9-1-1987

Basic Studies of III-IV High Efficiency Cell Components

Mark S. Lundstrom
Purdue University

M. R. Melloch
Purdue University

R. F. Pierret
Purdue University

Paul D. DeMoulin
Purdue University

D. P. Rancour
Purdue University

See next page for additional authors

Lundstrom, Mark S.; Melloch, M. R.; Pierret, R. F.; DeMoulin, Paul D.; Rancour, D. P.; and Kyono, C. S., "Basic Studies of III-IV High Efficiency Cell Components" (1987). *Department of Electrical and Computer Engineering Technical Reports.* Paper 574.
https://docs.lib.purdue.edu/ecetr/574

Authors

Mark S. Lundstrom, M. R. Melloch, R. F. Pierret, Paul D. DeMoulin, D. P. Rancour, and C. S. Kyono
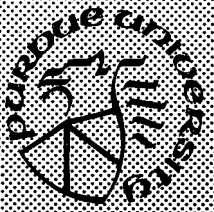
Basic Studies of III-IV High Efficiency Cell Components

M. S. Lundstrom, M. R. Melloch,
R. F. Pierret, P. D. DeMoulin,
D. P. Rancour, C. S. Kyono,
M. S. Carpenter and
M. E. Klausmeier-Brown

School of Electrical Engineering
Purdue University
West Lafayette, Indiana 47907

BASIC STUDIES

of

III-V HIGH EFFICIENCY CELL COMPONENTS

M.S. Lundstrom

M.R. Melloch

R.F. Pierret

P.D. DeMoulin

D.P. Rancour

C.S. Kyono

M.S. Carpenter

M.E. Klausmeier-Brown

School of Electrical Engineering

Technical Report TR-EE 87-33

Purdue University

West Lafayette, Indiana 47907

NOTICE

PREFACE

The efficiencies of III-V solar cells, especially GaAs-based cells, continue to rise. Because the material quality of such solar cells is now so high, it is time to examine the device design closely in order to ascertain what limits the performance of present, record-efficiency cells. Such work will provide accurate estimates of the realistic efficiency limits of III-V solar cells and will provide a roadmap for reaching ultimate efficiencies.

This project's objective is to improve our understanding of the generation, recombination, and transport of carriers within III-V homo- and heterostructures. The project consists of the fabrication and photovoltaic characterization of the basic building blocks of III-V cells: the pn junction, the pn heterojunction, the isotype (p-p and n-n) heterojunction) and graded gap semiconductors. A significant effort is also being directed at analyzing and understanding the performance of high-quality, III-V solar cells fabricated in industrial research laboratories throughout the United States. The project's goal is to use our understanding of the device physics of high-efficiency cell components to maximize cell efficiency. A related goal is the demonstration of new cell structures fabricated by molecular beam epitaxy (MBE). The development of measurement techniques and characterization methodologies is also a project objective. The insight into III-V device physics expected to occur during the course of this work will, we believe, identify paths towards higher efficiency III-V cells.

This report describes our progress during the second year of the project. Much of the first year was devoted to establishing MBE growth techniques, device fabrication capability, and at expanding our electrical characterization laboratory. This year's efforts were directed at the basic studies which comprise the core of the program. This report details accomplishments in the following areas: 1) baseline analysis of recombination losses in high-performance, GaAs, p-n heteroface cells, 2) characterization of electron injection currents in p^+ GaAs, 3) development of current DLTS for solar cell diagnostics, 4) measurement of recombination velocities at $p-p^+$ homo- and heterojunctions, and 5) observation of dark current suppression by $Al_xGa_{1-x}As$ buffer layers.

SUMMARY

Objectives

The objective of the project is to raise the understanding of dark current mechanisms in GaAs-related solar cells to a level comparable to that of silicon cells. Motivation for this work arises from the observation that much of the progress in crystalline silicon cell performance has occurred as a result of a very deep knowledge of the physics controlling the cell's dark current. Based on this knowledge, new cell structures evolved to suppress dominant dark current mechanisms. A comparable level of knowledge of GaAs cell device physics does not yet exist, but will be essential if cell performance near the thermodynamic limit is to be achieved.

Discussion

A broad investigation of minority carrier transport and recombination in GaAs has been initiated. The work includes investigating high-performance cells, in order to characterize performance-limiting factors, and experiments on MBE-grown test structures designed to obtain specific information on various aspects of minority carriers in GaAs. Several of the major thrusts of the projects are briefly described in this section.

Recombination Mechanisms in p/n Heteroface Cells

Because a comprehensive data base characterizing the device physics of high-efficiency, p/n heteroface solar cells did not exist, we undertook to create one using solar cells supplied to us by industrial research laboratories. The conclusions of this on-going study, which is discussed in Chapter 1, are, in brief, as follows. As expected, the very highest efficiency cells show exceeding low densities of mid-gap traps. Only one recombination center, whose density is below $10^{14} cm^{-3}$ and which appears to be EL2, is observed in very high quality cells. The very low space-charge recombination $(n=2)$ current has two consequences: 1) the diffusion current $(n=1)$ is a substantial portion of the 1-sun dark current and dominates under concentration, and 2) the low bulk $n=2$ current means that edge recombination is important and contributes significantly to the $n=2$ current at 1-sun in small $(0.25 cm^2)$ cells. The diffusion current appears to be dominated by hole injection into the bulk, which suggests that cell efficiency can be improved if hole injection can be suppressed.

Electron Injection in p-GaAs

The minority carrier electron density in the p-type region of a forward biased diode is proportional to $n_{ie}^2 D_n$, where n_{ie} is the effective intrinsic carrier density and D_n is the *minority* carrier diffusion coefficient. In heavily doped silicon, this product is about 100 times the value estimated by using n_i for lightly doped silicon along with majority carrier mobility values. Information on the value of this paramter in GaAs is not available, but its value is required for all device models. Chapter 2 describes the results of experments undertaken by our group to estimate the value of this parameter in p-GaAs.

In contrast to the observed behavior of p-type silicon, we find that the $n_{ie}^2 D_n$ product *decreases* with doping density in the middle 10^{17} to low $10^{18} cm^{-3}$ range. Bandgap narrowing effects which dominate the design of silicon cells appear to have little effect for typically employed emitter dopings of p/n heteroface cells. Data on the $n_{ie}^2 D_n$ product of very heavily doped p-GaAs, such as that employed for back-surface fields, is not yet available. Further work is needed to map out the value of this parameter as a

function of doping, to understand the result theoretically, and to explore the implications for cell design.

Properties of Minority Carrier Mirrors for GaAs-Based Solar Cells
A systematic experimental study of minority carrier mirrors for GaAs-based solar cells has been undertaken. The experiments completed so far utilize n^+/p GaAs diodes fabricated with films grown by molecular beam epitaxy (MBE). Cells were fabricated with (i) the p-type base grown directly on the p^+ substrate, (ii) the p-type base grown on a p^+ buffer layer, and (iii) the p-type base grown on a p^+ AlGaAs buffer layer. The dark current-voltage characteristics were then analyzed to compare the ability of various minority carrier mirrors to suppress dark current. The results showed that $p-p^+$ low-high homojunctions are ineffective as minority carrier mirrors; they displayed an interface recombination velocity of $\sim 6 \times 10^5$ cm/sec. The heterojunction back-surface field was only slightly more effective - an observation we attribute to the poor quality of the interface. Using demonstrated techniques for producing high-quality interfaces (e.g. with superlattice buffer layers) would, we believe, further lower the interface recombination velocity. One unexpected result was observed - the presence of an AlGaAs buffer layer seemed to result in diodes with a lower space-charge region recombination current. Since DLTS showed reduced levels of deep traps in these films, the AlGaAs layer may have a beneficial gettering effect. Heterojunction back-surface fields may provide benefits for high-efficiency cells quite distinct from their minority carrier reflecting properties.

Applications of Current DLTS to Solar Cell Diagnostics
Deep levels in semiconductors are commonly characterized by capacitance transient measurements (e.g. DLTS), but the large areas of solar cells complicate such measurements by overloading typical capacitance meters. In principle, however, current transients serve equally well and can even provide greater sensitivity in some cases. For these reasons, we have investigated the use of current transient measurments for the diagnostic evaluation of solar cells. The basic DLTS measurement and analysis technique has been modified; measurements are made at a constant temperature, and the spectra are plotted versus effective emission rate (as opposed to the usual plot versus temperature). For this reason, we call the technique emission-DLTS, or eDLTS.

Current sensing and amplifying circuitry has been designed and built, and data processing software was developed and implemented. The technique was applied to 0.25cm^2 GaAs solar cells. Advantages of the new technique include the ease of application to large area p-n junctions typical of solar cells, and the elimination of errors due to temperature hysteresis and unaccounted-for temperature dependencies. The theory and implementation of this technique are described in Chapter 3 of this report.

Conclusions

The basic studies our group is now engaged in are directed at providing information for attaining cell efficiencies near the thermodynamic limit. The work is motivated by three questions: 1) what are the values of the key physical parameters which control cell performance? 2) what are the dominant recombination loss mechanisms in present-day, high-performance cells and 3) how should cells be designed to minimize recombination losses? These basic studies, complemented by the sophisticated numerical device simulation capability at Purdue, should provide a roadmap for maximizing cell performance. The work is specifically directed at GaAs-based solar cells, but the methodology being developed for diagnosing cell performance and for the design of new cells should be broadly applicable.

The significant accomplishments of the past year's work are: 1) the first investigation of bandgap narrowing effects in p-GaAs, 2) measurment of the interface recombination velocity of $p-p^+$ back-surface fields in GaAs cells, and observation of dark current suppression by heterojunction back-surface fields. 3) analysis and autopsy of recombination mechanisms in high-efficiency MOCVD-grown p/n heteroface cells, and 4) development of a "current-DLTS" technique for solar cell diagnostics. The bandgap narrowing experiments show a decreasing $n_{ie}^2 D_n$ product in the $10^{17} - 10^{18}$ cm^{-3} doping range, which constrasts with the observed behavior in silicon. It is important to extend these measurements to the heavier doping typically used for back-surface fields and to characterize bandgap narrowing in n-GaAs. Our minority carrier mirror experiments showed that p-type homojunction back-surface fields are ineffective at comfining minority carriers, which suggests that heterojunction back-surface fields will have to be employed. Work directed at understanding this effect and at extending the measurement to n-GaAs will continue. Our work on characterizing recombination mechanisms in p/n heteroface cells is providing a wealth of information on cell device physics. The next task is to study device performance as cell design is varied. The current DLTS technique shows promise for diagnosing actual large area solar cells rather than small test diodes. DLTS has not yet provided us with a good diagnostic tool because the results of small test diodes rarely correlate with the performance of adjacent, large area cells. Work to apply this technique to 2 cm by 2 cm solar cells will be undertaken.

TABLE OF CONTENTS

CHAPTER 1

RECOMBINATION MECHANISMS IN
P/N HETEROFACE CELLS

Preface

This chapter is a status report describing an on-going study directed at characterizing recombination mechanisms in high-quality, p/n heteroface solar cells. The objective is to create a data base which characterizes the performance of present-day cells and to identify the efficiency-limiting mechanisms of current cells. The highest efficiency cells studied displayed extremely low n=2 (space-charge recombination) and n=1 (minority carrier diffusion) currents. Because the bulk, space-charge recombination currents in these cells is so low, the n=2 current is significantly affected by perimeter recombination, even in relatively large area $(A = 0.25 \text{cm}^2)$ cells. Although DLTS measurements have identified a few different defects in these cells, no strong correlation to the measured dark current was observed. DLTS measurements on the highest efficiency cells show only one deep level, which appears to be EL2. For very high efficiency cells, the minority carrier diffusion current comprises a substantial fraction of the dark current at one sun and dominates under concentration. In these cells the n=1 current can be explained by hole injection into the n-type bulk. For typically doped p^+ emitters, the emitter current component appears to be negligible. So-called bandgap narrowing effects, which are so important in p^+ silicon, were found to have little effect on conventionally designed p/n heteroface cells. The measurements described in this chapter also suggest that the front surface recombination velocity can sometimes exceed 10^5 cm/sec. Control of this parameter is essential for achieving maximum efficiency.

1.1. INTRODUCTION

Although the reported efficiencies of GaAs solar cells continue to advance [1,2], our understanding of the device physics of these cells is primitive when compared to the understanding of crystalline silicon cells. An improved understanding of the injection and recombination of minority carriers in GaAs is a prerequisite for achieving GaAs-based cell efficiencies near the thermodynamic limit. Detailed studies which relate the measured dark current to the cell's material and structural parameters are lacking. Little work has been reported on the role of so-called bandgap narrowing effects or the value of minority carrier diffusion coefficients—both important factors in silicon devices. In this chapter we report, analyze, and interpret the measured dark I-V and solar-cell characteristics of a series of MOCVD, GaAs, p/n heteroface solar cells. The objective of the study is to identify loss mechanisms in high-efficiency GaAs cells so that new cells, specifically designed to suppress these mechanisms, can be developed. The results obtained thus far suggest that with proper cell design additional reductions in dark current can be achieved.

For this study, dark currents were characterized by:

$$J = (J_{0F} + J_{0E} + J_{0B})(e^{qV/kT} - 1) + (J_{02B} + J_{02S})(e^{qV/2kT} - 1) , \qquad (1)$$

where the n=1 component of the saturation current density, $J_{0F} + J_{0E} + J_{0B}$, is the sum of the the front-surface, bulk-emitter and base component of currents respectively. The n=2 current component consists of the bulk space-charge current, J_{02B},

and the surface current at the space-charge perimeter, J_{02S}. To understand the cell's device physics, each of the various current components must be related to the material parameters and physical structure of the cell. While it is easy to extract a J_{01} and J_{02} by curve fitting a measured J-V characteristic, it is rather difficult to deduce the various physical components of these two saturation current densities. Much of the work to be described in this chapter is directed at just this objective — to quantify the recombination currents associated with the various regions of the cell. This insight into the sources of recombination is essential for designing higher performance cells.

Simple expressions for carrier injection into the emitter can be used because the electron diffusion length is expected to be much greater than the quasi-neutral emitter thickness. For the cells under consideration, we require $\tau_n \gg 0.03$ nanoseconds; τ_n is expected to be roughly 100 times this value in the high-efficiency cells used for this study. Under these conditions, the minority carrier electron distribution within the p-type emitter is approximately linear and the emitter component of J_{01} can be estimated from

$$J_{OF} + J_{OE} = \frac{qn_{iE}^2}{N_A} \times \frac{S_F + \dfrac{D_n W_E}{L_n^2}}{1 + \dfrac{S_F}{D_n/W_E}}, \tag{2}$$

where S_F is the front surface recombination velocity.

When the emitter surface is passivated by an $Al_{0.9}Ga_{0.1}As$ heteroface, S_F should be low and (2) reduces to

$$J_{OE} = \frac{qn_{iE}^2 W_E}{N_A \tau_n}. \tag{3}$$

If the heteroface layer were removed, S_F would be high and (2) would approach

$$J_{OF} = \frac{qn_{iE}^2 D_n}{N_A W_E}. \tag{4}$$

Equation (4), which shows that the emitter current varies as the inverse of the emitter thickness when the emitter surface is unpassivated, is the basis of an etch experiment to be described in the following section.

The current due to hole injection into the n-type base can be evaluated from

$$J_{OB} = \frac{qn_{iB}^2}{N_D} \frac{D_p}{L_p'}, \tag{5}$$

where L_p', an effective diffusion length for holes, depends on the actual diffusion length, the thickness of the base, and on the back-surface recombination velocity.

In addition to dark I-V measurements, we also characterized the performance of cells under illumination. By measuring a cell's short-circuit current and its reflectance as a function of optical wavelength, the internal quantum efficiency was deduced. A one-dimensional numerical simulation program, PUPHS1D [3], was then used to compare and extract minority carrier lifetimes and a front-surface recombination velocity from the internal quantum-efficiency data. This technique, coupled with the dark IV analysis and DLTS measurements, are the tools used for exploring the sources of

recombination.

The chapter is organized as follows. Section II discusses the experimental results: the description of cell structure and the fabrication process, the dark I-V extraction of J_{01} and J_{02}, quantum efficiency data, and etch experiments. Sections III and IV discuss the $n=2$ and $n=1$ components of dark current, respectively. The implications of these preliminary results for high-efficiency cell design are explored in Sec. V. And finally, Sec. VI summarizes the status of state-of-the-art GaAs solar-cell design.

1.2. EXPERIMENTAL RESULTS

The cell structure for the conventional GaAs solar cell is the p/n heteroface design, shown in Fig. 1. Starting with a heavily doped n-type substrate, a heavily doped n-type buffer layer is grown (for this study by MOCVD) that serves as a back-surface field. Atop this layer is a relatively low-doped n-type base region whose material quality is critical since a low minority carrier lifetime can severly limit the cells open-circuit voltage as well as restrict collection of light-induced carriers. On the base is a heavily doped p-type emitter. Its heavy doping helps minimize resistive drops due to the lateral current flow to the front metal grid and also suppresses minority carrier injection into the emitter. A wide bandgap material, $Al_{.9}Ga_{.1}As$, is grown on top of the GaAs emitter. The small lattice mismatch at the $Al_{.9}Ga_{.1}As$/GaAs interface produces effective surface-recombination velocities that are several orders of magnitude less than the recombination velocity, $10^7 \, cm/sec$, commonly seen at GaAs surfaces [4]. Optical absorption in $Al_{.9}Ga_{.1}As$ is low due to its large and indirect minimum bandgap and because the width of the heteroface is only several hundred angstroms. Ohmic contacts are subsequently formed on a GaAs cap-layer to avoid making contact to a wide bandgap semiconductor. Finally, an antireflection coating is laid on the top surface to reduce optical reflection losses. For the cells investigated, the p-type dopant was Zn.

Dark-current characteristics, solar-cell parameters, and cell-structure parameters (e.g. doping densities and layer thicknesses) were measured for four sets of cells. The first set, batch 052, had cell dimensions and doping densities as shown in Table 1.
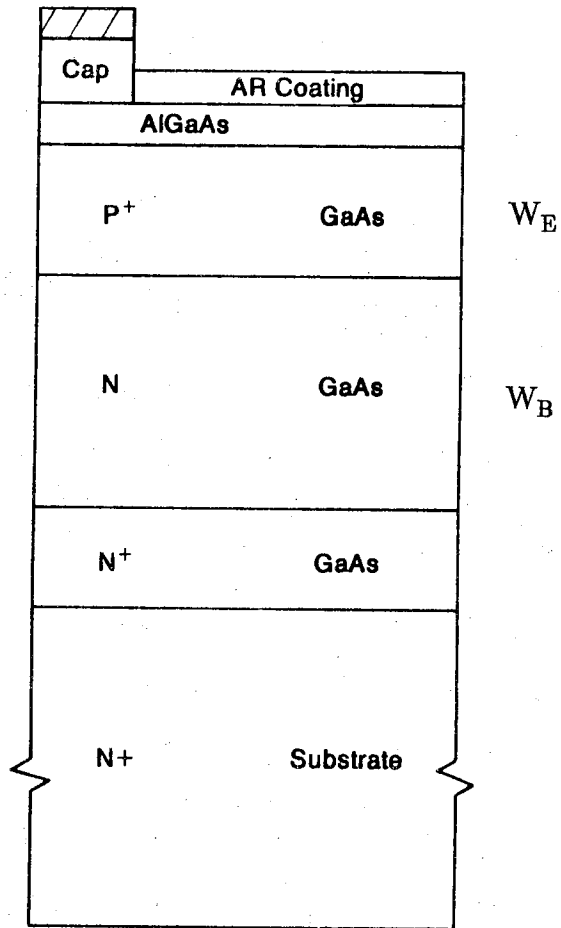
Fig. 1   Structure of the conventional P/N heteroface cell.

Parameter	Wafer 052	Wafer 733A(B)	Wafer 738	Wafer 746
$W_E(\mu m)$	0.5	0.5	0.25	0.5
$W_B(\mu m)$	2.0	2.0	2.0	2.0
P^+ emitter (cm^{-3})	6.0×10^{17}	2.0×10^{18}	2.0×10^{18}	2.0×10^{18}
N base (cm^{-3})	1.8×10^{17}	2.0×10^{17}	2.0×10^{17}	2.0×10^{17}
N^+ base(cm^{-3})	2.0×10^{18}	2.0×10^{18}	2.0×10^{18}	2.0×10^{18}
J_{02} (A/cm^2)	0.6×10^{-10}	$0.2(0.4) \times 10^{-10}$	0.2×10^{-10}	0.2×10^{-10}
τ_{SCR} (nsec)	4	8(4)	11	11
J_{01} (A/cm^2)	0.7×10^{-18}	$0.2(0.2) \times 10^{-18}$	0.1×10^{-18}	0.4×10^{-18}
V_{oc} (volts)	0.972	1.014(1.001)	1.025	
FF (%)	83.1	84.5(82.9)	82.7	
J_{SC} (mA/cm^2)	22.1	22.9(22.1)	26.7	
η (% AM1.5)	17.9	19.6(18.3)	22.6	

Table 1 Cell-structure, dark I-V (28 °C), and solar-cell
(25 °C) parameters for cells 052, 733, 738, 746.

For wafer 733, some cells (A) had AR coats applied by thermal evaporation while others (B) were applied by electron-beam evaporation. The numbers enclosed in parentheses are for cells 733B.

The p-type emitter doping density was deduced by measuring the resistance of a test resistor adjacent to each cell and was confirmed by C-V profiling using an aluminum Schottky barrier deposited directly on the p-type emitter. With the emitter doping known, the base doping was determined by the zero-bias capacitance of the p-n junction. The targeted thickness of the p-type emitter was confirmed during an etch experiment described below. The antireflection coating was Ta_2O_5 for cells on wafer 052. Au/Zn ohmic contacts covered approximately 6% of the surface. The cell area was 0.25 cm^2. The three other sets of cells, 733A, 733B, and 738, were found to possess a higher emitter doping level. Cells 733A and 733B were initially on the same wafer. After cleaving the wafer, a double-layer antireflection coating, ZnS/MgF$_2$, was deposited by thermal evaporation on cells 733A. On cells 733B, the antireflection coating, Ta_2O_5/MgF_2, was deposited by E-beam evaporation to explore possible differences in the two deposition technologies. The remaining set of cells with heavily doped emitters, those from batch 738, had a thinner emitter and a double-layer

antireflection coating, ZnS/MgF$_2$, deposited by thermal evaporation. Only dark I-V measurements were performed on a fifth set of cells, 746. Solar-cell parameters were not measured for these cells because their GaAs cap layers had not been removed.

The forward-biased dark-current characteristics were measured using four-point probe techniques and a Hewlett-Packard 4145A parameter analyzer with a temperature-controlled stage. A typical result, shown in Fig. 2, displays an n=2 characteristic at low biases and a fall-off at high biases due to the diode's series resistance. By curve-fitting in the region where 1<n<2, which occurs before series resistance becomes important, the saturation current density for the n=1 component of the current was extracted. The n=1 saturation current density, J_{01}, was verified by comparing it with that deduced from the cell's measured open-circuit voltage, which does not suffer from the series resistance limitation. The average saturation current densities along with the measured solar-cell parameters are shown in Table 1. The complete set of data is given in Appendix A. An inspection of Table 1 reveals that some cells had substantially lower n=2 currents than did others. Table 1 also reveals that cells on wafer 052 showed much higher n=1 currents than did the others. The lighter emitter doping of these devices cannot account for this difference. As we discuss in Sec. IV, the cell's performance indicates that its front surface recombination velocity exceeds 10^5 cm/sec.

For silicon bipolar devices, so-called bandgap narrowing effects are an important consideration, but no study of these effects on the electrical performance of GaAs diodes has been reported. To deduce the parameter, $n_{iE}^2 D_n$, which often controls injected diffusion currents, we performed etch experiments on cells 052-22 (light emitter doping) and 746-6 (standard emitter doping). Briefly, these experiments consisted of extracting J_{01} after successive etches which thinned the emitter. With the heteroface removed, the diffusion current is dominated by the emitter component and for a thin emitter, (2) reduces to

$$J_{01} \simeq J_{0F} = \frac{q n_{iE}^2 D_n}{N_A W_E(t)} \times \frac{S_F}{D_n/W_E(t) + S_F} . \tag{6}$$

According to (6), a plot of the measured $1/J_{01}$ versus emitter thickness (or etch time, assuming a constant etch rate) should be linear. Fig. 3 shows that the observed current varied as expected. From the slope of $1/J_{01}$ versus etch time the product, $n_{iE}^2 D_n$, was deduced. The conclusion, discussed more fully in Chapter 2 of this report, is that $n_{iE}^2 D_n$ decreases with doping density in the range of concentrations typically employed for emitters of p/n heteroface cells.

The emitter etch experiments also provided information about the n=2 component of the saturation current. Besides J_{02B}, the bulk space-charge component, there is also an n=2 current component associated with recombination in space-charge regions at the cell's perimeter. The saturation current density for this mechanism is proportional to the junction perimeter-over-area ratio, P/A, and is written as

$$J_{02S} = S_{SCR} L_s q n_i \frac{P}{A}, \tag{7}$$

where S_{SCR} is the surface-recombination velocity in the space-charge region at the perimeter of the junction, and L_s is a surface diffusion length. For large area cells, P/A is relatively small and the perimeter current is negligible. While 0.25 cm^2 diodes are usually considered large, bulk dark currents in high-quality solar cells are so low that
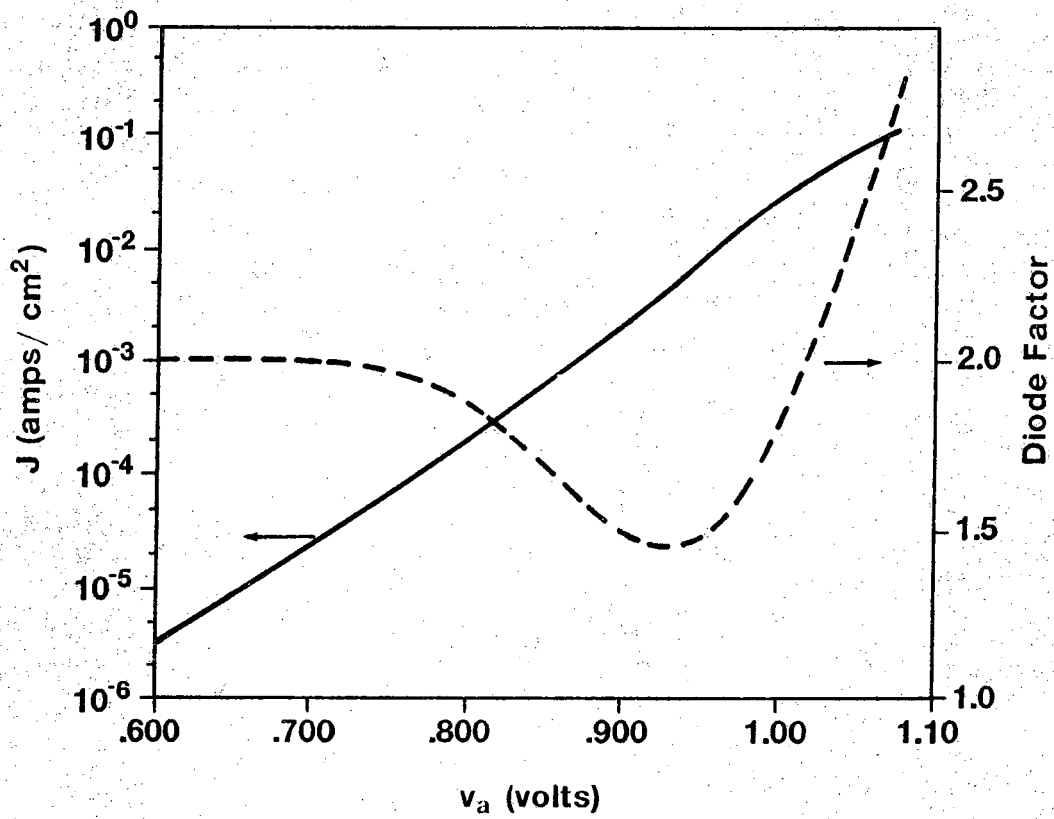
Fig. 2   Dark current versus voltage characteristic
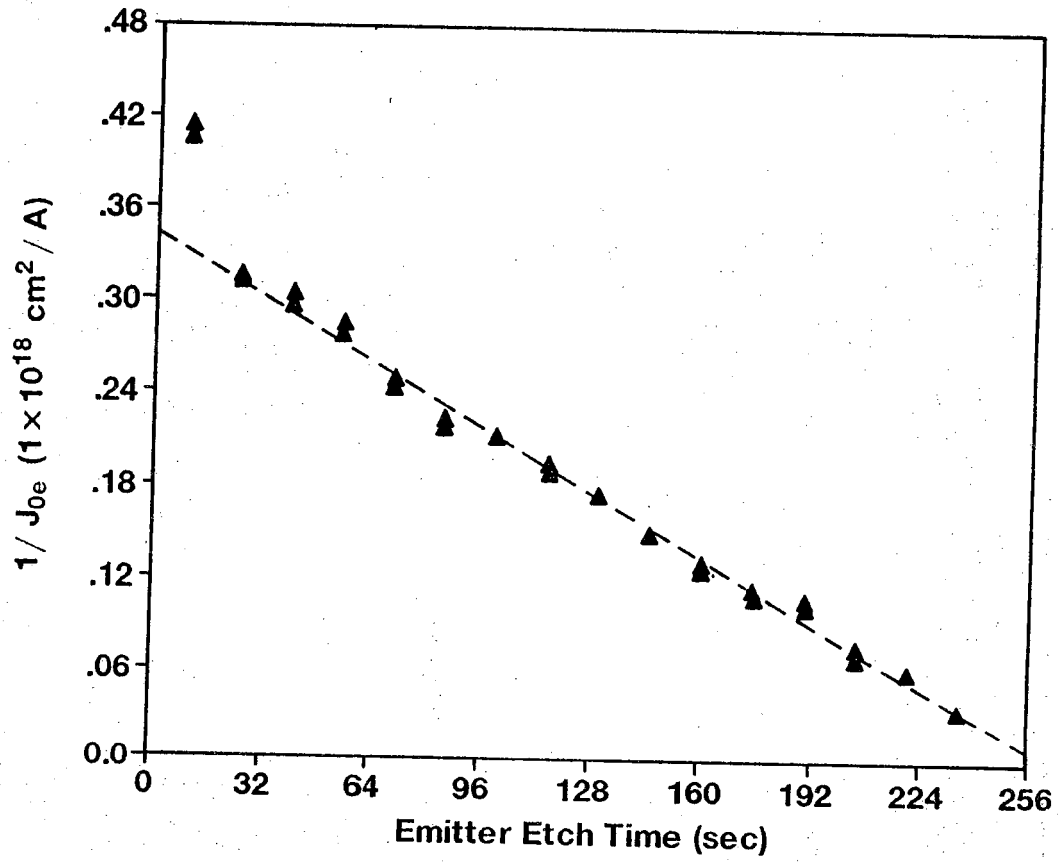for cell 052-22 at 28 ° C.

Fig. 3 $1/J_{0E}$ versus emitter etch time.

perimeter currents cannot automatically be assumed to be negligible. To estimate the magnitude of the perimeter current, the emitters of several cells were completely removed by wet etching between the metal contacts which increased the perimeter to area ratio from 8 to 567 cm^{-1}. Two cells with lightly doped emitters, 052-22 (the same cell used for the etch experiment above) and 052-23, were etched first. The same experiment was conducted for five cells with more heavily doped emitters, 733A-20, 738-9, 738-26, 746-6, and 746-7. For each cell, the n=2 component of the saturation current was extracted before and after etching. Table 2 shows pre-etch and post-etch data for J_{02}.

Cell ID	J_{02} (A/cm^2) (pre-etch)	J_{02} (A/cm^2) (post-etch)	$S_{SCR}L_s$ (cm^2/sec)
052-22	0.21×10^{-10}	$14. \times 10^{-10}$	6.0
052-23	0.27×10^{-10}	8.1×10^{-10}	3.4
733A-20	0.20×10^{-10}	$34. \times 10^{-10}$	14
738-9	0.46×10^{-10}	$98. \times 10^{-10}$	41
738-26	0.20×10^{-10}	$20. \times 10^{-10}$	8.3
746-6	0.051×10^{-10}	$32. \times 10^{-10}$	13
746-7	0.075×10^{-10}	$19. \times 10^{-10}$	7.9

Table 2 Results of perimeter-current etch experiment (28 ° C).

After the etch, J_{02} is dominated by recombination at the perimeter space-charge region. By equating the measured, post-etch, J_{02} to the right hand side of (7), a value for $S_{SCR}L_s$ can be deduced. The results, displayed in Table 2, are in general agreement with those reported by other workers [5,6]. Although $S_{SCR}L_s$ may have been influenced by the etch, the results displayed in Table 2 can be used to estimate the perimeter current in the original, 0.25 cm^2 cells. The implications of such estimates are discussed in Sec. 1.3.

The quantum efficiency data for the highest efficiency cell, 738-33, is shown in Fig. 4. The internal quantum efficiency was deduced from the measured external quantum efficiency and the cell's reflectance. The accuracy of the quantum efficiency data was confirmed by integrating the external quantum efficiency over the solar spectrum and by checking that it matched the measured short-circuit current.
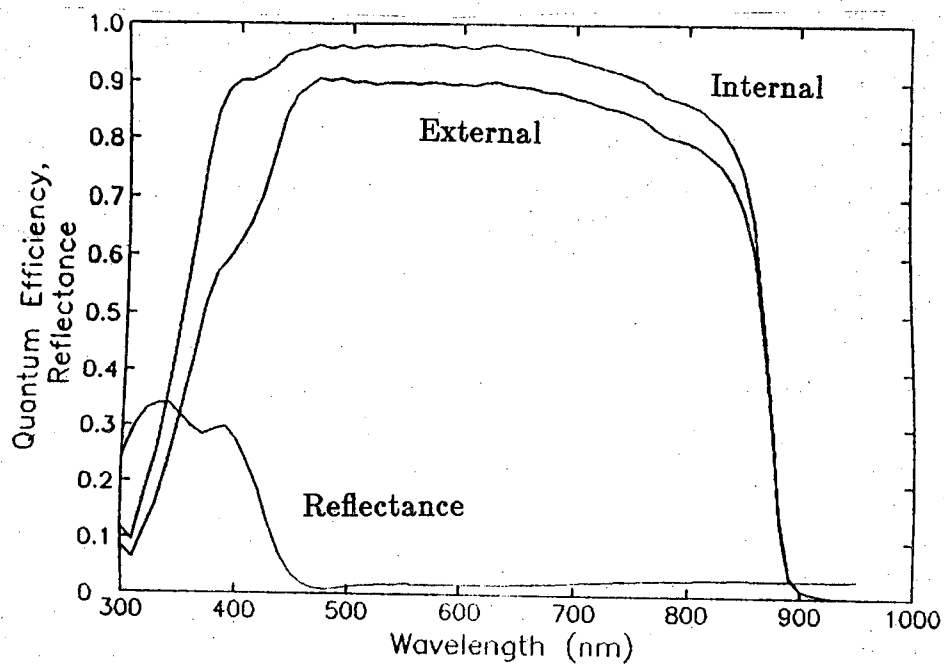
Fig. 4   Quantum efficiency data for cell 738-3-33.

1.3. ANALYSIS OF n=2 CURRENT COMPONENT

Our objective in performing the measurements described above was to relate the measured dark current to the cell's material parameters, dimensions and doping densities. The n=2 component, which comprises a substantial fraction of the one-sun dark current is considered first. The n=2 saturation current density associated with recombination in the bulk space-charge region can be written as

$$J_{02B} = \frac{q n_i W_{eff}}{\tau_{SCR}} , \qquad (8a)$$

where

$$\tau_{SCR} = \sqrt{\tau_n \tau_p} , \qquad (8b)$$

and W_{eff} is an effective width given by

$$W_{eff} = W_{SCR} \frac{\pi}{4} \frac{k_B T / q}{\left[(V_{bi} - V_A)(V_{bi} - \frac{V_A}{2} - \frac{k_B T}{q} \ln(\frac{N_A}{n_i})) \right]^{1/2}} , \qquad (8c)$$

where V_A is the applied bias, W_{SCR} is the width of the space-charge region at bias V_A, V_{bi} is the built-in voltage, and N_A is the emitter doping level. Equations (8a-8c) assume that dominant recombination centers are near midgap and that their electron and hole capture coefficients are roughly equal. The lifetime, τ_{SCR}, can be deduced by comparing (8a) with J_{02B} extracted from the measured data. The resulting lifetimes, also displayed in Table 1, are reasonable for device-quality GaAs.

DLTS measurements were performed on all cells except those from batch 746. On small diodes which were mesa-etched from the resistor pattern adjacent to each cell, only a single DLTS peak was observed. The trap level, $E_C - E_T \simeq 0.81$ eV, and electron capture cross-section, $\sigma \simeq 7 \times 10^{-14}$ cm^2, suggest that the peak is due to EL2. Note that cells 733A, 738, and 746 displayed an n=2 dark current substantially lower than did cells 052 and 733B. Cells 052 and 733B had anti-reflection coatings deposited by electron beam evaporation while the others were applied by thermal evaporation. When DLTS measurements were performed on the solar cells themselves, cells 733B showed an additional, very deep peak not observed in cells 733A and 738. These observations are consistent with the hypothesis that electron-beam evaporation introduces damage into the cells. One of the very earliest cells (not included in Table 1) showed an additional peak which we tentatively attribute to iron (refer to Chapter 3 for a discussion of these measurements). None of the later cells showed this peak. In summary, only one trap level, thought to be EL2, is observed in high-quality cells.

The results displayed in Table 2 suggest that the perimeter current may be an important component of the n=2 current — even for fairly large area cells. The perimeter current in 0.25 cm^2 cells was estimated using (7) with the $S_{SCR}L_s$ values displayed in Table 2 and $P/A = 8$ cm^{-1} (the assumption being that the etch did not alter the surface recombination velocity of the exposed perimeter). For the low-doped-emitter cells 052-22 and 052-23, we find that perimeter currents are significant to the overall n=2 current prior to etching. The perimeter current comprises roughly two-thirds and one-fourth of the observed n=2 current for the two cells respectively. Because the values for τ_{SCR} were calculated using the assumption that the n=2 component is entirely due to bulk space-charge recombination, the values for τ_{SCR} reported in Table 1 may underestimate the true lifetime. The cells with the more heavily doped emitters, 733A-20, 738-9, 738-26, 746-6, and 746-7 also had substantial perimeter

currents. The estimated pre-etch perimeter currents were found to be substantially greater than the measured n=2 component of current.

These results demonstrate that perimeter currents are not negligible in high-quality, $0.25 cm^2$ cells and suggest that they may even dominate cell performance. The fact that the estimated pre-etch perimeter current sometimes exceeded the measured pre-etch current, may indicate that the $H_2SO_4:H_2O_2:H_2O$ etch employed adversely affected the cell's exposed perimeter.

1.4. ANALYSIS Of n=1 CURRENT COMPONENT

While the n=2 component of the cell's current can be readily understood in terms of the relatively low trap concentrations in these high-quality MOCVD films, the cell's n=1 component may control its performance. Using the average parameters in Table 1, we find that near the open-circuit voltage at one AM1.5 sun, the n=1 current is about equal to the n=2 current. It is important to understand the origin of the diffusion current and its relation to the cell's materials and device parameters because it will certainly dominate the performance of concentrator cells. Values for GaAs materials parameters, such as the effective intrinsic carrier concentration and minority carrier electron mobility, have been documented but their accuracy is not well established. To acquire confidence in these parameters, results of etch experiments were analyzed to quantify the product $D_n n_{iE}^2$ in the emitter layer of the cells. For the case of a low recombination velocity at the $Al_{.9}Ga_{.1}As/GaAs$ interface and a transparent emitter, D_n is not a factor in the emitter component of the diffusion current, as demonstrated by (3). When front surface recombination is a significant component of the diffusion current, however, both n_{iE}^2 and D_n are important for predicting dark current. In either case, at least one of these parameters could create uncertainty in our prediction of $J_{0F} + J_{0E}$.

To quantify $D_n n_{iE}^2$, the first etch experiment was performed on cell 052-22, which had an emitter doping level of $6 \times 10^{17} cm^{-3}$ and on cell 746-6, whose emitter was doped to $2 \times 10^{18} cm^{-3}$. The $D_n n_{iE}^2$ product can be estimated from the slope of J_{01} versus emitter thickness as displayed in Fig. 3. As described in Chapter 2 of this report, the $n_{iE}^2 D_n$ product was deduced from the slope of the measured $1/J_{01}$ versus etch time. The results obtained were $D_n n_{iE}^2 = 8 \times 10^{14} cm^{-4} sec^{-1}$ for the cell with a lightly doped emitter and $D_n n_{iE}^2 = 7 \times 10^{14} cm^{-4} sec^{-1}$ for the cell with a more heavily doped emitter. The product can also be estimated by theoretical models for electron mobility and effective intrinsic carrier concentration. Using an intrinsic carrier density from Blakemore [7], corrected for bandgap shrinkage in p-GaAs according to Casey and Panish [8], and the theoretical minority carrier mobility of Walukiewicz et al. [9], we deduce $D_n n_{iE}^2 = 7 \times 10^{14} cm^{-4} sec^{-1}$ for both the heavily doped and lightly doped cells. The agreement with that predicted for uncompensated material is good for both cells. This suggests that there are not major uncertainties in the minority carrier transport parameters of p-type GaAs in this doping range.

An expected J_{01} can be computed from the cell's material and device parameters. Assuming that S_F is low, the cell's emitter current component should be given by (2) in which n_{iE} is the intrinsic carrier concentration for GaAs ($2.65 \times 10^6 cm^{-3}$ at $28° C$ [7]) corrected for 13.5×10^{-3} eV of bandgap shrinkage [8]. For the more lightly doped base, we assume negligible bandgap narrowing and compute the base component of J_{01} from (5) taking L_p to be the hole diffusion length. Using the measured doping densities, taking D_p from majority carrier values quoted by Sze [10], and estimating τ_n and τ_p by

τ_{SCR} given in Table 1 (these lifetimes are comparable to those routinely reported for high-quality GaAs cells), we find that $J_{01} = J_{0E} + J_{0B} = 0.07 \times 10^{-18} + 0.24 \times 10^{-18}$ A/cm^2 for cells with low emitter doping and $J_{01} = J_{0E} + J_{0B} = 0.02 \times 10^{-18} + 0.16 \times 10^{-18}$ A/cm^2 for cells with high emitter doping. The current predicted for the heavily doped cells is in good agreement with the measured values. The estimate for the low-doped-emitter cells, however, is about three times greater than the observed J_{01}. The explanation for this discrepancy is as follows.

We might account for the observed current due to an unexpected high J_{0B}. Equating (5) to the observed J_{01}, and assuming $D_p = 5.7$cm^2/v—sec [10], we find the $L_p \simeq 0.5$ micrometers. This effective length is much shorter than the expected minority carrier diffusion length (1–2μm). A more likely explanation for the discrepancy, however, is a higher than expected S_F at the Al$_{.9}$Ga$_{.1}$As/GaAs interface. Using (3), we can account for the observed dark current if $S_F \simeq 6 \times 10^5$ cm/sec. The recombination velocity is much greater than that reported for a high-quality interface [4,11,12]; however, the work of Partain et al. [13] showed that S_F can vary from less than 10^4 to 4×10^5 cm/sec in p/n heteroface cells. A relatively high interface-recombination velocity is therefore the likely cause of the excessive dark current in these low-doped cells.

The agreement between the estimated and observed J_{01} for the high-doped-emitter cells probably suggests that the front interface is sufficiently passivated. This speculation is confirmed by the quantum-efficiency data shown in Fig. 4. Using a one-dimensional numerical simulation program, PUPHS1D, and the experimental quantum-efficiency data, we find $S_F < 10^4$ cm/sec for cell 738-33. Therefore, it seems likely that the front interface-recombination velocity is low in the higher efficiency cells, 733 and 738. Interface quality is crucial to achieving very high efficiencies, and the performance of cells on wafer 052 indicate that values less than 10^4 cm/sec are not always obtained.

1.5. IMPLICATIONS FOR HIGH-EFFICIENCY CELL DESIGN

Gallium arsenide p/n heteroface cells have achieved high conversion efficiencies, but performance can still be improved by optimizing cell designs. Although the n=2 component of dark current is significant at 1-sun operation, GaAs cells are projected for concentrator applications. For this reason, our focus should be on the reduction of the n=1 diffusion current. If hole injection into the base is indeed the dominating diffusion component that limits cells with well passivated window layers, then there are two approaches for improving conversion efficiency: 1) reduce the dark current by suppressing this hole injection into the base (This could be accomplished with a more heavily doped base or with a heterojunction back-surface field.) and 2) increase the width of the emitter layer so that optical absorption occurs where collection efficiency is high. For doping levels commonly found in GaAs solar cells, emitter diffusion lengths of 4μm are conceivable. Such diffusion lengths would allow the emitter thickness to increase from that commonly found in present-day cells. Due to a lower sheet resistance, increasing the emitter thickness would also benefit the fill factor—an important advantage for concentrator cells. But such device designs can only work when the front interface-recombination velocity is $\simeq 10^4$ cm/sec or less. If this performance goal is achieved, along with bulk-emitter lifetimes near the radiative limit, GaAs solar cells should be able to approach their thermodynamic-limiting conversion efficiencies.

1.6. CONCLUSIONS

The dark I-V and solar-cell characteristics of high-quality p/n heteroface cells were measured and analyzed. At one-sun operation, the cells' diffusion current was found to be an important component of the dark current. We found evidence that heteroface recombination velocities are not always under control. Future work on understanding the mechanism which controls interface recombination is needed since a well passivated front surface is critical to the performance of these cells. The highest efficiency cells display very low $n=1$ and $n=2$ dark currents. Since hole injection is thought to control their dark-current characteristics, new device designs which reduce J_{0B} would improve cell performance. So it seems that progress in the already high efficiencies of p/n heteroface cells can still be achieved.

CHAPTER 1 REFERENCES

[1]   S. Tobin et al., presented at the 19th IEEE Photovoltaic Specialists Conference (1987).

[2]   H.C. Hamaker, C.W. Ford, J.G. Werthen, G.F. Virshup, V.R. Kaminar, D.L. King, and J.M. Gee, *Appl. Phys. Lett.,* Vol. 47, p. 762, 1985.

[3]   M.S. Lundstrom and R.J. Schuelke, *IEEE Trans. Electron Dev.,* Vol. ED-30, p. 1151, 1983.

[4]   H.C. Casey, B.I. Miller, and Pinkas, *J. Appl. Phys.* Vol. 44, p. 1281, 1973.

[5]   C.H. Henry, R.A. Logan, and F.R. Merritt, *J. Appl. Phys.,* Vol. 49, p. 3530, 1978.

[6]   T.J. de Lyon, H.C. Casey, Jr., M.L. Timmons, and J.A. Hutchby, D.H. Dietrich, *Appl. Phys. Lett., Vol. 50, p. 1903, 1987.*

[7]   J.S. Blakemore, *J. Appl. Phys.,* Vol. 53, p. R123, 1982.

[8]   H.C. Casey and M.B. Panish, *Heterostructure Lasers,* New York, Academic Press, 1978.

[9]   W. Walukiewicz, J. Lagowski, L. Jastrzebski, and H.C. Gatos, *J. Appl. Phys.,* Vol. 50, pp.5040-5042, 1979.

[10]   S.M. Sze, *Physics of Semiconductor Devices, 2nd Ed.,* John Wiley and Sons, New York, 1981.

[11]   R.J. Nelson, *J. Vac. Sci. Technol.* Vol. 15, p.1475, 1978.

[12]   P. Dawson and K. Woodbridge, *Appl. Phys. Lett.* Vol. 45, p.1227, 1984.

[13]   L.D. Partain, M.S. Kuryla, L.M. Fraas, P.S. McLeod, and J.A. Cape, to be published in *J. Appl. Phys.*

APPENDIX A

Cell ID	J_{02} (A/cm^2)	J_{01} (A/cm^2)	τ_{SCR} (nsec)	V_{oc} (volts)	FF (%)	J_{SC} (mA/cm^2)
2	0.9×10^{-10}	0.3×10^{-18}	2	0.968	83.9	21.7
15	0.5×10^{-10}	0.6×10^{-18}	4	0.974	83.4	22.1
19	0.5×10^{-10}	0.8×10^{-18}	4	0.971	82.5	22.3
20	1.0×10^{-10}	0.2×10^{-18}	2	0.976	83.3	22.4
21	0.4×10^{-10}	0.9×10^{-18}	5	0.977	83.5	22.3
22	0.3×10^{-10}	0.9×10^{-18}	6	0.975	83.2	22.3
23	0.4×10^{-10}	1.5×10^{-18}	5	0.965	82.2	21.7
average	0.6×10^{-10}	0.7×10^{-18}	4	0.972	83.1	22.1

Table 3 Results of dark I-V (28 ° C) and solar-cell (25 ° C) measurements for cells 052.

Cell ID	J_{02} (A/cm^2)	J_{01} (A/cm^2)	τ_{SCR} (nsec)	V_{oc} (volts)	FF (%)	J_{SC} (mA/cm^2)
20	0.2×10^{-10}	0.05×10^{-18}	6	1.013	84.5	22.6
26	0.06×10^{-10}	0.1×10^{-18}	19	1.015	85.4	22.7
27	0.2×10^{-10}	0.07×10^{-18}	4	1.010	83.5	22.9
32	0.1×10^{-10}	0.07×10^{-18}	8	1.017	85.1	23.1
33	0.2×10^{-10}	0.08×10^{-18}	6	1.013	84.2	23.2
average	0.2×10^{-10}	0.07×10^{-18}	9	1.014	84.5	22.9

Table 4 Results of dark I-V (24 °C) and solar-cell (25 °C) measurements for cells 733A.

Cell ID	J_{02} (A/cm^2)	J_{01} (A/cm^2)	τ_{SCR} (nsec)	V_{oc} (volts)	FF (%)	J_{SC} (mA/cm^2)
2	0.3×10^{-10}	0.05×10^{-18}	3	0.998	82.5	21.8
10	0.2×10^{-10}	0.2×10^{-18}	6	1.002	83.7	22.0
25	0.3×10^{-10}	0.1×10^{-18}	4	1.002	82.6	22.3
average	0.3×10^{-10}	0.1×10^{-18}	4	1.001	82.9	22.1

Table 5 Results of dark I-V (24 $^\circ$C) and solar-cell (25 $^\circ$C) measurements for cells 733B.

Cell ID	J_{02} (A/cm^2)	J_{01} (A/cm^2)	τ_{SCR} (nsec)	V_{oc} (volts)	FF (%)	J_{SC} (mA/cm^2)
2	0.2×10^{-10}	0.03×10^{-18}	5	1.023	83.6	26.7
9	0.2×10^{-10}	0.04×10^{-18}	5	1.021	82.2	25.8
11	0.08×10^{-10}	0.1×10^{-18}	14	1.024	84.5	25.9
12	0.1×10^{-10}	0.07×10^{-18}	8	1.024	84.4	26.8
18	0.06×10^{-10}	0.09×10^{-18}	18	1.025	84.7	26.7
19	0.07×10^{-10}	0.09×10^{-18}	16	1.026	82.7	27.2
25	0.1×10^{-10}	0.07×10^{-18}	11	1.026	84.4	26.6
26	0.07×10^{-10}	0.07×10^{-18}	15	1.026	70.3	27.1
27	0.2×10^{-10}	0.06×10^{-18}	6	1.026	84.4	26.8
32	0.09×10^{-10}	0.07×10^{-18}	12	1.025	83.9	26.9
33	0.08×10^{-10}	0.08×10^{-18}	13	1.027	84.7	27.2
average	0.1×10^{-10}	0.07×10^{-18}	11	1.025	82.7	26.7

Table 6 Results of dark I-V (24 $^\circ$ C) and solar-cell (25 $^\circ$ C) measurements for cells 738.

Cell ID	J_{02} (A/cm^2)	J_{01} (A/cm^2)	τ_{SCR} (nsec)
1	0.2×10^{-10}	0.1×10^{-18}	4
2	0.1×10^{-10}	0.2×10^{-18}	11
3	0.07×10^{-10}	0.2×10^{-18}	16
4	0.08×10^{-10}	0.2×10^{-18}	13
6	0.07×10^{-10}	0.2×10^{-18}	16
7	0.1×10^{-10}	0.2×10^{-18}	11
9	0.08×10^{-10}	0.2×10^{-18}	13
11	0.3×10^{-10}	0.1×10^{-18}	4
average	0.1×10^{-10}	0.2×10^{-18}	11

Table 7 Results of dark I-V (24 °C) measurements for cells 746.

CHAPTER 2

THE $n_{ie}^2 D_n$ PRODUCT FOR ELECTRON INJECTION

IN MOCVD-GROWN, ZN-DOPED, P-GAAS

I. INTRODUCTION

A quantitative understanding of electron injection and transport in quasi-neutral p-GaAs is essential for the design of high performance bipolar devices such as solar cells and transistors. Device designers must know how the effective intrinsic carrier concentration, n_{ie}, the minority carrier diffusion coefficient, D_n, and the minority carrier lifetime, τ_n, vary as a function of doping density. These three parameters are difficult to extract from steady-state measurements because device performance is controlled by products of parameters such as $n_{ie}^2 D_n$ and diffusion length, $\sqrt{D_n \tau_n}$ [1]. Nevertheless, knowledge of these two products (or an equivalent set of parameters) is all that is required for the steady-state analysis of bipolar devices [1]. During the past decade, much work has been devoted to mapping out these parameters as a function of doping density in silicon. The data of Slotboom and DeGraaff [2], for electrons in p-silicon, are plotted in Fig. 1; the observed increase in $n_{ie}^2 D_n$ with N_A is attributed to so-called bandgap narrowing effects which increase n_{ie}^2 at high doping densities. For p-GaAs, D_n can be estimated from the theoretical work of Walukiewicz et al [3] and n_{ie} from the measured bandgap shrinkages of Casey and Stern [4], but such estimates have not been tested experimentally in devices. In this chapter we analyze diode characteristics to deduce the $n_{ie}^2 D_n$ product for p-type GaAs grown by MOCVD and doped with zinc. In contrast to the observed behavior for electrons in p-silicon, we find a decrease of $n_{ie}^2 D_n$ with hole concentration in a range of concentrations from middle 10^{17} cm^{-3} to low 10^{18} cm^{-3}. Accurate modeling and analysis of GaAs bipolar devices requires further work to extend such measurements to higher doping densities, to other p-type dopants, and to measure the individual parameters, n_{ie} and D_n.

II. EXPERIMENTAL TECHNIQUE

Experiments were conducted on p/n heteroface solar cells fabricated on MOCVD-grown films. The device structure is displayed in Fig. 2 along with the targeted thicknesses of the various layers. Two different types of devices were studied: the first with a p-emitter doping of 6×10^{17} cm^{-3} and the second with an emitter doped at 2×10^{18}. The p-type dopant was zinc. For both cells, the n-base was moderately doped; 1.8×10^{17} cm^{-3} for the first cell and 2.0×10^{17} for the second. These doping densities were deduced by capacitance-voltage profiling using an aluminum Schottky barrier deposited directly on the p-type emitter and from the zero-bias capacitance of the p-n junction. The front surfaces of the cells were passivated by an $Al_{0.9}Ga_{0.1}As$ heteroface. The metal grid covered about 6% of the 0.25 cm^2 cell area.

The dark current versus voltage characteristic of a typical cell at 28° C is shown in Fig. 3. For biases below which the series resistance is important, the measured characteristic is well-described by

$$J = J_{01} \left(e^{qV/kT} - 1 \right) + J_{02} \left(e^{qV/2kT} - 1 \right) . \tag{1}$$

By curve fitting the measured characteristic in a bias range where resistive drops were unimportant, the two saturation current densities, J_{01} and J_{02} were extracted. For the
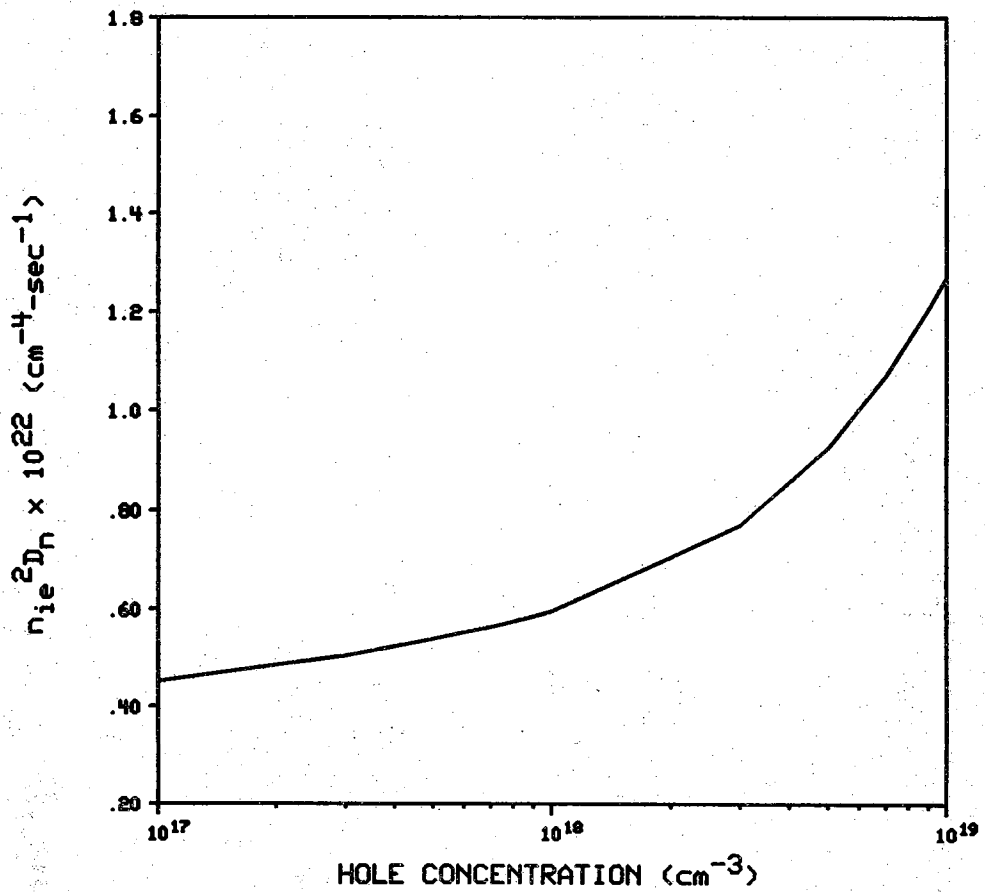
Figure 1   Measured $n_{ie}^2 D_n$ product for p-silicon. The curve uses the bandgap narrowing quoted by Slotboom and DeGraaff [2] and majority carrier electron mobilities in silicon.
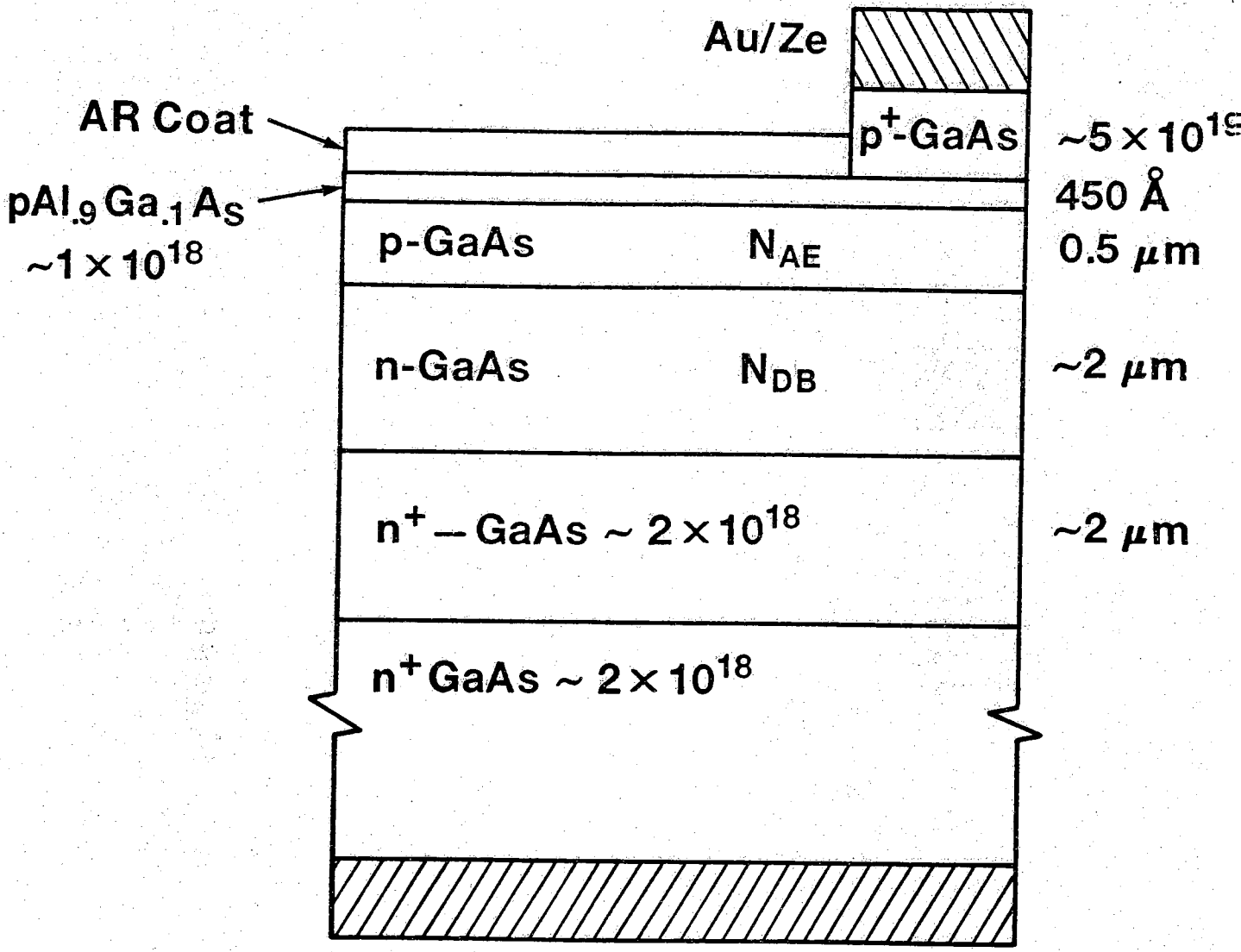
Figure 2   Device structure for the p/n heteroface solar cells used for the experiments. Targeted layer thicknesses are shown, the thickness of the p-type emitters were verified during the etch experiment described in the text.
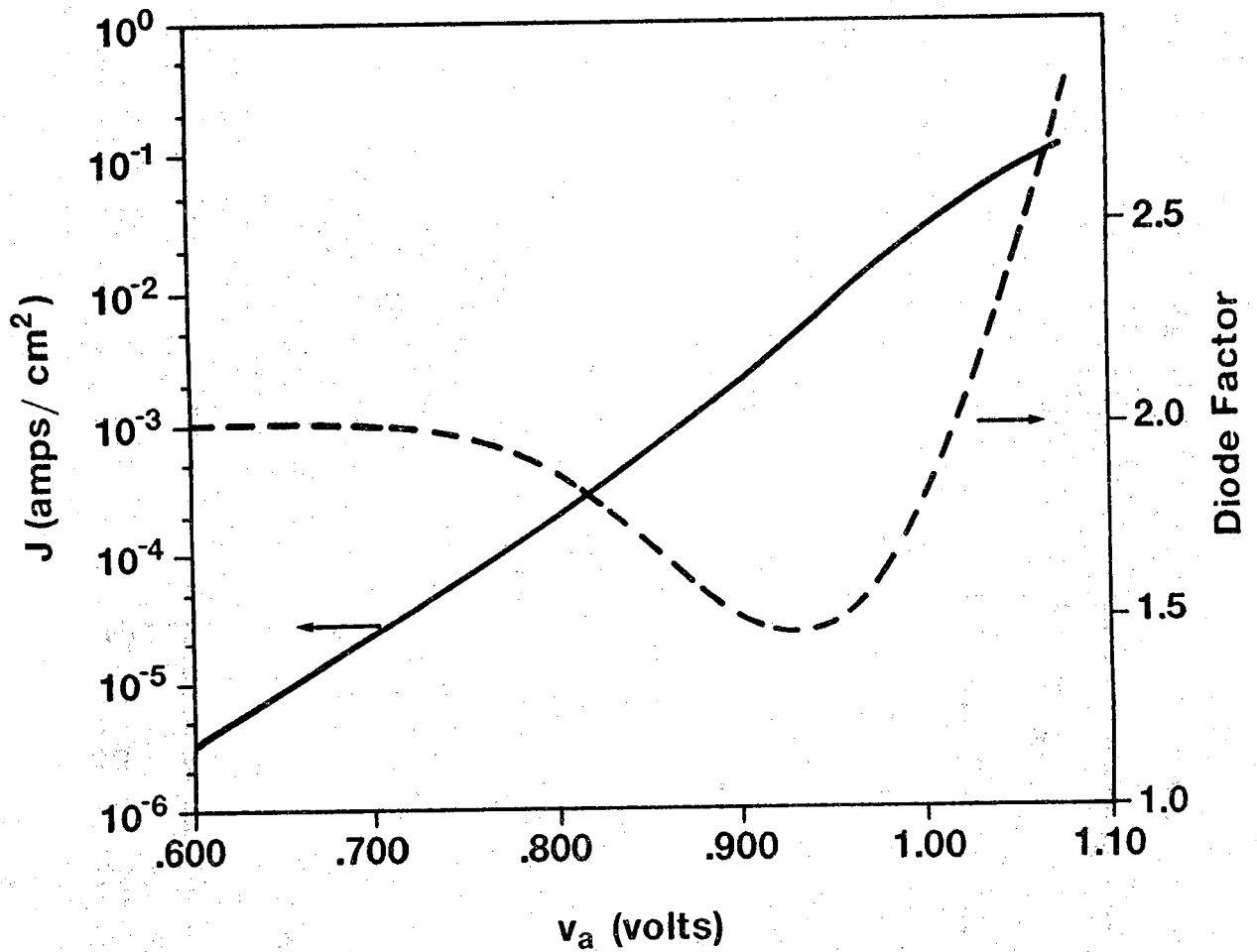
Figure 3   Typical current versus voltage characteristic for a cell with light emitter doping at 28 °C. The diode quality factor, n, is also displayed.

cells with the lightly doped emitters, values of J_{01} ranged from $0.4-1.3 \times 10^{-18}$ A/cm^2. Values ranged from $0.1-0.4 \times 10^{-18}$ A/cm^2 for the cells with the more heavily doped emitter.

The experiments consisted of two parts, the first required the removal of the $Al_{0.9}Ga_{0.1}As$ heteroface by etching in $H_2SO_4:H_2O_2:H_2O$ (2:1:96). The I–V characteristic was then re-measured and a new J_{01} was then extracted. As shown in Table 1, a large increase in J_{01} was observed when the heteroface was removed.

Parameter	Cell 1	Cell 2
Emitter doping, N_A	6.0×10^{17} cm^{-3}	2.0×10^{18} cm^{-3}
Base doping, N_D	1.8×10^{17} cm^{-3}	2.0×10^{17} cm^{-3}
J_{01} (with HF)	0.71×10^{-18} A/cm^2	0.16×10^{-18} A/cm^2
J_{01} (without HF)	3.4×10^{-18} A/cm^2	0.94×10^{-18} A/cm^2
$n_{ie}^2 D_n$ (A)	0.70×10^{15} cm^{-4}–sec^{-1}	0.55×10^{15} cm^{-4}–sec^{-1}
$n_{ie}^2 D_n$ (B)	0.78×10^{15} cm^{-4}–sec^{-1}	0.67×10^{15} cm^{-4}–sec^{-1}

Table 1   Results of emitter etch experiments. Data in the row labeled "with HF," refers to cells whose front surface is passivated by an $Al_{0.9}Ga_{0.1}As$ heteroface, and the row labeled "without HF" refers to results obtained after the heteroface was removed by etching. Estimate (A) is the $n_{ie}^2 D_n$ product obtained from the increase in J_{01} observed after removing the heteroface and (B) refers to the value obtained from the slope of $1/J_{01}$ versus emitter etch time. All measurements were performed on a temperature-controlled stage. Measurements for Cell 1 were taken at a temperature of 28 ° C while those for Cell 2 were taken at a temperature of 24 ° C. The Cell 2 values were corrected to provide the corresponding 28 ° C value using the known temperature dependence of n_{io}. The actual values measured for cell 2 were: J_{01} (with HF) = 0.075×10^{-18} and J_{01} (without HF) = 0.44×10^{-18} A/cm^2.

After removing the heteroface, the n=1 (diffusion) current is dominated by electron injection into the p-emitter and can be described by

$$J_{OE} = \frac{q n_{ie}^2 D_n}{N_A W_E} \times \frac{S_F}{D_n/W_E + S_F} . \tag{2}$$

For an unpassivated GaAs surface, the surface recombination velocity, S_F, is expected to be $\sim 10^7$ cm/sec [5]. Since the diffusion velocity, D_n/W_E, is on the order of 10^6 cm/sec, the factor involving S_F is expected to be about 0.9. Equation (2) assumes that the recombination of electrons in the bulk emitter is negligible, that is $L_n \gg W_E$. For these cells, this condition requires that τ_n greatly exceed 0.03 nanoseconds. The electron lifetime in these high-efficiency solar cells is thought to be

roughly 100 times this value, so (2) should accurately describe the emitter current of the cells without a heteroface. Using a typical value of hole diffusion length for high-efficiency cells of this type (2μm), we estimate the base component of the n=1 saturation current to be $\simeq 0.1 \times 10^{-18}$ A/cm^2, which is much smaller than the observed post-etch J_{01}. Consequently, we can equate (2) to the measured J_{01} and deduce the product, $n_{ie}^2 D_n$, if we set the factor involving the front surface recombination velocity to unity (that is, we assume that S_F is infinity). The results, displayed in Table. 1, are expected to be about 10% low because of the assumption of an infinite surface recombination velocity.

The second part of the experiment consisted of successively etching the cells using the same H$_2$SO$_4$:H$_2$O$_2$:H$_2$O etch and extracting J_{01} after each etch. If the measured J_{01} is dominated by electron injection into the emitter, and if this current is described by (2), then a plot of $1/J_{01}$ versus etch time should be linear. The results of successive etch experiments on both cells confirmed this expectation; the data for Cell 2, with the more heavily doped emitter, are displayed in Fig. 4. From the measured slope of $1/J_{01}$ versus etch time, the measured etch rate of 20Å/sec, and (2), we obtain a second estimate for the $n_{ie}^2 D_n$ product. These results are also listed in Table 1 and are observed to be slightly greater than those obtained by the first method. The difference is easily explained; in contrast to the first approach, the second does not require knowledge of the front surface recombination velocity.

III. DISCUSSION

Information on minority carrier electron mobility and on n_{ie} in p-type GaAs is still sparse, but some comparison with previous work is possible. Walukiewicz et al. [3] have presented theoretical calculations for electron mobility in p-GaAs which show that the electron mobility in p-GaAs is significantly affected by the presence of heavy holes. For high carrier concentrations, the electron mobility in p-GaAs is found to be substantially less than the electron mobility in comparably doped n-GaAs. Ahrenkiel and associates have recently reported transient photoconductivity measurements from which they deduce D_n for p-type GaAs doped with magnesium in the 10^{17}-10^{18} cm^{-3} range [6]. They find general agreement with the theory of Walukiewicz if a compensation ratio of 0.3-0.5 is assumed. The effective intrinsic carrier concentration versus doping density can be estimated from

$$ n_{ie}^2 = n_{io}^2 \, e^{\Delta E_G/k_B T} \, \frac{\mathcal{F}_{1/2}(\eta)}{e^\eta} , \tag{3} $$

where n_{io} is the intrinsic carrier concentration in lightly doped GaAs, ΔE_G is the bandgap shrinkage, and $\mathcal{F}_{1/2}$ is the Fermi-Dirac integral of order one-half with $\eta = (E_V - E_F)/k_B T$. The last factor accounts for majority carrier degeneracy. We estimate n_{ie}^2 from (3) by using the data of Blakemore for n_{io} [7] and that of Casey and Stern for ΔE_G [4].

In Fig. 5, we plot $n_{ie}^2 D_n$ versus hole concentration as obtained by combining the results of Walukiewicz et al., Casey and Stern, and Blakemore. The product is plotted for uncompensated p-GaAs and for a compensation ratio of 0.5. The results obtained from the experiments described in this chapter are also displayed. Both the estimate, and our experimental results show that the $n_{ie}^2 D_n$ product decreases with hole concentration — in contrast to the observations of Slotboom and DeGraaff for p-silicon [2]. While it is impossible to ascertain either n_{ie} or D_n from these results, Fig. 5 does show
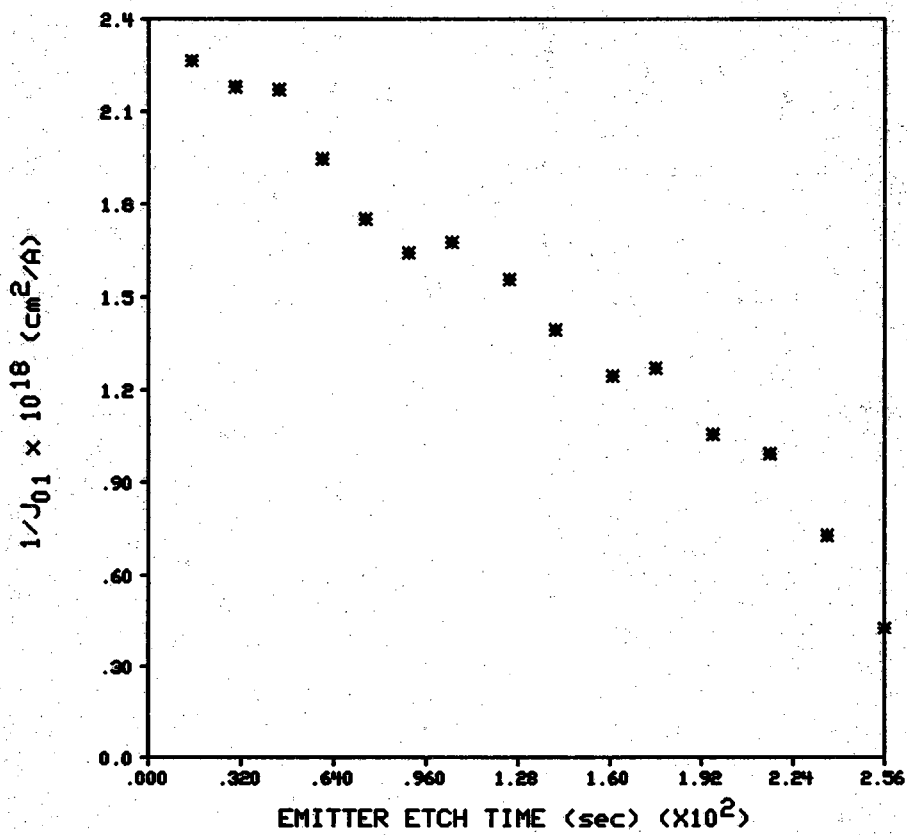
Figure 4   Plot of the inverse n=1 saturation current density versus etch time for the cell with the heavily doped emitter.
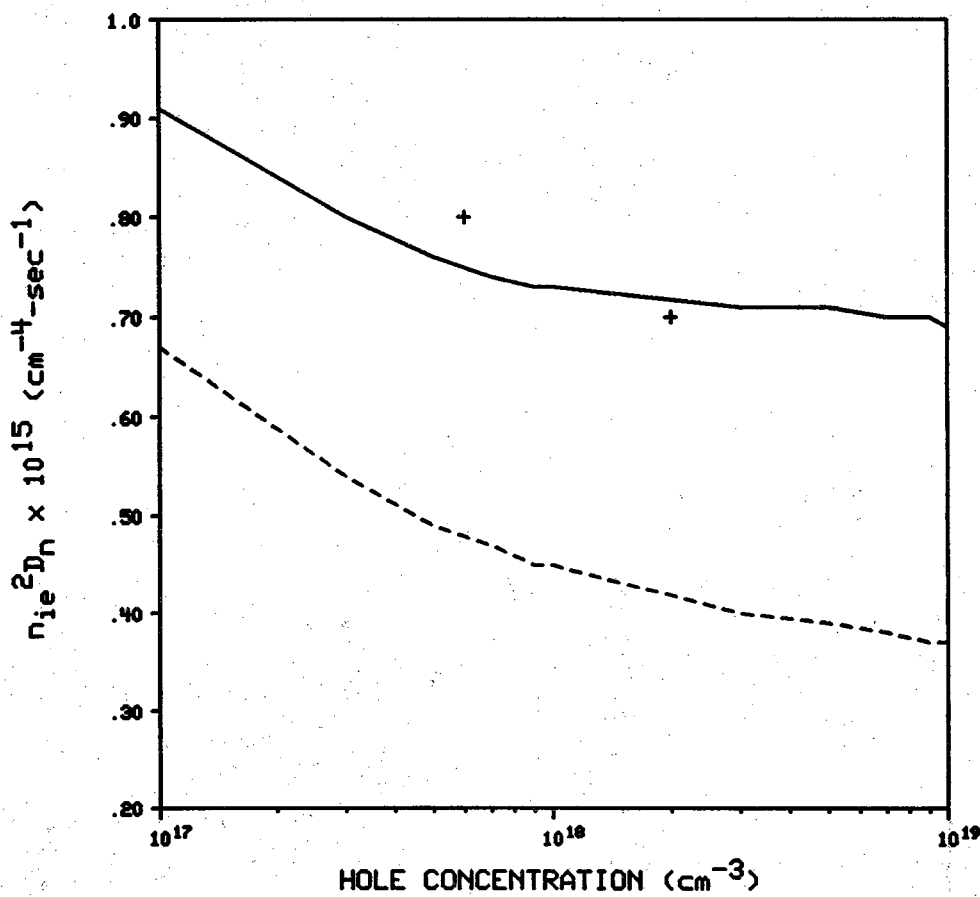
Figure 5   The product $n_{ie}^2 D_n$ versus hole concentration. The solid and dashed lines were computed from the data of Walukiewicz et al. [3], Casey and Stern [4], and Blakemore [7] for compensation ratios of 0.0 and 0.5. The points are the results reported in this chapter.

that the product can be explained from previous work, and that bandgap shrinkage is not a controlling factor in the emitters typically doped p/n heteroface cells.

If extended to lower and higher hole concentrations, data for the $n_{ie}^2 D_n$ product could provide adequate information for modeling the steady-state performance of many bipolar devices. Knowledge of the minority carrier diffusion coefficient itself, however, is essential for modeling transient aspects of device performance such as the base transit time in a bipolar transistor. Although it is impossible to ascertain the value of D_n from these measurements, we should note that the use of optically measured bandgaps in (3) tends to underestimate n_{ie}^2 for silicon [1]. Recent theoretical work by Bennett and Lowney [8] predicts an n_{ie} about twice that obtained from (3) and would therefore require a very low minority carrier diffusion coefficient (corresponding to a compensation ratio of 80% in Walukiewicz's theory). To provide accurate parameters for modeling and analyzing GaAs-based bipolar devices, further work to clarify these issues and to extend the measurements to a broader range of hole concentrations and dopant types is required.

CHAPTER 2 REFERENCES

[1]   J. del Alamo, "Minority Carrier Transport in Heavily Doped N-Type Silicon," Ph.D. Thesis, Stanford University, 1985.

[2]   J.W. Slotboom and H.C. DeGraaff, *Solid-State Electron.,* Vol. 19, pp. 857-862, 1976.

[3]   W. Walukiewicz, J. Lagowski, L. Jastrzebski, and H.C. Gatos, *J. Appl. Phys.,* Vol. 50, pp.5040-5042, 1979.

[4]   H.C. Casey and F. Stern, *J. Appl. Phys.,* Vol. 41, p. 631, 1976.

[5]   R.P. Leon, 19th IEEE Photovoltaic Spec. Conf., New Orleans, LA., May 4-8, 1987.

[6]   R. Ahrenkiel, private communication.

[7]   J.S. Blakemore, *J. Appl. Phys.,* Vol. 53, pp. R123-R181, 1982.

[8]   H.S. Bennett and J.R. Lowney, *J. Appl. Phys.,* Vol. 62, pp. 521-527, 1987.

CHAPTER III

APPLICATION OF CURRENT DLTS
TO LARGE AREA SOLAR CELLS

3.1 INTRODUCTION

Deep levels in semiconductors are commonly characterized by capacitance transient measurements (e.g. DLTS). However, in principle, current transients serve equally well and can even provide greater sensitivity in certain cases. The popularity of the capacitance transient techniques is probably due, in large part, to the fact that Lang[1] chose to use capacitance transients in his original DLTS system. This choice seems to have been somewhat arbitrary as he states in his paper that "If there are circumstances where current measurements are desirable...the basic DLTS scheme is applicable to current transients as well as capacitance transients.". Indeed, later workers were forced to use current transients in cases were capacitance measurements were impractical.[2-11] We have chosen to use current transients because the large junction areas of solar cells yield capacitance values that are much too large to be measured on the standard Boonton meter. We have also modified the basic DLTS measurement technique and data analysis. The measurements are made at a constant temperature and the spectra are plotted as a function of an effective emission rate as opposed to the usual plot versus temperature. For this reason we call the new technique emission DLTS or eDLTS. By taking the data at a constant temperature we avoid the problem of temperature hysteresis. More importantly, errors caused by unaccounted-for temperature dependencies are eliminated. Okushi and Tokumaru[12] measured capacitance transients at a constant temperature but their analysis involved numerical differentiation of the data and plotting of the spectra as a function of time. Our technique avoids the problems of numerical differentiation and also explicitly displays the trap emission rates on the "x axis" of the eDLTS plots.

In the remainder of this chapter we present the theory of the eDLTS technique, describe the experimental setup, present experimental data, and finally summarize our results.

3.2 THEORY †

In the standard DLTS measurement a capacitance or current transient is sampled at two different times and the difference of the sampled values is plotted as a function of temperature. Thus a signal is defined as

$$\Delta C(T) = C_{D.C.} \frac{N_T}{2N_D} \left[\frac{e_n}{e_n + e_p} \right] \left[e^{-(e_n + e_p)t_2} - e^{-(e_n + e_p)t_1} \right] \tag{1}$$

for capacitance transients where $C_{D.C.}$ is the steady state reverse bias capacitance, N_T is the trap concentration, N_D is the ionized shallow donor concentration, e_n is the trap thermal emission rate for electrons, e_p is the trap thermal emission rate for holes, and t_1 and t_2 are the two sample times ‡; and

---

†For simplicity we present the theory for N-type semiconductors only; of course all results can be easily converted to the P-type case.
‡ t_2/t_1 is kept constant.

$$\Delta I(T) = \tfrac{1}{2}qWA(e_n - e_p)N_T \left[\frac{e_n}{e_n + e_p} \right] \left[e^{-(e_n + e_p)t_2} - e^{-(e_n + e_p)t_1} \right] \qquad (2)$$

for current transients where q is the magnitude of the electron charge, W is the reverse bias depletion width, and A is the junction area. The signal, $\Delta C(T)$ or $\Delta I(T)$, will peak when $\dfrac{\partial \Delta C(T)}{\partial T}$ or $\dfrac{\partial \Delta I(T)}{\partial T} = 0$. In the standard theory it is assumed that all of the temperature dependence of $\Delta C(T)$ or $\Delta I(T)$ is found in the term $\left[e^{-(e_n + e_p)t_2} - e^{-(e_n + e_p)t_1} \right]$, but in fact the terms $C_{D.C.} \dfrac{N_T}{2N_D} \left[\dfrac{e_n}{e_n + e_p} \right]$ and $\tfrac{1}{2}qWA(e_n - e_p)N_T \left[\dfrac{e_n}{e_n + e_p} \right]$ may contribute a significant temperature dependence to $\Delta C(T)$ and $\Delta I(T)$, respectively, since e_n and e_p are strong functions of temperature and $C_{D.C.}$ may also be temperature dependent. This additional temperature dependence introduces error in the usual DLTS data analysis. eDLTS however, avoids this error since the data is measured at a constant temperature and plotted as a function of an effective emission rate, e^*. Thus the eDLTS peak occurs when $\dfrac{\partial \Delta C(e^*)}{\partial e^*}$ or $\dfrac{\partial \Delta I(e^*)}{\partial e^*} = 0$, and the dependence of $\Delta C(e^*)$ or $\Delta I(e^*)$ on e^* is much more well behaved than that of $\Delta C(T)$ or $\Delta I(T)$ on T.

A typical eDLTS bias pulse sequence is shown in Figure 1. The diode is held at a constant reverse bias and then briefly pulsed to a more positive bias, just as in regular DLTS.
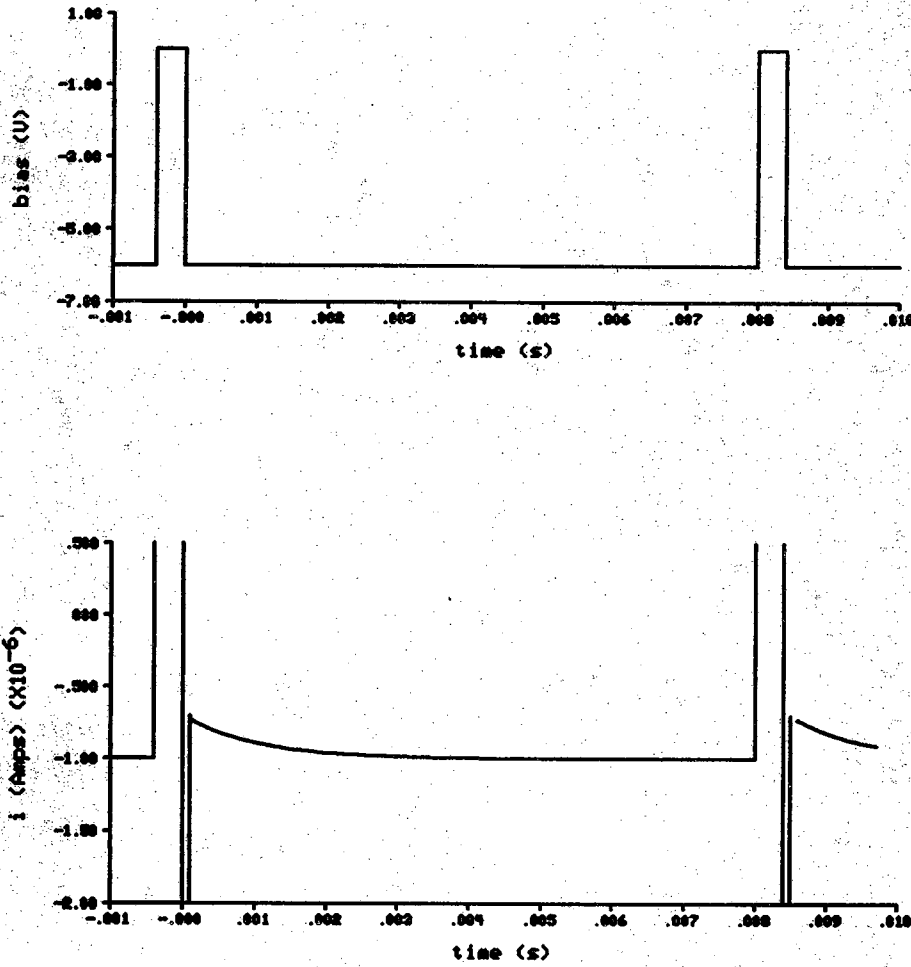
Figure 1.   eDLTS bias pulse train and current transient.

During the reverse bias period traps thermally emit captured carriers resulting in the current transient[13]

$$i(t) = -\tfrac{1}{2}qWA\left[e_p N_T + (e_n - e_p)n_T(t)\right] \qquad (3)$$

where $n_T(t)$ is the concentration of the traps that are filled by electrons at time t. The eDLTS signal is obtained by sampling the current transient at two different times, and plotting the difference of the sampled values as a function of an effective emission rate. The signal is defined as

$$\Delta I(t_1) \equiv i(t_2) - i(t_1)$$

$$= -\tfrac{1}{2}qWA(e_n - e_p)\left[n_T(t_2) - n_T(t_1)\right]. \qquad (4)$$

If the traps are completely filled with electrons at time t=0, then

- 33 -

$$n_T(t) = N_T\left[\left(\frac{e_n}{e_p + e_n}\right)e^{-(e_p + e_n)t} + \frac{e_p}{e_p + e_n}\right].$$

(5)

Substituting Equation (5) in Equation (4)

$$\Delta I(t_1) = -\tfrac{1}{2}qWA(e_n - e_p)N_T\left[\frac{e_n}{e_p + e_n}\right]\left[e^{-(e_p + e_n)t_2} - e^{-(e_p + e_n)t_1}\right].$$

(6)

Typically either $e_n \gg e_p$ or $e_n \ll e_p$ and so

$$\Delta I(t_1) \cong -\tfrac{1}{2}qWAe_nN_T\left[e^{-e_nt_2} - e^{-e_nt_1}\right]$$

$$= \Delta i\left[e^{-e_nt_2} - e^{-e_nt_1}\right], \quad e_n \gg e_p$$

(7)

and

$$\Delta I(t_1) \cong \tfrac{1}{2}qWAe_nN_T\left[e^{-e_pt_2} - e^{-e_pt_1}\right]$$

$$= \Delta i\left[e^{-e_pt_2} - e^{-e_pt_1}\right], \quad e_n \ll e_p$$

(8)

where $\Delta i \equiv i(0) - i(\infty)$. The eDLTS signal, $\Delta I(t_1)$, will peak when $\dfrac{\partial \Delta I(t_1)}{\partial t_1} = 0$. Differentiating Equations (7) and (8) with respect to t_1 and setting the result equal to zero yields

$$t_1 = \frac{\ln(t_2/t_1)}{e_n(t_2/t_1 - 1)}$$

(9)

and

$$t_1 = \frac{\ln(t_2/t_1)}{e_p(t_2/t_1 - 1)}$$

(10)

respectively. We next define the effective emission rate e^* as

$$e^* \equiv \frac{\ln(t_2/t_1)}{t_1(t_2/t_1 - 1)}.$$

(11)

Then Equations (7) and (8) can be rewritten in terms of e^* as

$$\Delta I(e^*) \cong \Delta i\left[e^{-(e_n/e^*)c_2} - e^{-(e_n/e^*)c_1}\right]$$

(12)

and

$$\Delta I(e^*) \cong \Delta i\left[e^{-(e_p/e^*)c_2} - e^{-(e_p/e^*)c_1}\right]$$

(13)

respectively, where

$$c_2 \equiv \frac{t_2}{t_1}\frac{\ln(t_2/t_1)}{(t_2/t_1 - 1)}$$

(14)

$$= \text{constant},$$

and

$$c_1 \equiv \frac{\ln(t_2/t_1)}{(t_2/t_1 - 1)}$$ (15)

$$= \text{constant.}$$

From Equations (9), (10), and (11) it is seen that the eDLTS signal will peak when e^* is equal to the trap's thermal emission rate, e_n or e_p. The value of $\Delta I(e^*)$ at the peak is

$$\Delta I(e^* = e_{\text{thermal}}) = \Delta i \left[e^{-c_2} - e^{-c_1} \right]$$

where $e_{\text{thermal}} = e_n$ or e_p. By plotting $\Delta I(e^*) \left[e^{-c_2} - e^{-c_1} \right]^{-1}$ versus e^* one obtains eDLTS peaks that are located at $e^* = e_{\text{thermal}}$ and have amplitudes equal to Δi. The data can easily be normalized by plotting $\Delta I(e^*)/\Delta I(e^* = e_{\text{thermal}})$ versus e^*/e_{thermal}. Moreover, a universal eDLTS curve can be obtained by setting $\Delta i = 1 = e_{\text{thermal}}$ in Equation (12) or (13). Experiment can then be compared with theory by superimposing normalized experimental data on the universal eDLTS curve.

3.3 EXPERIMENTAL SETUP

A Polaron S4600 DLTS system provided the pulse excitation, cryostat, and temperature control for the eDLTS measurements. The current transient was measured and amplified by a 5 stage operational amplifier circuit that was designed and built in our laboratory. Stage one is a current-to-voltage converter with a gain of 100 V/A. Stage two is a differential amplifier with a gain of 100 V/V. The differential amplifier provides the capability for offsetting the solar cell leakage current. Stages three, four, and five are inverting amplifiers each having a gain of 10 V/V. These last three stages can be switched into the circuit in succession thus providing overall system gains of 10^4, 10^5, 10^6, and 10^7 V/A. The transient waveform was digitized and stored on a Tektronix 11401 digitizing oscilloscope. The 11401 is interfaced to the Purdue Engineering Computer Network, thus the digitized transient waveform can be uploaded for data processing. We have written and tested software for analyzing the transient waveforms and generating the eDLTS plots. The system is fully operational as of this writing.

3.4 EXPERIMENTAL DATA

To date, eDLTS has been performed on a 0.5×0.5 cm^2 MOCVD GaAs solar cell. Figure 2 shows the as-measured eDLTS spectra.
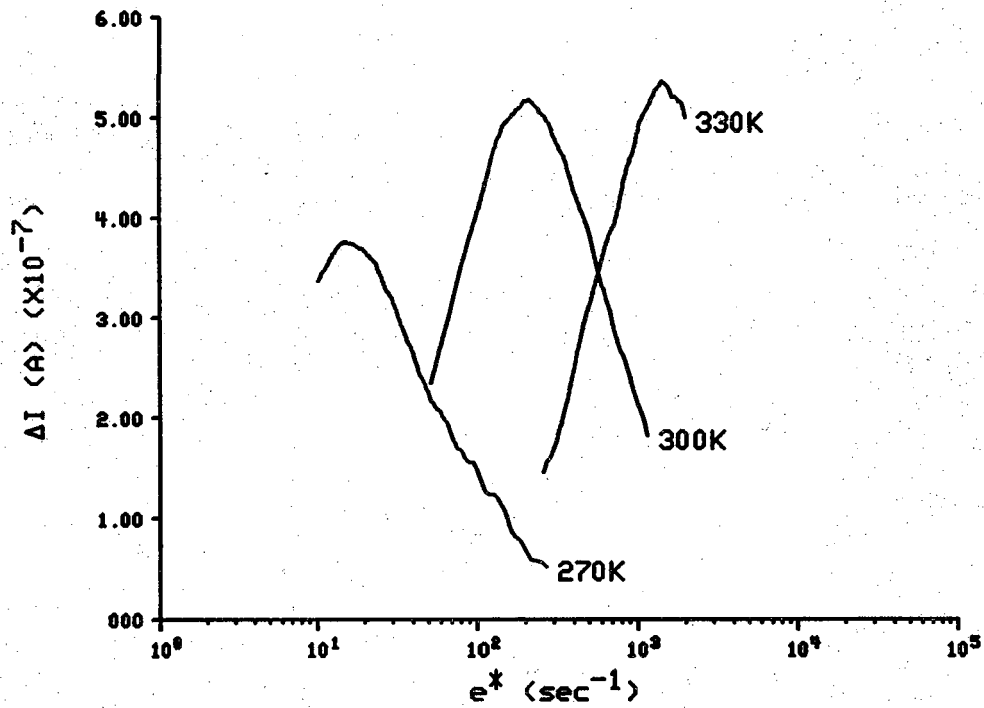
Figure 2.   eDLTS spectra for $t_2/t_1 = 3$.

The amplitude of each peak corresponds to the magnitude, Δi, of the current transient and the location of each peak corresponds to the trap thermal emission rate at the specified temperature. The data for each of the three peaks was normalized and superimposed on the universal eDLTS curve, as shown in Figures 3-5.
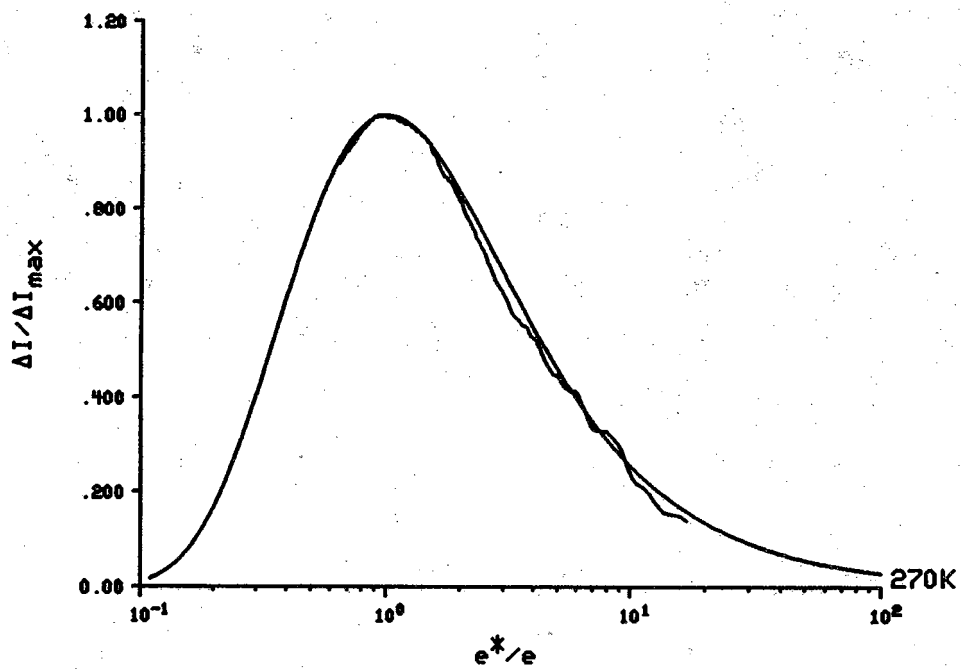
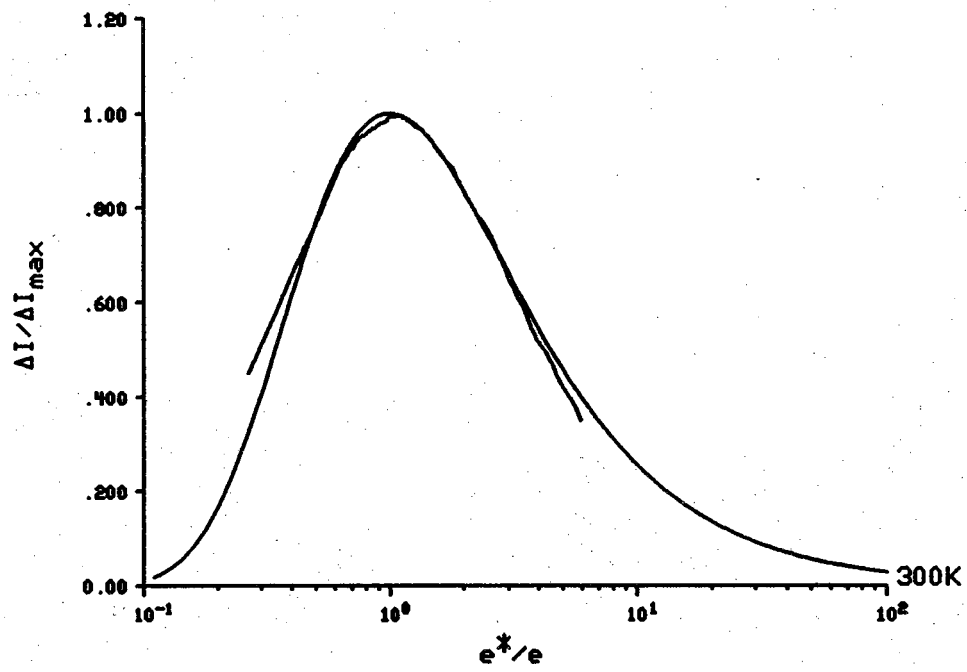Figure 3.   Normalized eDLTS spectra for 270K peak, $\Delta i = 0.38 \mu A$, $e_p = 16$ s^{-1}.

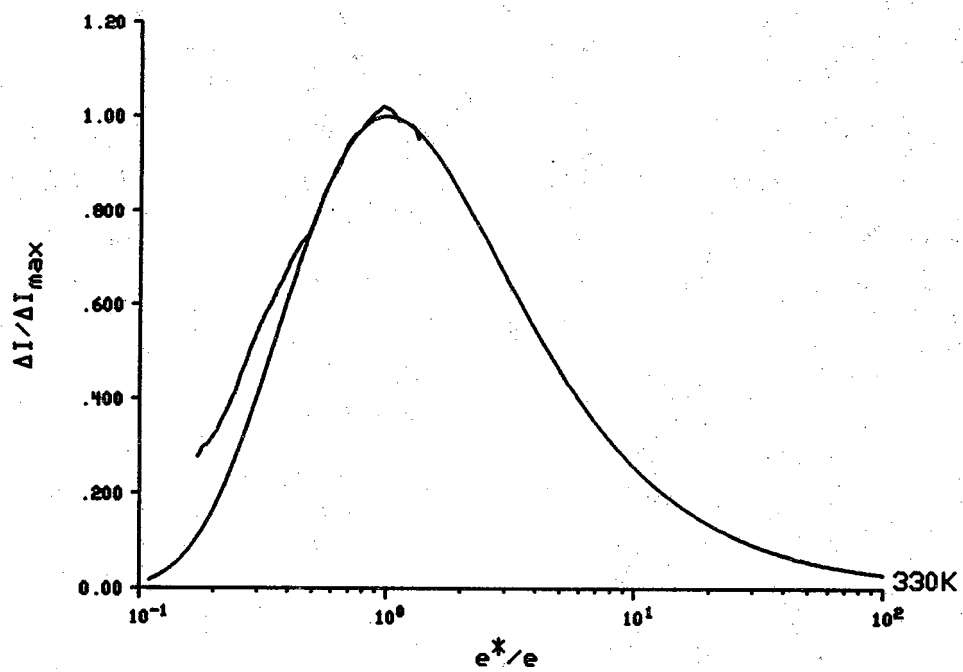Figure 4.   Normalized eDLTS spectra for 300K peak, $\Delta i = 0.52\mu A$, $e_p = 195 \text{ s}^{-1}$.

Figure 5.   Normalized eDLTS spectra for 330K peak, $\Delta i = 0.53 \mu A$, $e_p = 1,500$ s^{-1}.

The shape of the current transient for this data indicated that $e_n < e_p$ for this particular deep level. For this case Equation (8) applies. Using the data for the 300K peak, namely

$$\Delta i = 0.52 \mu A$$

$$A = 0.25 cm^2$$

and

$$W = 2422 Å \text{ at } -6 \text{ volts,}$$

Equation (8) yields

$$e_n N_T \cong 1.07 \times 10^{18} \ (cm^{-3} - s^{-1}).$$

Unfortunately, we were not able to determine the separate values for either e_n or N_T for this trap. This is because the trap is a hole emitter ($e_n < e_p$) thus the time constant for the current transient only provides information on e_p. For diodes having negligible leakage current, both e_p and e_n can be determined from the measured values of $i(t=0)$ and $i(t=\infty)$, with the help of Equations (3) and (5).

The deep level thermal activation energy and carrier capture cross section are commonly determined from the slope and intercept, respectively, of a plot of $\log \left[\dfrac{e_p}{T^2} \right]$

versus $\left[\dfrac{1000}{T}\right]$ (an Arrhenius plot). The Arrhenius plot for the data of Figure 2 is shown in Figure 6.
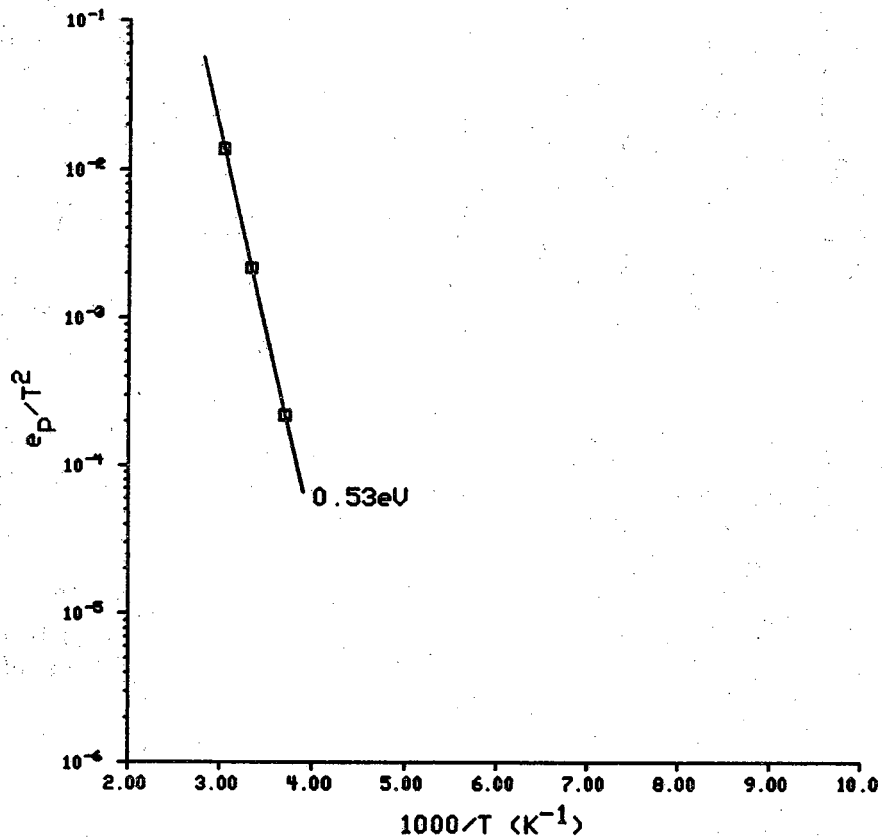

Figure 6.   Arrhenius Plot for the eDLTS spectra of Figure 2.

$E_T - E_V$ and σ_p are determined from the Arrhenius plot to be

$$E_T - E_V = 0.53\text{eV}$$

and

$$\sigma_p = 1.1 \times 10^{-15}\text{cm}^2.$$

The measured trap parameters are summarized in the table below. Also shown in the table are the reported[14] thermal activation energy and capture cross section for holes due to Fe.

Identity	$E_T - E_V$ (eV)	σ_p (10^{-15} cm^2)
measured	0.53	1.1
Fe (reported)	0.52	0.3

3.5 SUMMARY

The relatively large areas of solar cells make defect characterization by capacitance transient methods (DLTS) impractical due to overloading of the capacitance meter. For this reason we have chosen to work with current transients. Current sensing and amplifying circuitry has been designed and built, data processing software has been developed and implemented, and the resulting system has been used to characterize deep levels in a 0.25 cm^2 MOCVD GaAs solar cell. The measured trap parameters for the dominant deep level detected are similar to published[14] data for Fe. The standard DLTS technique has been modified in that measurements have been made at constant temperature and DLTS spectra have been plotted as a function of an effective emission rate. Errors due to temperature hysteresis and unaccounted for temperature dependencies have thus been eliminated.

CHAPTER 3 REFERENCES

References

1. D.V. Lang, "Deep-Level Transient Spectroscopy: A New Method to Characterize Traps in Semiconductors," *J. Appl. Phys.*, vol. 45, no. 7, p. 3023, July 1974.

2. B.W. Wessels, "Determination of Deep Levels in Cu-Doped GaP using Transient-Current Spectroscopy," *J. Appl. Phys.*, vol. 47, no. 3, p. 1131, March 1976.

3. P.M. Petroff and D.V. Lang, "A New Spectroscopic Technique for Imaging the Spatial Distribution of Nonradiative Defects in a Scanning Transmission Electron Microscope," *Appl. Phys. Lett.*, vol. 31, no. 2, p. 60, 15 July 1977.

4. Ch. Hurtes, M. Boulou, A. Mitonneau, and D. Bois, "Deep-Level Spectroscopy in High-Resistivity Materials," *Appl. Phys. Lett.*, vol. 32, no. 12, p. 821, 15 June 1978.

5. D. Pons, P.M. Mooney, and J.C. Bourgoin, "Energy Dependence of Deep Level Introduction in Electron Irradiated GaAs," *J. Appl. Phys.*, vol. 51, no. 4, p. 2038, April 1980.

6. J.A. Borsuk and R.M. Swanson, "Current Transient Spectroscopy: A High-Sensitivity DLTS System," *IEEE Trans. Electron. Dev.*, vol. ED-27, no. 12, p. 2217, December 1980.

7. K. Kosai, "Electron Traps in ZnSe Grown by Liquid-Phase Epitaxy," *J. Appl. Phys.*, vol. 53, no. 2, p. 1018, February 1982.

8. J.W. Farmer, C.D. Lamp, and J.M. Meese, "Charge Transient Spectroscopy," *Appl. Phys. Lett.*, vol. 41, no. 11, p. 1063, 1 December 1982.

9. P.M. Mooney, "Photo-Deep Level Transient Spectroscopy: A Technique to Study Deep Levels in Heavily Compensated Semiconductors," *J. Appl. Phys.*, vol. 54, no. 1, p. 208, January 1983.

10. M.O. Watanabe, K. Morizuka, M. Mashita, Y. Ashizawa, and Y. Zohta, "Donor Levels in Si-Doped AlGaAs Grown by MBE," *Japan. J. Appl. Phys.*, vol. 23, no. 2, p. L103, February 1984.

11. I.D. Hawkins and A.R. Peaker, "Capacitance and Conductance Deep Level Transient Spectroscopy in Field-Effect Transistors," *Appl. Phys. Lett.*, vol. 48, no. 3, p.

227, 20 January 1986.

12. H. Okushi and Y. Tokumaru, "Isothermal Capacitance Transient Spectroscopy for Determination of Deep Level Parameters," *Japan. J. Appl. Phys.*, vol. 19, no. 6, p. L335, June 1980.

13. C.T. Sah, L. Forbes, L.L. Rosier, and A.F. Tasch, Jr., "Thermal and Optical Emission and Capture Rates and Cross Sections of Electrons and Holes at Imperfection Centers in Semiconductors from Photo and Dark Junction Current and Capacitance Experiments," *Solid-St. Electron.*, vol. 13, p. 759, 1970.

14. A. Mitonneau, G.M. Martin, and A. Mircea, "Hole Traps in Bulk and Epitaxial GaAs Crystals," *Electron. Lett.*, vol. 13, p. 666, 1977.

APPENDIX: PUBLICATIONS

This appendix contains reprints of the publications which resulted from the work conducted during the past year.

[1] M.R. Melloch, C.P. MaMahon, M.S. Lundstrom, J.A. Cooper, Jr. and Q.-D. Quian, "Photocollection Efficiency of GaAs/AlAs/GaAs p^+—i—n and n^+—i—p Photodiodes," *Solar Cells,* Vol. 21, pp. 233-240, 1987.

[2] P.D. DeMoulin, C.S. Kyono, M.S. Lundstrom, and M.R. Melloch, "Dark IV Characterization of P/N Heteroface Cells," presented at the 19th IEEE Photovoltaic Specialists Conf., New Orleans, LA., May 1987.

[3] M.E. Klausmeier-Brown, C.S. Kyono, D.P. Rancour, M.S. Carpenter, M.R. Melloch, M.S. Lundstrom, and R.F. Pierret, "Experimental Characterization of Minority Carrier Mirrors for Gallium Arsenide-based Solar Cells," presented at the 19th IEEE Photovoltaic Specialists Conf., New Orleans, LA., May 1987.

[4] D. P. Rancour, M.R. Melloch, R.F. Pierret, M.S. Lundstrom, M.E. Klausmeier-Brown, and C.S. Kyono, "Recombination Current Suppression in GaAs P-N Junctions on AlGaAs Buffer Layers Grown by Molecular Beam Epitaxy," *J. Appl. Phys.,* Vol. 62, pp. 1539-1541, 1987.

[5] M.R. Melloch, C.P. McMahon, M.S. Lundstrom, J.A. Cooper, Jr., Q-D. Qian, and S. Bandyopadhyay, "Bias-Dependent Photoresponse of p^+—i—n GaAs/AlAs/GaAs Diodes," *Appl. Phys. Lett., Vol. 50, pp. 161-163, 1986.*

PHOTOCOLLECTION EFFICIENCY OF GaAs/AlAs/GaAs p+-i-n AND n+-i-p PHOTODIODES*

M. R. MELLOCH, C. P. McMAHON, M. S. LUNDSTROM, J. A. COOPER, JR. and Q.-D. QIAN

School of Electrical Engineering, Purdue University, West Lafayette, IN 47907 (U.S.A.)

Summary

Measurements of the photocollection efficiency of GaAs/AlAs/GaAs diodes are reported. The quantum efficiency measurements demonstrate that the conduction band discontinuity between AlAs and GaAs is small — most of the band gap discontinuity is accommodated by the valence band. These results suggest that series resistance may be a problem in p-type heteroface cells (owing to the large majority carrier barrier); n-type hetero-faces should display low series resistance due to the isotype heterojunction, even when the junction is not intentionally graded.

1. Introduction

Heterojunctions have several applications in advanced high efficiency solar cells. When they are used as a window layer in heteroface cells, surface recombination losses are reduced and heterojunction back-surface fields have recently been shown to increase open-circuit voltage [1]. A number of novel cell designs based on heterojunctions have also been proposed [2 - 5]. A key heterojunction parameter is the band line-up which describes how the difference in band gaps is distributed between the conduction and valence bands. There has been considerable effort to determine the band alignment between GaAs and $Al_xGa_{1-x}As$ during the past several years [6 - 15]. The majority of the work has dealt with aluminum mole fractions where $0 < x < 0.4$, a range of mole fractions of interest for devices such as modulation-doped field effect transistors. For this compositional range, the conduction band discontinuity (from Γ GaAs to Γ AlGaAs) is at present believed to be between 0.6 and 0.65 of the band gap difference.

In heteroface solar cell applications, much larger aluminum mole fractions ($x \approx 0.9$) are typically used to obtain a wide indirect band gap which allows most of the light to be collected in the underlying GaAs regions.
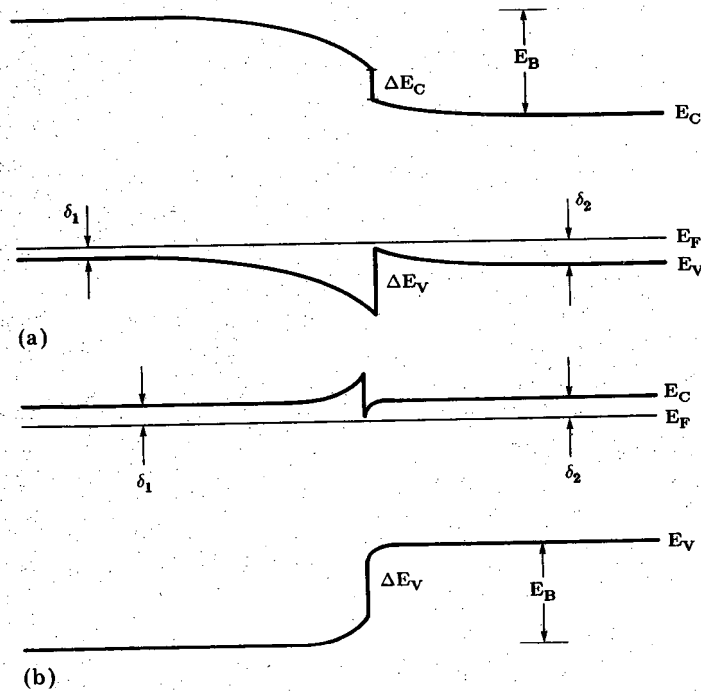
Fig. 1. Energy band diagrams of AlAs/GaAs heterofaces: (a) p-type heteroface; (b) n-type heteroface.

Figure 1(a) shows the energy band diagram of a p-type heteroface; the energy band diagram of an n-type heteroface is shown in Fig. 1(b). The confining barrier for minority carriers is readily shown to be

$$E_B = (E_{G2} - E_{G1}) + \delta_2 - \delta_1$$

which depends only on the band gap difference and not on how this difference is distributed between the conduction and valence bands. The barrier to majority carrier flow, however, is related directly to the majority carrier band discontinuity. Work on heterojunction bipolar transistors has demonstrated that these barriers must be intentionally removed (e.g. by compositional grading) if a low series resistance is to be achieved.

The results of band alignments for aluminum mole fractions below $x = 0.4$ (direct band gap alloy) cannot be extrapolated to heterojunctions with mole fractions where $0.4 < x < 1.0$ (indirect alloy). Very recently, investigators have found evidence that the conduction band discontinuity from Γ GaAs to X AlGaAs (in the indirect alloy) is significantly below 60% of the indirect band gap difference. For the AlAs–GaAs heterojunction the band gap difference is about 0.75 eV. These recent reports place 0.1 - 0.2 eV of this band gap difference in the conduction band discontinuity from Γ GaAs to X AlAs and 0.55 - 0.65 eV in the valence band discontinuity [11, 13, 15].

If a large difference in size in the conduction and valence band discontinuities exists, there should be a measurable difference in the ability of

a GaAs/AlAs heterojunction to block electrons and holes. In this paper we present our investigations of these minority carrier barriers by measuring the relative photocollection efficiencies in GaAs/AlAs/GaAs p^+–i–n and n^+–i–p photodiodes. The results demonstrate that the band discontinuity between AlAs and GaAs is mostly accommodated by the valence band as suggested in Fig. 1. These results suggest that the series resistance of n–p AlAs/GaAs heteroface cells should be low, but for p–n heteroface cells compositional grading may be required to remove the majority carrier barrier.

2. Device fabrication

The films used in this work were grown in a Perkin–Elmer PHI400 molecular beam epitaxy (MBE) system. Typical device structures are displayed in Fig. 2. The starting substrates were (100) cut and either p type (zinc doped to 1×10^{19} cm^{-3}) or n type (silicon doped to 1.5×10^{18} cm^{-3}) depending on whether an n^+–i–p or p^+–i–n photodiode was being fabricated. The lightly doped (10^{16} cm^{-3}) buffer layers were grown at a substrate temperature of 600 °C, followed by an undoped AlAs layer grown at 700 °C. Finally the heavily doped (10^{18} cm^{-3}) top GaAs layer was grown at 600 °C. Silicon was used as the n-type dopant and beryllium as the p-type dopant in the MBE films. Devices of dimensions 300 μm $\times$ 300 μm were defined by photolithography and subsequent wet etching. Ohmic contacts of dimensions 100 μm $\times$ 100 μm were then made to the top GaAs layers.
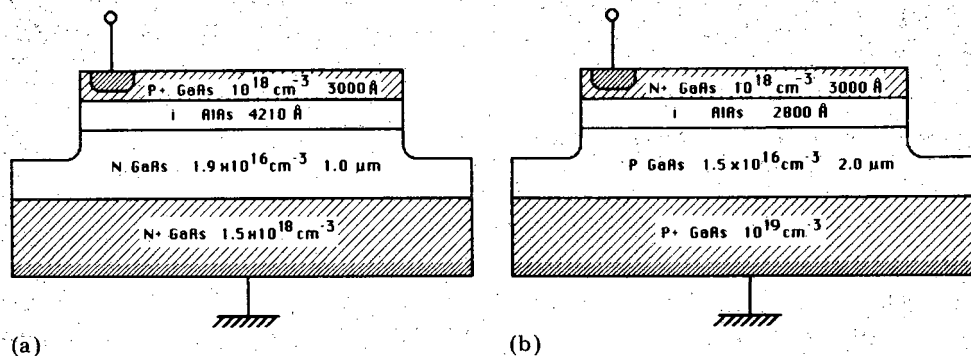

(a)   (b)

Fig. 2. GaAs/AlAs/GaAs device structures: (a) p^+–i–n structure; (b) n^+–i–p structure.

3. Results

The p^+–i–n and n^+–i–p photodiodes can be thought of as metal/insulator/semiconductor structures where the top heavily doped GaAs region acts as a gate. We have previously investigated structures similar to those described in Section 2 using photosensitive capacitance–voltage (C–V) techniques [16, 17]. Figure 3 shows the C–V characteristic of a p^+–i–n
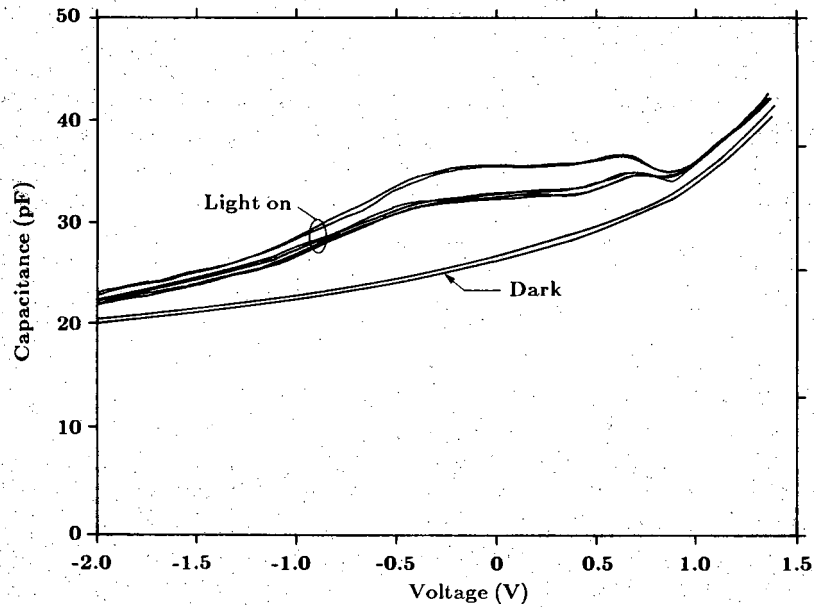
Fig. 3. Dark and illuminated $C-V$ characteristics of a p^+-i-n GaAs/AlAs/GaAs structure at 77 K. Each capacitance curve was swept in both directions.

GaAs/AlAs/GaAs structure in the dark and with two different intensities of illumination from a microscope light; these measurements were made at a temperature of 77 K. (The $C-V$ data displayed in Fig. 3 were measured on a device whose AlAs barrier was 1700 Å thick.) In the dark, one observes the expected deep depletion characteristic; there is also no accumulation of electrons at the underlying AlAs/n-GaAs heterojunction. With the addition
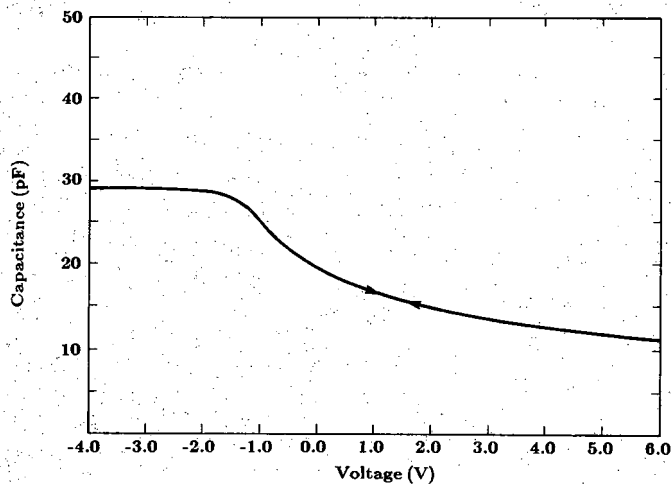

Fig. 4. Dark $C-V$ characteristic of an n^+-i-p GaAs/AlAs/GaAs structure at 77 K (frequency, 100 kHz). The capacitance curve was swept in both directions.

of the light, an inversion layer of holes is observed in the $C-V$ characteristic corresponding to the observed ledge formation.

The $C-V$ characteristic of an n^+–i–p GaAs/AlAs/GaAs structure is shown in Fig. 4. (The $C-V$ data displayed in Fig. 4 were measured on a device whose AlAs barrier was 2800 Å thick.) In this characteristic, one observes an accumulation of holes at the underlying AlAs/p-GaAs hetero-
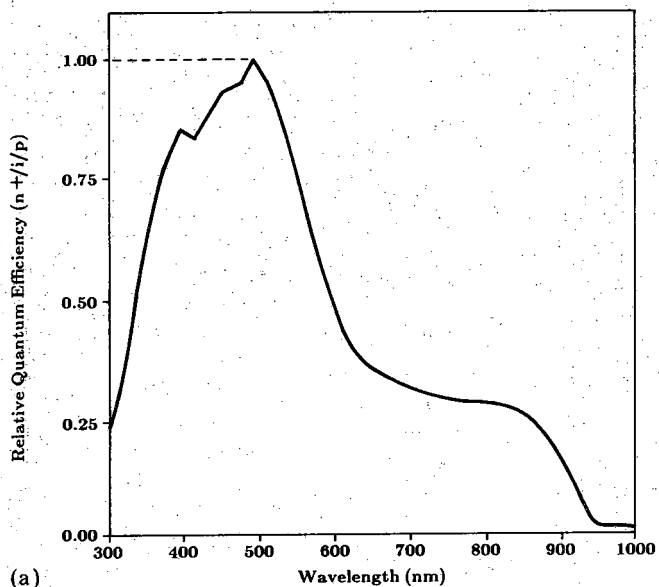
(a)
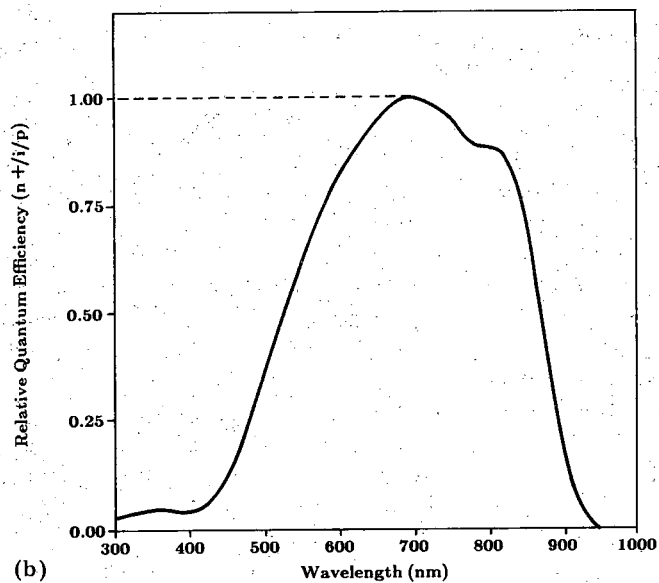
(b)

Fig. 5. Relative quantum efficiency for the GaAs/AlAs/GaAs structures: (a) p^+–i–n structure; (b) n^+–i–p structure.

junction corresponding to gate voltages of -4 V $< V_g < -1$ V; a deep depletion characteristic is observed for $V_g > -1$ V. With illumination and at an a.c. signal frequency of 100 kHz, the p^+-i-n structures showed no evidence of the formation of an electron inversion layer ledge. The lack of electron accumulation in the p^+-i-n device and the lack of evidence of an electron inversion layer in our n^+-i-p devices may be a consequence of a small conduction band discontinuity from Γ GaAs to X AlAs.

The effect of the barriers at the AlAs-GaAs interface on minority carriers can also be investigated by measuring the photocollection efficiency of these structures. The relative quantum efficiencies are shown in Figs. 5(a) and 5(b) for the p^+-i-n and n^+-i-p devices whose dimensions are shown in Figs. 2(a) and 2(b) respectively. The zero-bias energy band diagrams for these structures are shown in Figs. 6(a) and 6(b).
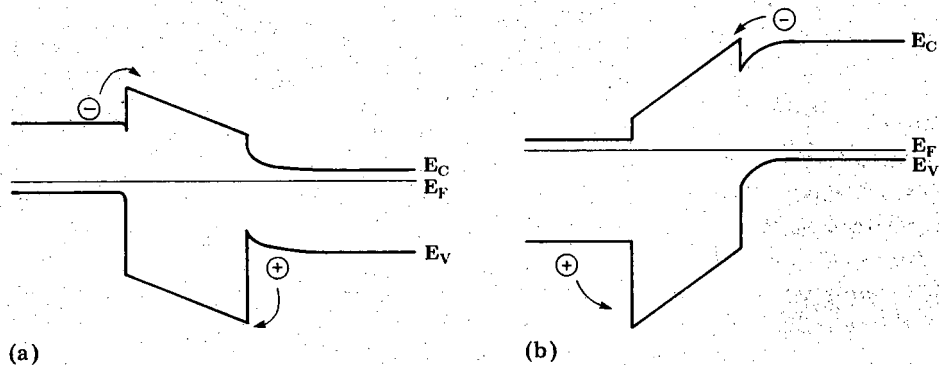

Fig. 6. Energy band diagrams under zero bias for the GaAs/AlAs/GaAs structures: (a) p^+-i-n structure; (b) n^+-i-p structure.

The photocollection results can be interpreted with the aid of Table 1, a list of absorption depth in the GaAs/AlAs/GaAs p^+-i-n diode of Fig. 2(a) as a function of wavelength [18]. (We define absorption depth as the distance it takes to absorb 90% of the light.) From the data in Table 1 we see that, near 700 nm, the absorption of light in our structures should shift from being mainly in the GaAs buffer layers (for wavelengths greater than 700 nm) to being mainly in the top heavily doped GaAs regions (for wavelengths less than 700 nm). The direct band gap is 2.95 eV in AlAs at room temperature; we therefore assume that for wavelengths greater than 420 nm there will be no appreciable absorption in the AlAs barriers.

The photocollection efficiency data for the p^+-i-n structure is shown in Fig. 5(a). For light of wavelength $\lambda > 700$ nm, the light is absorbed in the n-GaAs buffer region. The minority carriers are holes which experience a large valence band discontinuity. Hence for 700 nm $< \lambda < 870$ nm one would expect a low collection efficiency as observed in the Fig. 5(a) data. For light of $\lambda < 700$ nm, the absorption is in the top p^+-GaAs region. Here the minority carriers are electrons which experience a smaller conduction band discontinuity from Γ GaAs to X AlAs and the collection efficiency

TABLE 1

Absorption depth *vs.* wavelength

Wavelength (μm)	Absorption depth (μm)
0.400	0.063
0.500	0.077
0.600	0.098
0.650	0.126
0.660	0.140
0.680	0.168
0.700	0.259
0.720	1.347
0.740	1.404
0.760	1.480
0.780	1.593
0.800	1.726
0.850	2.649

increases substantially. As the wavelength decreases below 500 nm the absorption is nearing the top surface of the GaAs and surface recombination begins to lower the collection efficiency.

The photocollection data for the n^+–i–p structure is shown in Fig. 5(b). Again for light of $\lambda > 700$ nm the absorption is in the p-GaAs buffer region. The minority carriers are electrons which experience a small conduction band discontinuity from Γ GaAs to X AlAs and are easily collected. As the wavelength is decreased below 700 nm, the absorption shifts to the n^+-GaAs top layer. Here the minority carriers are holes which experience a relatively large valence band discontinuity and the photocollection efficiency declines.

4. Conclusions

The relative photocollection efficiencies in p^+–i–n and n^+–i–p GaAs/AlAs/GaAs structures were measured. The results demonstrate that the valence band discontinuity at the GaAs–AlAs interface is much more efficient at blocking holes than the conduction band discontinuity from Γ GaAs to X AlAs is at blocking electrons. These results agree with recent reports which place 70% - 85% of the band gap difference in the valence band discontinuity for the GaAs/AlAs heterojunction. The results have significance for heterostructure cell design. They suggest, for example, that lower series resistance may be expected in n-type heterofaces because of the low majority carrier barrier. For p-type heterofaces, the junction may have to be compositionally graded by design to achieve very low series resistance.

Acknowledgment

240

References

1 R. P. Gale, J. C. C. Fan, G. W. Turner and R. L. Chapman, *Proc. 17th IEEE Photovoltaic Specialists' Conf., Kissimmee, FL, 1984*, IEEE, New York, 1984, p. 1422.
2 A. G. Milnes, *14th IEEE Photovoltaic Specialists' Conf., San Diego, CA, 1980*, IEEE, New York, 1980, p. 536.
3 B. Kallback, *Solid-State Electron., 26* (1983) 653.
4 S. C. Lee and G. L. Pearson, *IEEE Trans. Electron Devices, 27* (1980) 844.
5 J. M. Borrego, S. K. Ghandhi and D. A. Page, *Proc. 17th IEEE Photovoltaic Specialists' Conf., Kissimmee, FL, 1984*, IEEE, New York, 1984, p. 729.
6 R. Dingle, W. Weigman and C. H. Henry, *Phys. Rev. Lett., 33* (1978) 750.
7 H. Kroemer, Wu-Yi Chien, H. C. Casey, Jr., and A. Y. Cho, *Appl. Phys. Lett., 33* (1978) 749.
8 H. Kroemer, Wu-Yi Chien, J. S. Harris, Jr., and D. D. Edwall, *Appl. Phys. Lett., 36* (1980) 295.
9 J. R. Waldrop, S. P. Kowalczyk, R. W. Grant, E. A. Kraut and D. L. Miller, *J. Vac. Sci. Technol., 19* (1981) 573.
10 D. Arnold, A. Ketterson, T. Henderson, J. Klem and H. Morkoc, *Appl. Phys. Lett., 45* (1984) 1237.
11 J. Batey and S. L. Wright, *IEEE Device Research Conf., Boulder, CO, June 17 - 19, 1985.*
12 H. Okumura, S. Misawa, S. Yoshida and S. Gonda, *Appl. Phys. Lett., 46* (1985) 377.
13 T. J. Drummond and I. J. Fritz, *Appl. Phys. Lett., 47* (1985) 284.
14 K. L. Tan, M. S. Lundstrom and M. R. Melloch, *Appl. Phys. Lett., 48* (1986) 428.
15 B. A. Wilson, P. Dawson, C. W. Tu and R. C. Miller, *J. Vac. Sci. Technol., B4* (1986) 1037.
16 J. A. Cooper, Jr., Q.-D. Qian and M. R. Melloch, *Appl. Phys. Lett., 48* (1986) 365.
17 Q.-D. Qian, M. R. Melloch and J. A. Cooper, Jr., *Appl. Phys. Lett., 48* (1986) 638.
18 C. Mazier, *Material Models and Device Structures for GaAs Solar Cells, SERI Subcontract Rep.*, 1984 (Solar Energy Research Institute, Golden, CO) (Subcontract XL-3-03124-1).

DARK IV CHARACTERIZATION OF GAAS P/N HETEROFACE CELLS

P.D. DeMoulin, C.S. Kyono, M.S. Lundstrom, and M.R. Melloch
School of Electrical Engineering
Purdue University
West Lafayette, IN 47907

ABSTRACT

Dark current measurements for MOCVD-grown, GaAs, p^+n heteroface solar cells are reported. The results demonstrate that the n=2 (space-charge region) and n=1 (minority carrier diffusion) current components contribute nearly equally to the 1-sun dark current. Under even modest concentration, the diffusion current dominates. Hole injection into the n-base appears to be the dominant component of the diffusion current in conventionally designed heteroface cells, but for these cells, in which the emitter is relatively lightly doped, the emitter component is unexpectedly large. These results suggest that a considerable reduction in the dark current of high-efficiency p/n heteroface cells can be achieved.

I. INTRODUCTION

Although high GaAs cell efficiencies have been achieved [1], our knowledge of minority carrier transport in GaAs is still primitive when compared to the understanding of silicon cell device physics. A quantitative understanding of minority carrier injection and recombination in GaAs is needed to guide solar cell design. Detailed studies which relate the measured dark current to the cell's material and structural parameters are lacking. Little work has been reported on the role of so-called bandgap narrowing effects or the value of minority carrier diffusion coefficients - both important factors in silicon devices. In this paper we report, analyze, and interpret the measured dark I-V characteristics of MOCVD, GaAs, p/n heteroface solar cells. The objective of the work is to identify loss mechanisms in high-efficiency GaAs cells so that new cells, specifically designed to suppress these mechanisms, can be developed. The results of this work suggest that substantial reductions in dark currents can be achieved.

For this study, dark currents were characterized by the expression:

$$J = J_{01}(e^{qV/kT}-1) + J_{02}(e^{qV/2kT}-1), \quad (1)$$

where J_{01} and J_{02}, the saturation current densities for the n=1 and n=2 component currents, were determined by curve fitting as described in the next section. The saturation current density J_{01} can be separated into two component currents — J_{0E}, the emitter component, and J_{0B}, the base component. Simple expressions for J_{0E} can be used because the electron diffusion length is expected to be much greater than the quasi-neutral emitter thickness. For the cells under consideration, we require $\tau_n \gg 0.03$ nanoseconds; τ_n is expected to be roughly 100 times this value in the high-efficiency cells used for this study. Under these conditions, the minority carrier electron distribution within the p-type emitter is nearly linear and the emitter component of J_{01} can be estimated from

$$J_{0E} = \frac{qn_{iE}^2}{N_A} \times \frac{S_F + \dfrac{D_n W_E}{L_n^2}}{1 + \dfrac{S_F}{D_n/W_E}}, \quad (2)$$

where S_F is the front surface recombination velocity.

When the emitter surface is passivated by an $Al_{0.9}Ga_{0.1}As$ heteroface, S_F should be low and (2) reduces to

$$J_{0E} = \frac{qn_{iE}^2 W_E}{N_A \tau_n}. \quad (3)$$

If the heteroface layer were removed, S_F would be high and (2) would reduce to

$$J_{0E} = \frac{q n_{iE}^2 D_n}{N_A W_E} . \tag{4}$$

Equation (4), which shows that the emitter current varies as one over the emitter thickness when the emitter surface is unpassivated, is the basis of the etch experiment to be described in the following section.

The current due to hole injection into the n-type base can be evaluated from

$$J_{0B} = \frac{q n_{iB}^2}{N_D} \frac{D_p}{L_p'} , \tag{5}$$

where L_p', an effective diffusion length for holes, depends on the actual diffusion length, the thickness of the base, and on the back-surface recombination velocity.

II. EXPERIMENTAL RESULTS

For a meaningful analysis of the measured dark current, the cell's structural parameters (e.g. doping densities and layer thicknesses) must be accurately known. The cell structure with targeted film thicknesses and estimated doping densities is displayed in Fig. 1. The p-type emitter doping density was deduced by measuring the resistance of a test resistor adjacent to each cell and was confirmed by C-V profiling using an aluminum Schottky barrier deposited directly on the p-type emitter. The n-type base doping was also found by C-V profiling. The targeted thickness of the p-type emitter was confirmed during the etch experiment described below. A continuous $Al_{0.9}Ga_{0.1}As$ heteroface passivated the cell's front surface. Au/Zn ohmic contacts covered approximately 6% of the surface; the antireflection coating was Ta_2O_5. The cell area was 0.25 cm².

The forward-biased current-voltage characteristic was measured for seven different cells using four-point probe techniques and a Hewlett-Packard 4145A parameter analyzer with a temperature-controlled stage. A typical result, shown in Fig. 2, displays an $n=2$ characteristic at low biases and a fall-off at high biases due to the diode's series resistance. By curve-fitting in the region where $1<n<2$, which occurs before series resistance becomes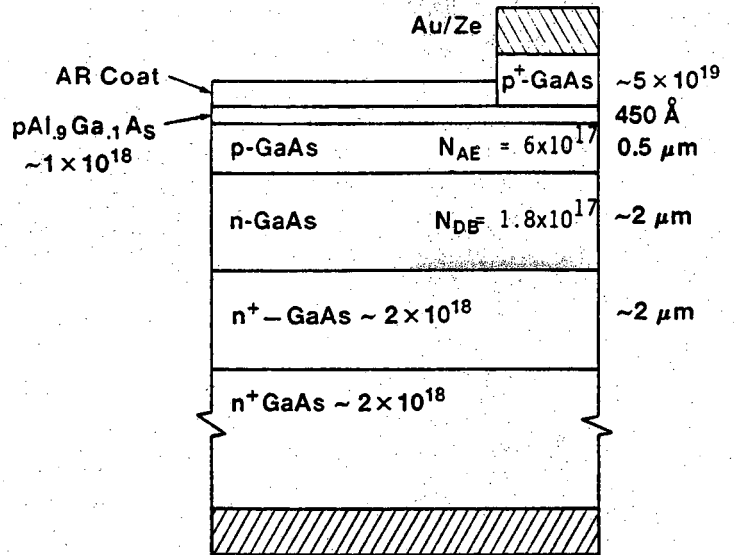 important, the saturation current density for the $n=1$ component of the current was extracted. The $n=1$ saturation current density, J_{01}, was verified by comparing it with that deduced from the cell's measured open-circuit voltage, which does not suffer from the series resistance limitation. The measured results and extracted saturation current densities are summarized in Table 1. The results show relatively little variation from cell to cell; note also that the $n=1$ saturation current density deduced by curve-fitting the dark I-V characteristic agrees well with that deduced from the open-circuit voltage.

To explore electron transport in the p-type emitter, an etch experiment was conducted to quantify the behavior of the emitter component of J_{01} as successive etches into the emitter layer were performed. Measurements of J_{01} at a temperature of 28.2 °C were taken after each etch. Before etching, J_{01} was $0.9 \times 10^{-18} A/cm^2$. The cell's antireflection coating was then removed by etching in hydrofluoric acid. An increase in the $n=1$ current occurred following this etch, which suggests that a part of the $Al_{0.9}Ga_{0.1}As$ window-layer was also removed. A solution of $H_2SO_4{:}H_2O_2{:}H_2O (2{:}1{:}96)$ was then used to etch the p-GaAs emitter everywhere except beneath the contacts. For the case of a high-recombination surface and negligible bulk-emitter recombination,

Fig. 1   Structure of the P/N heteroface cells showing targeted layer thicknesses and estimated carrier densities.

$$J_{OE} = \frac{q n_{iE}^2 D_n}{N_A(W_{E0} - Rt)} , \qquad (6)$$

where R is the etch rate and t the time the emitter was etched. According to (6), a plot of the measured $1/J_{01}$ versus t should be linear if J_{01} is dominated by J_{OE}; Fig. 3 shows that the measured current varies as expected. The experimental data, which lie on a straight line, suggest that J_{01} was described by (6). (The vertical axis of this plot is one over the measured saturation current density *minus* the saturation current measured before the experiment was begun.) The time required to etch through the emitter indicated that W_{E0} was very near the targeted value of $0.5\,\mu m$ (R was measured to be 20 Å/sec).
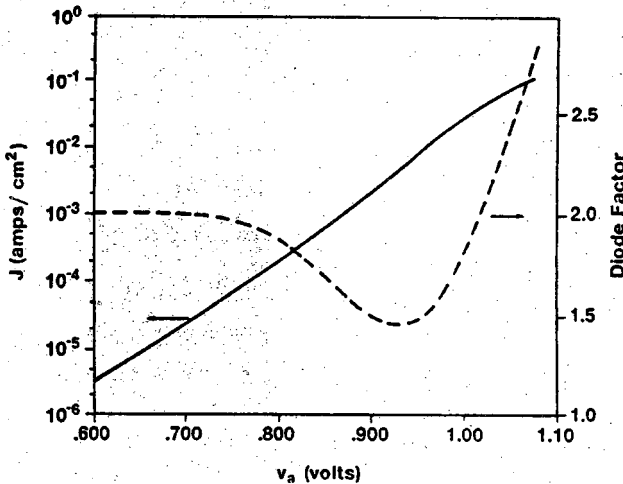

Fig. 2   Dark current versus voltage characteristic for cell 22 at 28° C.

III. ANALYSIS and INTERPRETATION

We now analyze and interpret the results with the objective being to relate the measured dark current to the cell's material parameters, dimensions and doping densities. The n=2 component, which comprises about half of the one-sun dark current is considered first then the n=1 component which dominates under even modest concentration. The n=2 saturation current density associated with recombination in the space-charge region can be written as

$$J_{02} = \frac{q n_i W_{eff}}{\tau_{SCR}} , \qquad (7a)$$

where

$$\tau_{SCR} = \sqrt{\tau_n \tau_p} , \qquad (7b)$$

$$W_{eff} = \frac{\pi}{2} \frac{k_B T/q}{\mathscr{E}_p} , \qquad (7c)$$

and $\mathscr{E}_p$ is the electric field where the recombination is at its maximum. There is also an n=2 current component associated with recombination in space-charge regions at the cell's perimeter, but for these relatively large area cells, perimeter currents are unimportant. Assuming that the traps are near midgap, the lifetime, τ_{SCR} can be deduced by comparing (7a) with J_{02} extracted from the measured data. The resulting lifetimes, also displayed in Table 1, are reasonable for device-quality GaAs. The DLTS spectra for this wafer showed a single peak at an energy near midgap. The activation energy (E≃0.67eV) and electron capture cross-section $\sigma \simeq 1.0\times10^{-15}cm^2$ do not correspond with the tabulated properties of intrinsic defects. The fact that it appears to be due to an impurity, not to an intrinsic defect, suggests that solar cell performance could be improved by reducing the source of this defect.
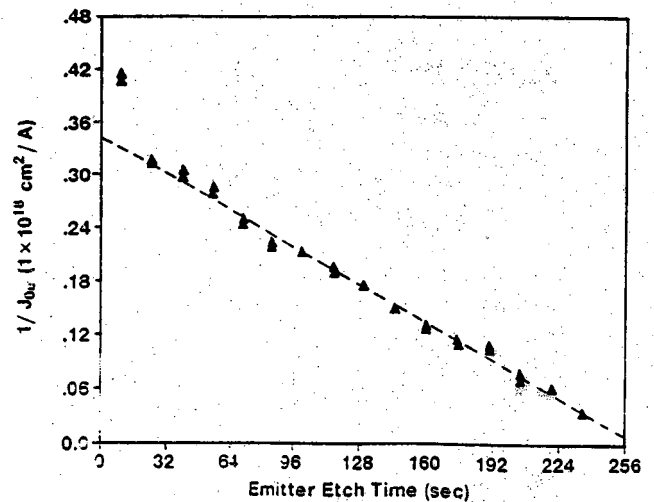

Fig. 3 $1/J_{0r}$ versus emitter etch time.

While the $n=2$ component of the cell's current can be readily understood in terms of the relatively low trap concentrations in these high-quality MOCVD films, the cell's $n=1$ component may control its performance. Using the average parameters in Table 1, we find that near the open-circuit voltage at one AM1.5 sun ($\simeq 0.98$ volts) the $n=1$ current is about equal to the $n=2$ current. It is important to understand the origin of the diffusion current and its relation to the cell's material quality and physical structure. An expected J_{01} can be computed from the cell's material and device parameters. Because the recombination velocity of the AlGaAs window layer to GaAs emitter interface is thought to be low, the cell's emitter current component should be given by (2) in which n_{iE} is the intrinsic carrier concentration for GaAs ($2.65\times10^6 \mathrm{cm}^{-3}$ at $28\,^\circ$C [2]) corrected for 13.5×10^{-3} eV of bandgap shrinkage [3]. For the more lightly doped base, we assume negligible bandgap narrowing and compute the base component of J_{01} from (5) taking $L_p{}'$ to be the hole diffusion length. Using the measured doping densities, taking D_p from majority carrier values quoted by Sze [5], and estimating τ_n and τ_p by τ_{SCR} given in Table 1

(these lifetimes are comparable to those routinely reported for high-quality GaAs cells), we find that $J_{01} = J_{0E} + J_{0B} = 0.04\times10^{-18} + 0.24\times10^{-18}$ A/cm^2. This estimate is about three times less than the observed J_{01}.

To increase cell efficiency by dark current reduction, the source of the observed diffusion current must be identified. Consider first the possibility that the observed J_{01} is due to recombination in the emitter. If we equate (2) to the measured J_{01}, we find that a lifetime of 0.2 nanosecond is required to account for the observed dark current. This lifetime estimate is far below the space-charge region lifetimes quoted in Table 1 and is 5 to 10 times less than the minority carrier lifetime typically found in device-quality GaAs. An alternative hypothesis to account for the observed J_{01} is recombination at the AlGaAs/GaAs interface. Using (3) and assuming $D_n = 75$ cm^2/v–sec [4], we estimate that $S_F \simeq 6\times10^5$cm/sec. This estimated S_F is near the value expected for a bare GaAs surface so little change in dark current should be observed when the heteroface is removed by etching. This prediction contrasts with the factor of 3.5 increase in J_{01} that was observed when the heteroface was removed by etching.

Our analysis of the emitter current component may be clouded by uncertainties in the minority carrier parameters, n_{iE} and D_n. The $D_n n_{iE}{}^2$ product can be estimated from the slope of J_{01} versus emitter thickness as displayed in Fig. 3. If we describe the slope of this line by (6), then a value of $D_n n_{iE}{}^2 = 6\times10^{14}$ cm^{-4}sec^{-1}. Using an intrinsic carrier density from Blakemore [2], corrected for bandgap shrinkage in p-GaAs according to Casey and Panish [3], and the theoretical minority carrier mobility of Walukiewicz et al. [4], we deduce $D_n n_{iE}{}^2 = 9\times10^{14}$. The reasonable agreement between theory and experiment suggests that there are no major uncertainties in the minority carrier transport parameters of p-GaAs in this doping range.

Next, we make use of (5) to consider the component of J_{01} due to hole injection into the n-base. Equating (5) to the observed J_{01}, and assuming $D_p = 5.7$cm^2/v–sec [5], we find the $L_p{}' \simeq 0.5$ micrometers. This effective length is somewhat shorter than the expected minority carrier diffusion length ($1-2\mu$m), but hole injection does appear to be a significant component of the diffusion current. The minority carrier hole diffusion coefficient in silicon has been recently measured to be 2 times the majority carrier value [6]. Similar effects, if operative in GaAs, would increase our estimate of the dark current. For these particular cells, the discrepancy between the measured and expected diffusion currents may be due to the light emitter doping coupled with a low emitter lifetime.

IV. CONCLUSIONS

The dark I-V characteristics of high-quality p/n heteroface cells were measured and analyzed. The cell's diffusion current was shown to be an important component of the dark current, even for one-sun operation. For conventionally designed cells, the dark current is expected to be dominated by hole injection into the n-bulk. Measurements of cells with relatively lightly doped emitters suggest that the electron lifetime in the emitter may be low. If hole injection into the bulk can be suppressed, and if routinely reported lifetimes are maintained, the dark currents observed in this study can be reduced by more than a factor of 10. Considerable progress in the already high efficiencies of p/n heteroface cells can still be achieved.

REFERENCES

[1]   H.C. Hamaker, C.W. Ford, J.G. Werthen, G.F. Virshup, and N.R. Kaminar, *Appl. Phys. Lett.,* Vol. 47, p. 762, 1985.

[2]   J.S. Blakemore, *J. Appl. Phys.,* Vol. 53, p. R123, 1982.

[3]   H.C. Casey and M.B. Panish, *Heterostructure Lasers,* New York, Academic Press, 1978.

[4]   W. Walukiewicz, J. Lagowski, L. Jastrzebski, and H.C. Gatos, *J. Appl. Phys.,* Vol. 50, pp.5040-5042, 1979.

[5]   S.M. Sze, *Physics of Semiconductor Devices, 2nd Ed.,* John Wiley and Sons, New York, 1981.

[6]   S.E. Swirhum, J.A. del Alamo, and R.M. Swanson, *IEEE Electron Dev. Lett.,* Vol. EDL-7, pp. 168-171, 1986.

Cell ID	Temp °C	J_{02} A/cm^2	J_{01} A/cm^2	J_{01} (from V_{oc})	τ_{SCR} nsec
2	28	0.9×10^{-10}	0.3×10^{-18}	0.7×10^{-18}	2.0
15	28	0.5×10^{-10}	0.6×10^{-18}	0.5×10^{-18}	3.8
19	28	0.5×10^{-10}	0.8×10^{-18}	0.9×10^{-18}	3.6
20	28	1.0×10^{-10}	0.2×10^{-18}	0.4×10^{-18}	1.9
21	28	0.4×10^{-10}	0.9×10^{-18}	0.8×10^{-18}	5.4
22	28	0.3×10^{-10}	0.9×10^{-18}	0.9×10^{-18}	5.5
23	28	0.4×10^{-10}	1.5×10^{-18}	1.3×10^{-18}	4.9
average	28	0.6×10^{-10}	0.7×10^{-18}	0.8×10^{-18}	3.9
std. dev.	-	0.3×10^{-10}	0.4×10^{-18}	0.3×10^{-18}	1.4

Table 1 Results of dark I-V measurements and analysis.

EXPERIMENTAL CHARACTERIZATION OF MINORITY CARRIER MIRRORS FOR GALLIUM ARSENIDE-BASED SOLAR CELLS

M. E. Klausmeier-Brown, C. S. Kyono, D. P. Rancour, M. S. Carpenter,

M. R. Melloch, M. S. Lundstrom, R. F. Pierret

School of Electrical Engineering, Purdue University

West Lafayette, Indiana 47907

ABSTRACT

The results of a systematic experimental study of minority carrier mirrors for GaAs-based solar cells are reported. The experiments utilized n^+/p GaAs diodes fabricated on films grown by molecular beam epitaxy (MBE). Cells were fabricated (i) with the p-type base layer grown directly on the p^+ substrate, (ii) with the base layer grown on a p^+ buffer layer, and (iii) with the base layer grown on a p^+ AlGaAs buffer layer. The dark current-voltage characteristics were analyzed to compare the ability of various minority carrier mirrors to suppress dark current. Results showed that these buffer layers were ineffective as minority carrier mirrors. Also used was a new technique employing illumination and etching which allowed a comparison of the minority carrier reflecting properties of two different barriers incorporated into a single solar cell. It was found that heterojunction barriers can be effective if the interface quality is high. In addition, solar cells with AlGaAs buffer layers appeared to reduce trap concentrations and n=2 dark currents.

I. INTRODUCTION

Isotype doping barriers, or back-surface-fields (BSF's), are commonly used to confine minority carriers in silicon solar cells, thereby increasing both open-circuit voltage and short circuit current [1,2]. By analyzing the dark current versus voltage characteristics of cells, an effective, low injection recombination velocity for nn^+ silicon barriers of ≈ 10 cm/sec has been deduced [3]. For pp^+ silicon barriers, effective recombination velocities of about 100 cm/sec have been reported recently by Girisch and coworkers [4]. They demonstrated that the effective barrier recombination velocity can be quantitatively related to the physical structure of the low-high junction when effects such as bandgap narrowing, majority carrier degeneracy, and Auger recombination are taken into account. Low-high barriers are also a standard feature of GaAs solar cell design [5], but quantitative studies of such barriers in GaAs cells have not been reported. An experiment reported by Gale and coworkers demonstrated that when a pp^+ homojunction barrier is replaced by a heterojunction barrier, substantial reduction of dark current occurs [6]. This result suggests that pp^+ barriers in GaAs are ineffective in confining minority carriers, in direct contradiction with simple estimates of the effective recombination velocity [7]. It indicates that substantial uncertainties in our understanding of

the minority carrier transport properties of p^+ GaAs exist.

The purpose of this paper is to describe results of experiments conducted to estimate S_{LH}, the effective recombination velocity for p GaAs/p^+ GaAs and p GaAs/p^+ AlGaAs barriers. Section II describes the devices fabricated, and Sec. III the simple theory used to interpret the experimental results. In Sec. IV, the results of dark current-voltage characterization of several different diodes, with and without low-high junctions, are reported. The results are shown to imply barrier recombination velocities of $\approx 6 \times 10^5$ cm/sec for homojunction BSF's. These results exceed those predicted by a simple theoretical analysis [7] and are close to the kinetic limit. Results for a structure incorporating an AlGaAs buffer layer as a BSF indicate recombination velocities which are a factor of three lower than those in the homojunction BSF structures. The solar cells grown with this configuration may have had impurities or defects at the upper GaAs/AlGaAs interface which increased recombination at the barrier, reducing its effectiveness as a minority carrier mirror. The AlGaAs buffer layer had the beneficial effect, however, of improving overall film quality by reducing the concentration of recombination centers in the space-charge (or depletion) region of the solar cells. Investigations of the MBE film quality by Deep Level Transient Spectroscopy (DLTS) have shown that deep level trap concentrations are greatly reduced when an AlGaAs buffer layer is used. While the GaAs/AlGaAs interface quality problem mentioned above may be unique to MBE-grown films, it is possible that incorporation of AlGaAs buffer layers would improve the quality of films grown using other technologies, such as MOCVD (Metal-Organic Chemical Vapor Deposition) or LPE (Liquid Phase Epitaxy), by reducing the concentration of deep levels.

Also described in Sec. IV is an experiment with an "inverted" structure having both p^+ GaAs and p^+ AlGaAs layers on top of the film, instead of on the substrate. In this experiment the top layers of the cell were etched away gradually by a series of short etches, and the short circuit current I_{SC} was measured under constant illumination after each etch. This technique yielded a lower limit estimate for the effective recombination velocity of the p GaAs/p^+ GaAs barrier of $\approx 5 \times 10^5$ cm/sec, confirming the results of our dark current-voltage measurements. In this inverted configuration the p^+ AlGaAs layer proved to be a better effective minority carrier mirror.

II. DEVICE FABRICATION

A Perkin-Elmer Model 400 MBE system was used to grow all the films for these experiments. Standard GaAs substrate preparation and film growth procedures were followed [8,9]. The substrates used were cleaved from (100) GaAs wafers grown by the horizontal Bridgman method. The first five films were grown in two groups. Films F1-F3 were grown on consecutive days on substrates cleaved from the same wafer. Films F4 and F5 were grown on consecutive days three weeks later on substrates cleaved from another wafer.

The structure of the diodes is shown in Fig. 1. Note that in Fig. 1 and elsewhere, use of the superscript "+" on a quantity or variable associates that quantity with the buffer layer, except in the case of p^+ and n^+. Table 1 lists the characteristics of each film. Note that for the first film, F1, the p-type base was grown directly on the p^+ substrate, with no intervening buffer layer. For films F2-F4, a p^+ GaAs buffer layer was first grown on the substrate to serve as a minority carrier mirror, or BSF. In film F5 the buffer layer is p^+ $Al_{0.2}Ga_{0.8}As$. Layer thicknesses were estimated from MBE growth rates. The base doping densities were determined by capacitance-voltage profiling. Buffer layer doping densities were estimated to be greater than 5.0×10^{18} cm^{-3}, and the substrates were doped to approximately 1×10^{19} cm^{-3}.

Fabrication of diodes on the films was done in parallel for each of the two groups. The front contact metalization was patterned by a lift-off technique. Diode and resistor test patterns were isolated by mesa-etching. The front contacts were alloyed Au:Ge. Indium served as the contact to the substrate.

III. MEASUREMENT AND ANALYSIS

Several theoretical treatments of the current-voltage characteristics of back-surface-diodes have been reported [3,7,10]. We outline in this section a very simple treatment of the problem which is expected to be valid for the devices described above. The theory will apply only when the base is thin with respect to the minority carrier diffusion length in the base, L_n:

$$L_n \gg W_B ,\qquad (1a)$$

or equivalently,

$$\tau_n \gg \frac{W_B^2}{D_n} ,\qquad (1b)$$

where D_n is the diffusion coefficient and τ_n is the recombination lifetime for electrons in the base. The back-surface-field cannot significantly affect the current-voltage characteristic of the cell unless condition (1) is met. For the diodes under investigation, the base doping was chosen low with respect to the emitter doping in order to: (i) maintain long diffusion lengths so that condition (1) was achieved, (ii) enhance the n=1 component of the current, and (iii) to suppress hole injection into the emitter.

For these conditions, the n=1 component of the diode current is determined by electron injection into the base. It can be shown that the n=1 current component due to electrons injected into the base is:

Table 1.
Layer thicknesses and doping densities for films F1-F5. W_B' is the base width as fabricated.

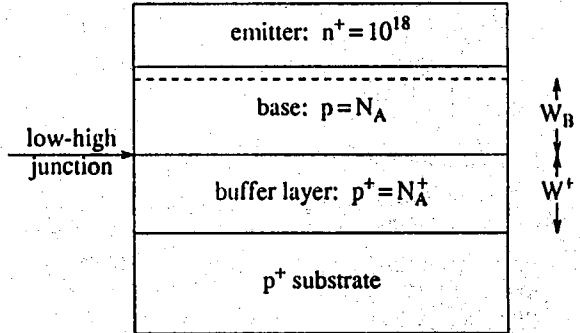| Film ID	Buffer Layer	W_B' μm	W^+ μm	N_A cm^{-3}
F1	none	1.35	0.00	4.4×10^{16}
F2	p^+ GaAs	0.88	0.44	3.7×10^{16}
F3	p^+ GaAs	0.90	0.90	4.0×10^{16}
F4	p^+ GaAs	0.62	0.69	3.0×10^{16}
F5	p^+ $Al_{0.2}Ga_{0.8}As$	0.62	0.69	3.0×10^{16}

Figure 1.
GaAs diode structure and labeling conventions. The dashed line indicates the extent of the depletion region into the base.

$$J_1 = J_{01} \left[e^{\frac{qV_A}{k_B T}} - 1 \right] ,\qquad (2a)$$

where the n=1 saturation current density J_{01} is

$$J_{01} = \frac{qn_i^2}{N_A} \left[\frac{S_{LH} + \frac{D_N}{L_N} \tanh\left(\frac{W_B}{L_N}\right)}{1 + \frac{S_{LH} \tanh\left(\frac{W_B}{L_N}\right)}{D_N/L_N}} \right] .\qquad (2b)$$

Assuming J_{01} is entirely due to electron diffusion into the base and that condition (1a) holds, equation (2b) can be rearranged to find S_{LH}, the effective minority carrier recombination velocity at the base-buffer layer interface (or low-high junction):

$$S_{LH} = \frac{1 - \frac{qn_i^2}{N_A J_{01}} \cdot \frac{W_B}{\tau_n}}{\frac{qn_i^2}{N_A J_{01}} - \frac{W_B}{D_N}} .\qquad (3)$$

The n=2 current component can be expressed in the same form as (2a), where the saturation current density J_{02} is:

$$J_{02} = \frac{qn_i}{\tau_{SCR}} W_{eff}, \quad (4)$$

the effective lifetime in the space-charge region (SCR) is $\tau_{SCR} = (\tau_n \tau_p)^{1/2}$, and the effective recombination width W_{eff} depends on the applied voltage, the doping of the p-type active region, and the width of the space charge region about the n^+/p junction [11,12]. The derivation of (4) assumes a single dominant R-G center in the SCR and that $\tau_n \approx \tau_p$.

The procedure used to analyze the measured current-voltage characteristic of n^+/p GaAs diodes used the above-described theory as follows. First, the dark current-voltage characteristics of several diodes from each wafer were measured. Saturation current densities for both the n=2 and n=1 current components were extracted from the measured data by curve fitting. The minimum voltage for curve fitting n=1 and n=2 components to the measured data was chosen so that n≤2. The maximum voltage was chosen so that the series resistance drop was negligible. Next, the J_{02} value derived from curve fitting was used in (4) to obtain τ_{SCR}. Using τ_{SCR} to approximate τ_n, we then checked to be sure that condition (1) was well satisfied. If condition (1) was satisfied, we could then estimate S_{LH} from (3).

IV. RESULTS AND DISCUSSION

This section will describe the results of experiments carried out so far on n^+/p GaAs diodes, both with and without BSF buffer layers. In Sec. IV.A we discuss the dark-current characterization of diodes in terms of the effective barrier recombination velocity S_{LH}. The results of DLTS characterization of the films are shown in Sec. IV.B. Illuminated short circuit current measurements on the inverted (barriers on top) structure are discussed in Sec. IV.C.

The extracted n=1 saturation current density component, J_{01}, showed little variation either from diode-to-diode on a wafer, or from wafer-to-wafer. Using τ_{SCR} from (4) to approximate τ_n, it was found that condition (1) was well satisfied for all diodes tested. The values of τ_{SCR} were in the

range of 1-4 nsec. This estimate of τ_n is consistent with estimates based on the measured short-circuit current of solar cells fabricated in our laboratory. The minority carrier electron diffusion coefficient in the p-type base was taken to be 135 cm²/sec from the theoretical calculations of Walukiewicz [13] (see also [14]). These parameters were used in (3) to calculate S_{LH} for each film. The results are presented in Table 2. We found that because the extracted J_{01} and S_{LH} values were rather large, the value of τ_n used in (3) did not strongly affect the resultant S_{LH}.

A. Effective Barrier Recombination Velocities

The effective barrier recombination velocities extracted from (3) are surprisingly high. An upper limit for S_{LH} may be deduced from the thermionic emission velocity [15],

$$S_{LH} \leq \left[\frac{k_B T}{2\pi m^*}\right]^{1/2}. \quad (5)$$

For GaAs at room temperature, we find $S_{LH} \leq 1.0 \times 10^7$ cm/sec. The barrier recombination velocities deduced experimentally for films without an AlGaAs BSF (F1-F4) are within approximately one order-of-magnitude of this limit. While none of the solar cells with BSF layers performed as well as expected, the measured values of S_{LH} do show the expected trend. Solar cells fabricated on film F1, grown directly on a p⁺ substrate, had the largest values of S_{LH}. Films F2-F4, with homojunction BSF's, resulted in S_{LH} values a factor of three lower. S_{LH} values were lowest for the heterojunction BSF film, F5: ten times lower than for film F1.

A simple expression relating S_{LH} to the structural parameters of the barrier, valid for both homojunction and heterojunction barriers, has been given by DeMoulin and coworkers [7] as

$$S_{LH} = \frac{D_n N_A}{L_n' N_A'} \left[\frac{n_i^+}{n_i}\right]^2 \frac{\mathcal{J}_{1/2}(\eta_V^+)}{e^{\eta_V^+}} \coth\left[\frac{W_B}{L_n^+}\right], \quad (6)$$

where $\eta_V^+ = (E_V^+ - E_F^+)/k_B T$ and $\mathcal{J}_{1/2}(\eta_V^+)$ is the Fermi-Dirac integral of order one-half. The expression accounts for majority carrier degeneracy in the heavily doped buffer layer and bandgap shrinkage effects, but does not consider any interface

Table 2.
Average extracted saturation current densities
and barrier recombination velocities.
Measurements were made at 300K.

Film ID	Buffer Layer	J_{02} A/cm²	J_{01} A/cm²	S_{LH} cm/sec
F1	none	3.8×10^{-10}	1.6×10^{-17}	2.2×10^6
F2	p⁺ GaAs	3.0×10^{-10}	1.4×10^{-17}	6.9×10^5
F3	p⁺ GaAs	3.7×10^{-10}	1.1×10^{-17}	5.4×10^5
F4	p⁺ GaAs	$19. \times 10^{-10}$	1.8×10^{-17}	6.6×10^5
F5	p⁺ Al$_{0.2}$Ga$_{0.8}$As	3.8×10^{-10}	0.8×10^{-17}	2.3×10^5

states which may be present. An estimate for S_{LH} can be made using (6) assuming that the buffer layer is short compared to a diffusion length and that the buffer layer-substrate interface acts as an infinite recombination plane. Under such conditions, using (6) and bandgap shrinkage data from Casey and Panish [16], we estimate $S_{LH} \approx 10^4$ cm/sec for the pp$^+$ homo-junction barriers in films F2-F4. This theoretical estimate is roughly 50 times less than the value deduced from analysis of the experimental data. Some of the parameters used in making this estimate from (6), are fairly uncertain. For example, we did not measure the doping (N_A^-) in the buffer layer, but estimated its value from MBE growth rates. In addition, a small change in the expression for bandgap shrinkage from [16] would cause a large change in the estimated S_{LH} value.

Applying (6) to the AlGaAs BSF used in film F5 we expect $S_{LH} \approx 1$ cm/sec. This estimate does not account for interface states. It appears that impurities or defects near the upper GaAs/AlGaAs interface serve to increase recombination (and thus S_{LH}) at the heterojunction barrier. It should be emphasized that this is probably an MBE-specific problem. The existence of a high impurity concentration at this interface is consistent with the findings of McAfee and coworkers [17], who observed a spatial profile of deep levels which was highly peaked in a 140 Å region at the GaAs/AlGaAs interface in MBE double heterostructure lasers. If impurities coming from the substrate were the source of these interface states in our MBE-grown material, then incorporation of an AlGaAs/GaAs superlattice into the AlGaAs buffer layer of MBE-grown solar cells might lower the recombination velocity for the heterojunction barrier by trapping the impurities. MBE-grown structures which include an AlGaAs minority carrier mirror near the top surface, such as the normal "heteroface" solar cell design, would not necessarily show the same degradation in performance as was seen in film F5, for which the mirror was grown on the substrate. Capacitance-voltage measurements of MBE structures by Tan and coworkers [18] showed that when an AlGaAs layer is incorporated into the GaAs crystal, the interface nearer the substrate (bottom) is cleaner than the top interface. Thus by simply inverting the structure of film F5 (placing the AlGaAs BSF layer on top), better n=1 current suppression is expected.
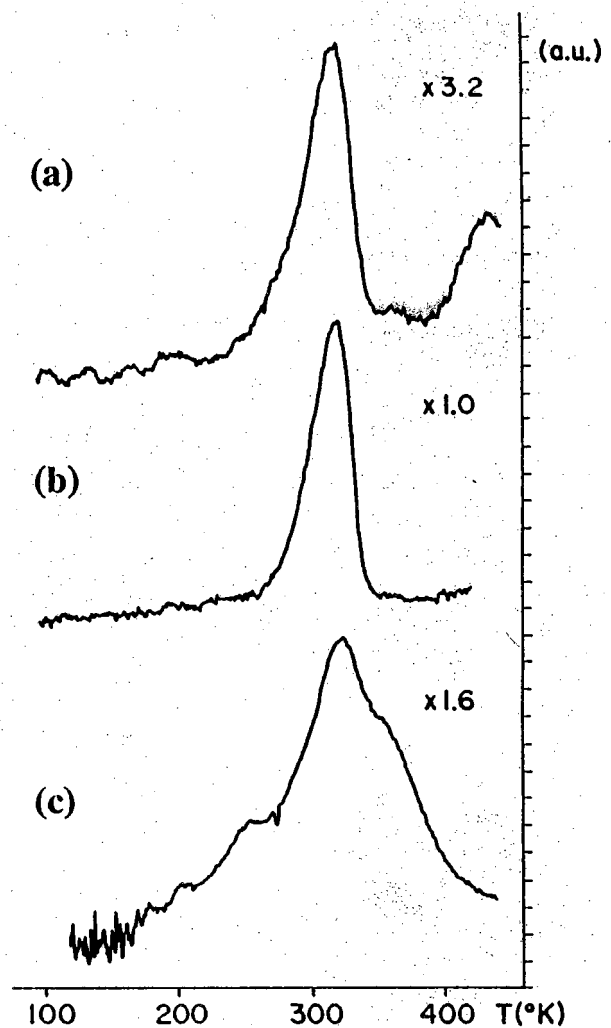
B. Discussion of DLTS Studies

While the existence of defects or impurities at the hetero-interface in film F5 seems to degrade the performance of the minority carrier mirror, the AlGaAs buffer layer still appears to have a beneficial effect. In general, the cleanest films (in terms of impurity and trap density) are grown in the MBE after many films have been grown without opening the growth chamber. Between the growth of the first three films (F1-F3) and the growth of the last two films (F4 and F5) the MBE growth chamber was opened for repairs. Because more growth time had been accumulated in the case of films F1-F3, we expected diodes fabricated on films F4 and F5 to show much higher J_{02} values due to higher impurity concentrations in the space-charge-region of the diodes. However, Table 2 shows that J_{02} for film F5 was about the same as for films F1-F3, while J_{02} for film F4 was much higher. We attribute this to the gettering or trapping of impurities in film F5 at the GaAs/AlGaAs interface. The DLTS studies discussed were undertaken to confirm this interpretation of the results.

Figure 2.
Typical DLTS spectra for
(a) films F1-F3, (b) film F5, and (c) film F4.
The DLTS emission rate window was 200 sec^{-1}.
The diodes were pulsed from 1.0V reverse bias to 0.0V with 1 msec fill pulses.

A study of deep levels in each of the five films was done using DLTS. There seems to be a correlation between the DLTS data in Fig. 2, and the space-charge-recombination saturation currents (J_{02}) listed in Table 2. Fig. 2 shows that the main peaks for films F1-F3 and F5 are very similar, as are the values of J_{02} for those films. On the other hand, the main peak in the DLTS spectrum for film F4 is broadened by several sub-peaks. The main peak in each plot in Fig. 2 is located at 320K, with a thermal activation energy of $E_T - E_V = 0.55$eV, and a capture cross section for holes of $\sigma_p = 6.8 \times 10^{-16}$ cm^2. Possible identities of the trap include iron [19,20], a Gallium vacancy [21], or a vacancy complex.

C. Illuminated Measurements of the Inverted Structure

To take advantage of the superior quality of the bottom interface of AlGaAs layers in MBE-grown GaAs crystals (as discussed in Sec. IV.A), the structure shown in Fig. 3 was grown. It is similar to film F5, but is inverted with respect to film F5, and incorporates an additional p$^+$GaAs minority carrier mirror. The 0.2 µm p$^+$GaAs cap layer was contacted with non-alloyed Au:Zn. Indium was again used as the back contact. A large n=2 dark current component in this film obscured the presence of an n=1 component. However, it was still possible to judge the quality of the minority carrier mirrors by measuring the short circuit current I$_{SC}$ under illumination. We devised the following experiment. First, the metal pattern was covered by photoresist. Then I$_{SC}$ was measured under illumination of approximately 1 sun by a General Electric ELH lamp. Next, ≈ 0.025 µm of material was etched off, and I$_{SC}$ was measured again. This process of etching followed by measurement of I$_{SC}$ was repeated until the active p GaAs layer was exposed. A fresh etchant solution ($2H_2SO_4 : 1 H_2O_2 : 96 H_2O$) was prepared for each etch. Etch depth and uniformity was checked several times during the experiment by step profiling.

The experiment was modeled using the Purdue University one-dimensional non-equilibrium heterostructure simulation program PUPHS [22]. Fig. 4a shows the results of this simulation. Short circuit current I$_{SC}$ rises initially as the cap layer is etched off and more photons pass through the AlGaAs layer, generating electron-hole pairs where they can be collected. There is a slope change when the AlGaAs layer is exposed, due to the different absorption coefficients of AlGaAs and GaAs. As soon as the AlGaAs layer is completely removed, I$_{SC}$ plummets because electrons generated in the 0.15 µm p$^+$GaAs barrier layer can recombine at the surface. I$_{SC}$ again rises as the p$^+$GaAs barrier is etched away, and falls when the p GaAs active layer is exposed. Finally, I$_{SC}$

rises as the active region is thinned and electrons are generated nearer the p/n$^+$ junction. The vertical scale factor is somewhat arbitrary in Fig. 4a due to uncertainty of the lamp's spectrum.

Results of the actual experiment are shown in Fig. 4b. The experiment generally follows the simulation, with an important exception: I$_{SC}$ rises very little as the p$^+$GaAs barrier layer is removed, in contrast to the anticipated shape of the curve. This demonstrates that the p$^+$AlGaAs layer is effective as a minority carrier mirror, while the p$^+$GaAs layer is a poor mirror. The magnitude of the sharp drop in I$_{SC}$ that is observed when the p$^+$GaAs barrier is exposed can be used to estimate the effective recombination velocity S$_{LH}$ for the p$^+$GaAs barrier. The result is S$_{LH} \geq 5 \times 10^5$ cm/sec, in agreement with dark current-voltage measurements of S$_{LH}$ for p GaAs/p$^+$GaAs BSF's in films F2-F4.

(a)

Figure 3.
Film profile for etching experiment.

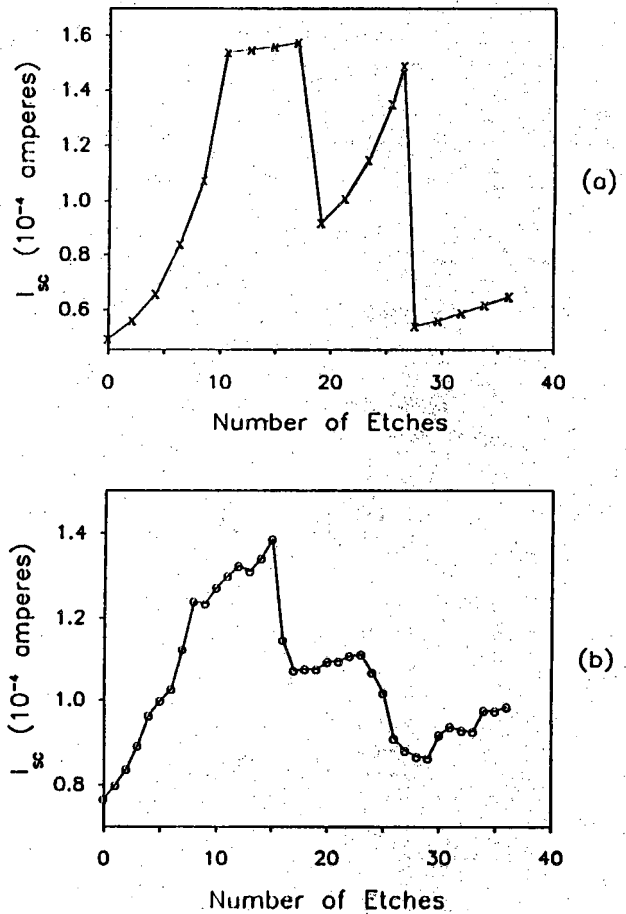| p$^+$GaAs	0.20 µm
p$^+$(AlGa)As	0.15 µm
p$^+$GaAs	0.15 µm
p GaAs	0.75 µm
n$^+$GaAs	0.75 µm
n$^+$ substrate	

(b)

Figure 4.
I$_{SC}$ versus number of etches.
(a) PUPHS Simulation; (b) Experiment

V. CONCLUSIONS

Experiments with MBE-grown n^+/p GaAs diodes demonstrated that p GaAs/p^+ GaAs homojunction barriers were ineffective at confining minority carriers. Such barriers have effective recombination velocities of $\approx 6 \times 10^5$ cm/sec, which is near the kinetic limit. Theoretical estimates of S_{LH}, which make use of conventionally accepted minority carrier parameters for p-type GaAs, are a factor of 50 less than the experimentally deduced S_{LH} values. Heterojunction back-surface-fields can be effective minority carrier mirrors if the p GaAs/p^+ AlGaAs interface quality is high. The results demonstrate the requirement for heterojunction BSF's in GaAs cells containing a p-type base and emphasize the need for improved characterization of minority carrier properties of p^+GaAs. Finally it was shown by DLTS studies and measurements of the SCR recombination current, J_{02}, that the presence of an AlGaAs buffer layer grown on the GaAs substrate reduces dark-current by gettering and/or trapping impurities.

REFERENCES

[1] J. Mandelkorn, J.H. Lamneck Jr., and L.R. Scudder, in Conf. Rec. 9th Photovoltaic Specialists Conference, 1972.

[2] J.G. Fossum and E.L. Burgess, *Appl. Phys. Lett.*, Vol. 33, pp. 238-240, 1978.

[3] J.G. Fossum, R.D. Nasby, and S.C. Pao, *IEEE Trans. Electron Dev.*, Vol. ED-27, pp. 785-791, 1980.

[4] R. Girsch, R.P. Mertens, and R. Van Overstraeten, *Solid-State Electron.*, Vol. 29, pp. 776-676, 1986.

[5] H.C. Hamaker, C.W. Ford, J.G. Werthen, G.F. Virshup, and N.R. Kaminar, *Appl. Phys. Lett.*, Vol. 47, pp. 762-764, 1985.

[6] R.P. Gale, J.C.C. Fan, G.W. Turner, and R.L. Chapman, in Conf. Rec. 17th IEEE Photovoltaic Specialists Conference, p. 1422, 1984.

[7] P.D. DeMoulin, M.S. Lundstrom, and R.J. Schwartz, *Solar Cells*, Vol. 20, pp. 229-236.

[8] R.E. Noren, M.S.E.E. Thesis, Purdue University, School of Electrical Engineering, August, 1986.

[9] A.Y. Cho and J.R. Arthur, *Progress in Solid-State Chemistry*, Vol. 10, pp. 157-191, 1975.

[10] J.R. Hauser and P.M. Dunbar, *Solid-State Electron.*, Vol. 18, p. 715, 1975.

[11] C.-T. Sah, R.N. Noyce, and W. Schockley, *Proc. IRE*, Vol. 45, No. 9, pp. 1228-1243, 1957.

[12] A. van der Ziel, *Solid-State Electronics*, Prentice-Hall, Englewood-Cliffs, N.J., 1970.

[13] W. Walukiewicz, W. Lagowski, L. Jastrzebski, and H.C. Gatos, *J. Appl. Phys.*, Vol. 50, pp. 5040-5042, 1979.

[14] C.M. Maziar and M.S. Lundstrom, *Electron. Lett.*, Vol. 22, pp. 565-566, 1986.

[15] S.M. Sze, *Physics of Semiconductor Devices*, John Wiley and Sons, New York, p. 261, 1981.

[16] H.C. Casey and M.B. Panish, *Heterostructure Lasers*, Academic Press, New York, p. 157, 1978.

[17] S.R. McAfee, D.V. Lang, and W.T. Tsang, *Appl. Phys. Lett.*, Vol. 40, p. 520, 1982.

[18] K.L. Tan, M.S. Lundstrom, and M.R. Melloch, *Appl. Phys. Lett.*, Vol. 42, 1986.

[19] P.K. Battacharya, H.J. Buhlmann, and M. Ilegems, *J. Appl. Phys.*, Vol. 53, p. 6391, 1982.

[20] A. Mitonneau, G.M. Martin, and A. Mircea, *Electron. Lett.*, Vol. 13, p. 666, 1977.

[21] A. Fazzio, J.R. Leite, and M.L. De Siqueira, *J. Phys. C*, Vol. 12, p. 3469, 1979.

[22] M.S. Lundstrom and R.J. Schuelke, *IEEE Trans. Electron Dev.*, Vol. ED-30, pp. 1151-1159, 1983.

Recombination-current suppression in GaAs *p-n* junctions grown on AlGaAs buffer layers by molecular-beam epitaxy

D. P. Rancour, M. R. Melloch, R. F. Pierret, M. S. Lundstrom, M. E. Klausmeier-Brown, and C. S. Kyono

School of Electrical Engineering, Purdue University, West Lafayette, Indiana 47907

n^+pp^+ GaAs and n^+pP^+ GaAs/GaAs/Al$_{0.3}$Ga$_{0.7}$As mesa diodes have been fabricated from films grown by molecular-beam epitaxy. The diodes made from films employing an AlGaAs buffer layer show marked improvements (a factor of 5 reduction) in recombination current densities. Deep level transient spectroscopy measurements moreover indicate that deep level concentrations are reduced by the AlGaAs buffer.

Suppression of recombination currents is an important factor in the design of high-performance AlGaAs/GaAs solar cells and bipolar transistors.[1,2] Nonradiative recombination is typically controlled by deep levels introduced by impurities and/or defects in the semiconductor bulk and surfaces. In this communication we demonstrate that relatively thick GaAs films grown by molecular-beam epitaxy (MBE) atop a 0.69-μm Al$_{0.3}$Ga$_{0.7}$As buffer layer show a substantially lower deep level concentration than do films grown atop a GaAs buffer layer. *p-n* junctions fabricated in such films display a corresponding reduction in recombination current. Gale *et al.*[3] have previously employed AlGaAs buffer layers in the fabrication of GaAs solar cells by metalorganic chemical vapor deposition (MOCVD). These cells showed higher open-circuit voltages and conversion efficiencies than cells made with GaAs buffers. This improvement was attributed to the greater minority-carrier confinement achieved by the GaAs/AlGaAs potential barrier. Our work indicates that reduced recombination current, due to impurity reduction, may also have contributed to the improved solar-cell characteristics. Similar results have been obtained by Beneking *et al.*,[4,5] who observed reduced impurity concentrations for GaAs films grown by MOCVD and liquid-phase epitaxy on top of an indium-doped strained layer several micrometers thick. Our report of corresponding benefits for MBE-grown films using relatively thin AlGaAs layers suggests that the technique is suitable for the routine growth of high-quality MBE-grown AlGaAs/GaAs films for bipolar applications.

The MBE films used in this work were grown in a Perkin-Elmer 400 MBE system. The starting substrates were Zn-doped (1.5×10^{19} cm^{-3}) (100) horizontal Bridgeman material with an etch pit density of less than 500 cm^{-2}. The GaAs layers were grown at a substrate temperature of 605 °C and the AlGaAs layer at a substrate temperature 625 °C.

There were a total of five films grown for this work which we have labeled $F1$–$F5$. The first three samples, $F1$, $F2$, and $F3$, were grown on three consecutive days and the substrates were cleaved from the same wafer. There was a total of 28 μm of material grown in the MBE system prior to the growth of samples $F1$–$F3$. The first film, $F1$, had the Be-doped *p*-type base grown directly on the p^+ substrate. The second film, $F2$, had a 0.44-μm p^+ buffer layer below the *p*-type base while the third film, $F3$, had a 0.9μm p^+ buffer

layer. (Film structures $F1$–$F3$ are shown in Fig. 1.) Ohmic contacts were made to the n^+ emitters by alloying Au-Ge, and mesa diodes were defined by photolithography and subsequent wet etching in H$_2$SO$_4$:H$_2$O$_2$:H$_2$O (1:8:40). The areas of the diodes ranged from 4×10^{-4} cm^2 to 1.6×10^{-3} cm^2. The MBE system was opened to repair a broken weld on its Ga oven before growing the second set of films $F4$ and $F5$. Films $F4$ and $F5$ were grown on two consecutive days with substrates cleaved from a second wafer. There was a total of 12 μm of material grown in the MBE system prior to the growth of samples $F4$ and $F5$. (Because of the shorter burn in time of the ovens, one would suspect samples $F4$ and $F5$ to be of inferior quality when compared to samples $F1$ through $F3$.) The first sample grown, $F4$, had a heterojunction pP^+ barrier while the second sample grown, $F5$, had an isotype pp^+ barrier as shown in Fig. 2.

The mesa diodes for all five films were characterized by dark current-voltage (I-V) measurements and by deep level transient spectroscopy (DLTS). The dark I-V characteristics were measured using a Hewlett Packard 4145A semiconductor parameter analyzer. The $n = 1$ and $n = 2$ saturation current densities were extracted from the measured I-V characteristics by curve fitting. The $n = 2$ current component is of particular interest because it is directly related to both recombination in the space-charge region and to surface recombination around the junction perimeter.[6,7] Thus, the $n = 2$ current can provide an indication of the MBE film quality. Table I shows the average $n = 2$ saturation current densities J_{02} for films $F1$–$F5$.

Au-Ge	
emitter: N$_D \sim 1 \times 10^{18}$cm^{-3}	~1.0 μm GaAs
base: N$_A = 4.0 \times 10^{16}$cm^{-3}	1.35, .88, .90 μm GaAs
buffer: N$_A = 1 \times 10^{19}$cm^{-3}	0.0, 0.44, 0.90 μm GaAs
P$^+$ substrate	GaAs
N$_A \sim 10^{19}$cm^{-3}	
In	

FIG. 1. Device structure for films $F1$, $F2$, and $F3$. The GaAs buffer layer thickness was 0.0, 0.44, and 0.90 μm; the thickness of the base was 1.35, 0.88, and 0.90 μm for films $F1$, $F2$, and $F3$, respectively.

Au-Ge	
emitter: $N_D \sim 1 \times 10^{18} cm^{-3}$	0.69μm GaAs
base: $N_A = 3 \times 10^{16} cm^{-3}$	0.62μm GaAs
buffer: $N_A = 1 \times 10^{19} cm^{-3}$	0.69μm GaAs or $Al_{0.3}Ga_{0.7}As$
P⁺ substrate	GaAs
$N_A \sim 10^{19} cm^{-3}$	
In	

FIG. 2. Device structure for films $F4$ and $F5$. $F4$ had a 0.69-μm $Al_{0.3}Ga_{0.7}As$ buffer layer and $F5$ had a 0.69-μm GaAs buffer layer.

The first three isotype barrier films $F1$-$F3$ have J_{02} values that are five to six times lower than the J_{02} value for film $F5$. On the other hand, J_{02} for the heterojunction barrier film ($F4$) falls within the range of J_{02} values for films $F1$-$F3$. One would expect the impurity concentrations in film $F4$ to be greater than those in film $F5$ because film $F5$ was grown on the day following the growth of film $F4$. However, $F4$'s lower J_{02} value indicates that film $F4$ is actually of significantly higher quality than $F5$. It is our conclusion that the introduction of an AlGaAs buffer layer has caused the film quality of $F4$ to be comparable to that of $F1$-$F3$.

The MBE film quality was further investigated by means of DLTS. Our DLTS measurements have shown that deep level concentrations are greatly reduced when an AlGaAs buffer layer is used. We suspect that the AlGaAs layer traps impurities that are floating up from the substrate, and/or getters impurities from the subsequent GaAs layers during film growth. This is in agreement with McAfee et al.,[8] who observed a highly peaked spatial profile of deep levels located in a 140-Å-wide region at the GaAs/AlGaAs interface in MBE double heterostructure lasers. Photoluminescence[9,10] and capacitance-voltage[11] studies of GaAs quantum wells have also indicated the presence of impurities at the GaAs/AlGaAs interface.

Typical DLTS spectra for films $F1$-$F5$ are compared in Fig. 3. Figure 3(a), representative of films $F1$-$F3$, shows a prominent DLTS peak at about 320 K, a second peak at about 430 K, and lesser peaks at 360 K and between 100 and 200 K. Figure 3(b) is typical of film $F4$. Again there is a prominent peak at 320 K and lesser peaks to either side. Finally, Fig. 3(c) shows a representative DLTS scan for film $F5$. We reiterate that $F5$ was grown after $F4$ and is therefore expected to contain a lesser number of impurities. However, in addition to the ever present peak at 320 K, $F5$ has significant DLTS shoulders at 350, 260, 210, and 190 K. Clearly film $F5$ contains a greater number of deep levels than $F4$. With the exception of the deep level associated with the peak at 320 K, the AlGaAs buffer layer appears to have blocked and/or gettered impurities from the layers grown above it.

The DLTS peak at 320 K requires additional discussion, since it appears in all of the samples and seems unaffected by the AlGaAs layer. The average deep level concentration N_T associated with the 320 K peak for films $F1$-$F3$ was $N_T = 4.4 \times 10^{13}$ cm^{-3}. For film $F4$ the average trap concentration was $N_T = 1.0 \times 10^{14}$ cm^{-3}; for film $F5$ it was $N_T = 7.8 \times 10^{13}$ cm^{-3}. The results suggest that the concentration of this particular deep level is correlated with the amount of MBE material grown prior to each film growth. This observation in turn would imply that the deep level is related to impurities introduced by the system during film growth. Failure of these impurities to be gettered by the AlGaAs layer may indicate that they occupy substitutional lattice sites, or form vacancy complexes that do not readily diffuse to the AlGaAs layer during film growth. They appear to be continually incorporated into the film during the growth process along with the Ga, As, and dopant atoms.

The thermal activation energy for the 320 K peak was measured by DLTS to be $E_T - E_V = 0.55$ eV. The capture cross section for the majority-carrier holes was found to be $\sigma_p = 6.8 \times 10^{-16}$ cm^2. The impurity could therefore be iron,[12,13] or possibly a Ga vacancy[14] or vacancy complex. We suspect that this particular deep level does not control the J_{02} current. This is suggested by a comparison of the carrier
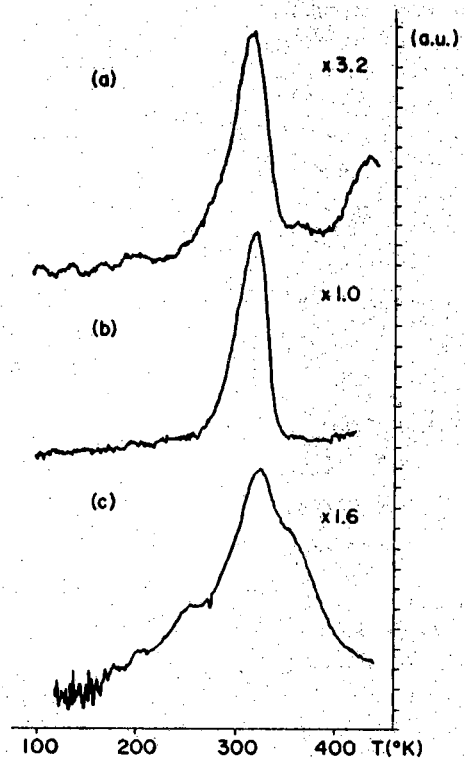

FIG. 3. Typical DLTS spectra for (a) films $F1$-$F3$, (b) film $F4$, and (c) film $F5$. The diodes were pulsed from 1.0 V reverse bias to 0.0 V with 1.0 ms fill pulses. The DLTS emission rate window was 200 s^{-1}.

TABLE I. $n = 2$ saturation current densities for films $F1$-$F5$.

Film I.D.	Growth date	J_{02} (pA/cm²)	Barrier
$F1$	8/11/86	263	p-GaAs/p^+-GaAs
$F2$	8/12/86	209	p-GaAs/p^+-GaAs
$F3$	8/13/86	252	p-GaAs/p^+-GaAs
MBE system was opened on 9/6/86			
$F4$	9/24/86	258	p-GaAs/P^+-$Al_{0.3}Ga_{0.7}As$
$F5$	9/25/86	1330	p-GaAs/p^+-GaAs

1540   J. Appl. Phys., Vol. 62, No. 4, 15 August 1987

Rancour et al.   1540

lifetimes as determined from DLTS and dark I-V data. For the deep level concentrations encountered here, the measured σ_p would imply hole lifetimes,

$$\tau_p \equiv 1/\sigma_p \langle V_{TH} \rangle N_T,$$

on the order of 0.1–$1.0\,\mu s$. However, the average recombination lifetime $\sqrt{\tau_n \tau_p}$, as determined from the measured $n = 2$ saturation current density (J_{02}) was on the order of 1.0 ns. Consequently, τ_n would have to be ~ 1.0 ps and σ_n on the order of 6.8×10^{-10} cm^2. A capture cross section on the order of 10^{-9}–10^{-10} cm^2 is unusually large.

The concentration of the 0.55-eV level does not correlate with the recombination current density. This further confirms our suspicions that the 0.55-eV level does not dominate the recombination current. However, the controlling recombination rate, whatever the mechanism, does appear to have been reduced by the presence of the AlGaAs layer. It is possible that a deep level, as yet undetected by our DLTS measurements, is controlling the $n = 2$ current. Another factor to consider is surface recombination around the device perimeter, which may make a significant contribution to J_{02}; gross defects (e.g., oval defects) are another possible contributor. Further work is needed to establish the controlling recombination mechanism.

In summary, we have shown that p-n junctions, fabricated from MBE GaAs films, show marked reductions in recombination current when an AlGaAs buffer layer is employed. Deep level concentrations are also reduced by the presence of an AlGaAs buffer layer. One deep level, possibly iron or a Ga vacancy/vacancy complex, remains unaffected by the AlGaAs buffer layer. This impurity/defect is either rigidly incorporated into the lattice during MBE film growth, or is highly soluble in AlGaAs. Fortunately, the cited deep level does not appear to significantly affect the $n = 2$ current density. The use of AlGaAs buffers should be independent of growth technology and could provide significant improvements in AlGaAs/GaAs films grown for bipolar applications.

[1]H. C. Hamaker, C. W. Ford, J. G. Werthen, G. F. Virshup, and N. R. Kaminar, Appl. Phys. Lett. 47, 762 (1985).
[2]S. Tiwari, S. L. Wright, and A. W. Kleinsasser, IEEE Trans. Electron Devices ED-34, 185 (1987).
[3]R. P. Gale, John C. C. Fan, G. W. Turner, and R. L. Chapman, in 17th IEEE Photovoltaic Specialists Conference, Kissimmee Florida (IEEE, New York, 1984), p. 1422.
[4]H. Beneking, P. Narozny, and N. Emeis, Appl. Phys. Lett. 47, 828 (1985).
[5]H. Beneking, P. Narozny, P. Roentgen, and M. Yoshida, IEEE Electron Device Lett. EDL-7, 101 (1986).
[6]H. C. Casey Jr., A. Y. Cho, and P. W. Foy, Appl. Phys. Lett. 34, 594 (1979).
[7]C. H. Henry, R. A. Logan, and F. R. Merritt, J. Appl. Phys. 49, 3530 (1978).
[8]S. R. McAfee, D. V. Lang, and W. T. Tsang, Appl. Phys. Lett. 40, 520 (1982).
[9]R. C. Miller, W. T. Tsang, and O. Munteanu, Appl. Phys. Lett. 41, 374 (1982).
[10]P. M. Petroff, R. C. Miller, A. C. Gossard, and W. Wiegmann, Appl. Phys. Lett. 44, 217 (1984).
[11]K. L. Tan, M. S. Lundstrom, and M. R. Melloch, Appl. Phys. Lett. 48, 428 (1986).
[12]P. K. Bhattacharya, H. J. Buhlmann, and M. Ilegems, J. Appl. Phys. 53, 6391 (1982).
[13]A. Mitonneau, G. M. Martin, and A. Mircea, Electron. Lett. 13, 666 (1977).
[14]A. Fazzio, J. R. Leite, and M. L. De Siqueira, J. Phys. C 12, 3469 (1979).

Bias-dependent photoresponse of p^+in GaAs/AlAs/GaAs diodes

M. R. Melloch, C. P. McMahon, M. S. Lundstrom, J. A. Cooper, Jr., Q-D. Qian, and
S. Bandyopadhyay

School of Electrical Engineering, Purdue University, West Lafayette, Indiana 47907

We report photocollection efficiency measurements of p^+in GaAs/AlAs/GaAs diodes fabricated on films grown by molecular beam epitaxy. Both the zero-bias and bias-dependent photocollection characteristics can be explained by assuming that the band discontinuity between AlAs and GaAs is mostly accommodated in the valence band.

Due to the important device applications of GaAs and $Al_xGa_{1-x}As$, there has been much activity in recent years to determine the band alignment of this heterojunction.[1-10] It is presently accepted that the Γ GaAs to Γ AlGaAs conduction-band discontinuity is between 0.6 and 0.65 of the direct band-gap difference. Recent workers have shown that Γ GaAs to X AlGaAs (in the indirect alloy) conduction-band discontinuity is significantly below 60% of the indirect band-gap difference.[6,8,10] From photosensitive capacitance-voltage measurements and internal quantum efficiency measurements of p^+in and n^+ip GaAs/AlAs/GaAs photodiodes, we have seen qualitative evidence that the band discontinuity between AlAs and GaAs is mostly accommodated in the valence band;[11,12] this is in agreement with recent reports of other investigators.[6,8,10] In this letter we report bias-dependent photoresponse measurements of p^+in photodiodes. The measurements clearly demonstrate that the band discontinuity is largely accommodated in the valence band.

The device, whose structure is shown in Fig. 1, uses films grown by molecular beam eptiaxy (MBE) in a Perkin–Elmer PHI 400 MBE system. The starting substrates were (100) cut and silicon doped at 1.5×10^{18} cm^{-3}. The GaAs buffer layer was grown at a substrate temperature of 600 °C and doped with silicon to 1.9×10^{16} cm^{-3}. The 4210-Å-thick undoped AlAs layer was grown at a substrate temperature of 700 °C. The top GaAs layer was grown at a substrate temperature of 600 °C and doped with beryllium to 1×10^{18} cm^{-3}. (The doping densities were determined by capaci-
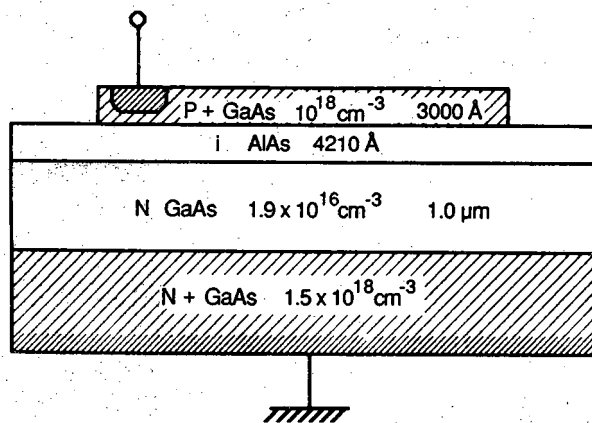
tance-voltage profiling.) Devices of dimension 300 μm by 300 μm were defined by photolithography and subsequent wet etching. Ohmic contacts of dimension 100 μm $\times$ 100 μm were then made to the top GaAs layer.

The relative photocollection efficiency is shown in Fig. 2 for the p^+in diode whose dimensions are shown in Fig. 1. The Fig. 2 data were taken at a temperature of 300 K and relative photocollection efficiencies are shown for various applied reverse bias. For our device dimensions, the absorption of the light will shift from the n GaAs buffer layer to the top p^+ GaAs layer as the wavelength decreases. From the Fig. 2 zero-bias photocollection efficiency one sees that the minority-carrier holes in the n GaAs buffer layer are not as efficiently collected as minority-carrier electrons in the p^+ GaAs top layer. This suggests a larger band-gap discontinuity in the valence band than in the Γ GaAs to X AlAs conduction band. As the wavelength of the light decreases past 500 nm, the photocollection efficiency begins to decrease. This decrease is due to surface recombination as more and more carriers are being generated near the surface. As the wavelength decreases below 420 nm, there is an initial increase in the photocollection. This increase is due to direct band-to-band generation in the AlAs layer. Also seen in the Fig. 2 data is that as the p^+in diode is reverse biased, the
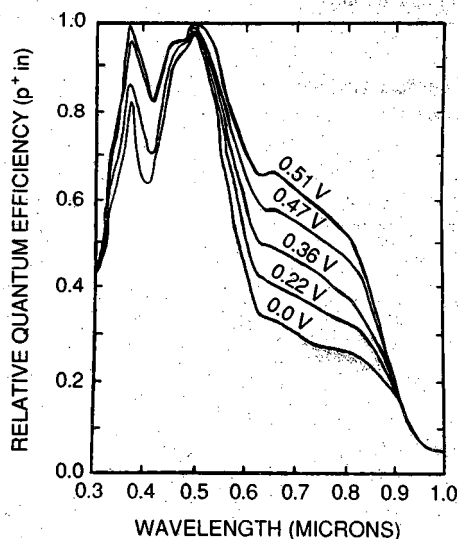

FIG. 1. p^+in GaAs/AlAs/GaAs device structure.

FIG. 2. Relative photocollection efficiency for the p^+in GaAs/AlAs/GaAs photodiode (whose dimensions are shown in Fig. 1) with external bias as a parameter.
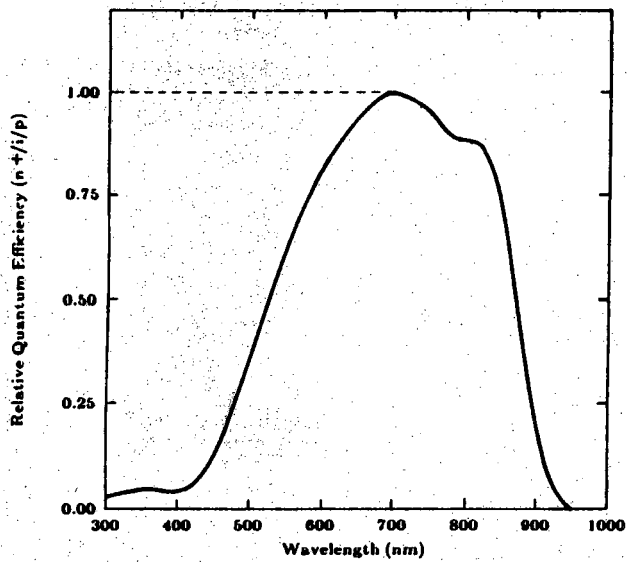
FIG. 3. Relative photocollection efficiency for an n^+ip GaAs/AlAs/GaAs photodiode. The top n^+ GaAs layer was 3000 Å thick and the AlAs layer was 2800 Å thick.

collection of minority-carrier holes in the n GaAs buffer layer increases relative to the minority-carrier electrons in the p^+ GaAs top layer.

A complementary device, n^+ip GaAs/AlAs/GaAs diode, was also fabricated and its zero-bias relative photocollection efficiency is shown in Fig. 3. Again for this device the absorption of the light will shift from the p GaAs buffer layer to the top n^+ GaAs layer as the wavelength decreases. From the Fig. 3 relative photocollection efficiency one sees that minority-carrier holes in the top n^+ GaAs layer are not as efficiently collected as minority-carrier electrons in the p GaAs buffer layer which also suggests that the valence-band discontinuity is much larger than the conduction-band discontinuity. (Note that the sharp decrease in photocollection efficiency for wavelengths shorter than 650 nm is not due to surface recombination which does not become significant unless $\lambda < 500$ nm; the sharp decrease is due to poor photocollection efficiency for holes.)

The photocollection efficiency at a wavelength of 800 nm for the p^+in structure depicted in Fig. 1 is shown as a function of reverse bias in Fig. 4; the measurement was made at a temperature of 300 K. At 800 nm the depth required to absorb 90% of the light in our structure is 1.73 μm.[13] Therefore, at 800 nm a large portion of the light is absorbed in the n GaAs buffer region. The data in Fig. 4 can be explained with the aid of Fig. 5. At zero bias there is a barrier to holes between the AlAs and n GaAs buffer region as shown in Fig. 5(a). As the diode is reverse biased the barrier will decrease, increasing the photocollection efficiency. At a large enough bias the barrier will be removed, as shown in Fig. 5(b), and the photocollection efficiency will saturate. One would expect that before the barrier is completely removed [as depicted in Fig. 5(b)] that the photocollection current would saturate when the holes are able to tunnel through the remaining potential barrier. An analysis based on a numerical
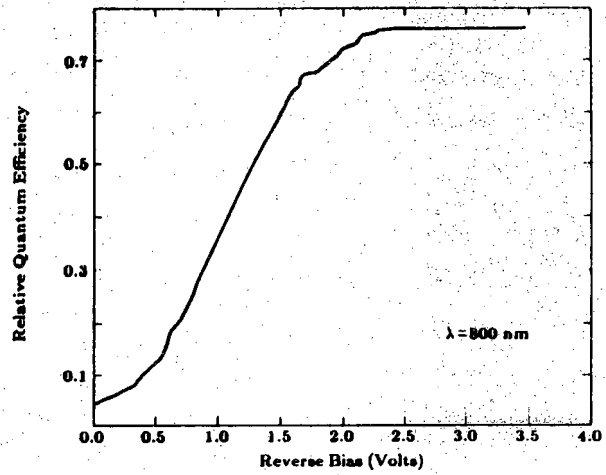

FIG. 4. Relative photocollection efficiency at a wavelength of 800 nm as a function of reverse bias of the p^+ in photodiode.

technique for solving the Schrödinger equation[14] shows that this tunneling can lower the effective barrier by a maximum of 10 meV.

In summary, we have measured the relative photocollection efficiency of p^+in and n^+ip GaAs/AlAs/GaAs photodiodes. The photoresponses can be explained based on the band discontinuity between AlAs and GaAs being mostly accommodated in the valence band. The effect of external
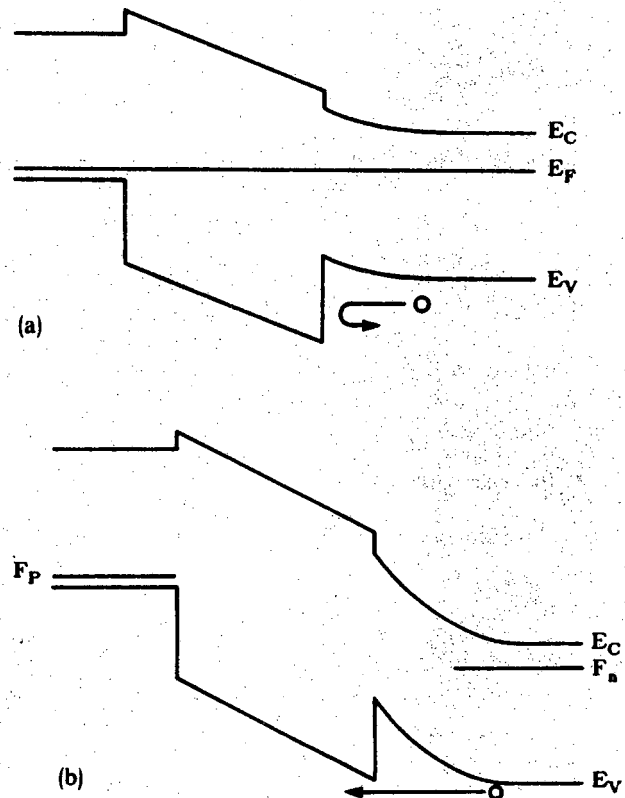

FIG. 5. Energy-band diagrams of the p^+in GaAs/AlAs/GaAs photodiode: (a) zero-bias condition; (b) biased to where the valence-band discontinuity is equal to the band bending in the n GaAs buffer region.

bias on the photoresponse of the p^+in GaAs/AlAs/GaAs diode was also reported.

[1] R. Dingle, W. Weigman, and C. H. Henry, Phys. Rev. Lett. **33**, 750 (1978).

[2] H. Kroemer, Wu-Yi Chien, H. C. Casey, Jr., and A. Y. Cho, Appl. Phys. Lett. **33**, 749 (1978).

[3] H. Kroemer, Wu-Yi Chien, J. S. Harris, Jr., and D. D. Edwall, Appl. Phys. Lett. **36**, 295 (1980).

[4] J. R. Waldrop, S. P. Kowalczyk, R. W. Grant, E. A. Kraut, and D. L. Miller, J. Vac. Sci. Technol. **19**, 573 (1981).

[5] D. Arnold, A. Ketterson, T. Henderson, J. Klem, and H. Morkoç, Appl. Phys. Lett. **45**, 1237 (1984).

[6] J. Batey and S. L. Wright, 1985 IEEE Device Research Conference, June 17–19, 1985, University of Boulder, Boulder, CO.

[7] H. Okumura, S. Misawa, S. Yoshida, and S. Gonda, Appl. Phys. Lett. **46**, 377 (1985).

[8] T. J. Drummond and I. J. Fritz, Appl. Phys. Lett. **47**, 284 (1985).

[9] K. L. Tan, M. S. Lundstrom, and M. R. Melloch, Appl. Phys. Lett. **48**, 428 (1986).

[10] B. A. Wilson, P. Dawson, C. W. Tu, and R. C. Miller, J. Vac. Sci. Technol. B **4**, 1037 (1986).

[11] J. A. Cooper, Jr., Q-D. Qian, and M. R. Melloch, Appl. Phys. Lett. **48**, 365 (1986).

[12] M. R. Melloch, C. P. McMahon, M. S. Lundstrom, J. A. Cooper, Jr., and Q-D. Qian, to be published in Solar Cells.

[13] C. Mazier, "Material Models and Device Structure for GaAs Solar Cells," SERI subcontract report, prepared under subcontract No. XL-3-03124-1, 1984.

[14] M. Cahay, M. McLennan, S. Bandyopadyay, S. Datta, and M. S. Lundstrom, *Proceedings of the 2nd International Conference on Simulation of Semiconductor Devices and Processes, Swansea, U. K. July 21–23, 1986* (Pineridge, Swansea, U. K., 1986), p. 58.